UNIVERSIDAD DE CHILE
FACULTAD DE CIENCIAS FÍSICAS Y MATEMÁTICAS
DEPARTAMENTO DE FÍSICA

STUDY OF ZERO-TEMPERATURE NEUTRON MATTER WITHIN SELF-CONSISTENT GREEN'S FUNCTION THEORY

TESIS PARA OPTAR AL GRADO DE
MAGÍSTER EN CIENCIAS, MENCIÓN FÍSICA

MATÍAS IGNACIO GUTIÉRREZ ESCOBARI

PROFESOR GUÍA:
HUGO ARELLANO SEPÚLVEDA

MIEMBROS DE LA COMISIÓN:
LUIS FOÀ TORRES
ARNAU RIOS HUGUET

Powered@NLHPC: Esta tesis fue parcialmente apoyada por la infraestructura de supercómputo del NLHPC (ECM-02) y parcialmente financiada por la beca ANID-Subdirección de Capital Humano/Magíster Nacional/2021 - 22210411

SANTIAGO DE CHILE
2023

RESUMEN DE LA TESIS PARA OPTAR AL GRADO DE
MAGÍSTER EN CIENCIAS, MENCIÓN FÍSICA
POR:MATÍAS IGNACIO GUTIÉRREZ ESCOBARI
FECHA:2023
PROF. GUÍA:HUGO ARELLANO SEPÚLVEDA

ESTUDIO DE MATERIA DE NEUTRONES A TEMPERATURA CERO DENTRO DE LA TEORÍA DE FUNCIONES DE GREEN AUTOCONSISTENTES

Las propiedades de materia de neutrones en estado normal a temperatura cero son investigadas dentro de la teoría de funciones de Green autoconsistentes (SCGF, por sus siglas en inglés) en la aproximación escalera utilizando la interacción nucleón-nucleón realista Argonne V18. Dentro de este marco de trabajo, la dinámica intermedia de dos cuerpos viene dada por la propagación partícula-partícula (p-p) y agujero-agujero (a-a), en contraste con la aproximación de Brueckner-Hartree-Fock (BHF), que solo tiene en cuenta la propagación p-p. Se revisa la aparición de estados ligados en el medio dentro de BHF y se explora la formación de estos estados en el contexto de la teoría SCGF. Para obtener soluciones estables y autoconsistentes, se implementa una descomposición de las funciones espectrales para controlar simultáneamente las excitaciones de las cuasipartículas y la dispersión de las partículas sobre las energías. Obtenemos la estructura *off-shell* de las funciones espectrales y de la autoenergía, junto con otras cantidades relevantes, como las distribuciones de momento, la energía del sistema y el camino libre medio de neutrones en el medio. La dependencia en la densidad de las cantidades mencionadas anteriormente es estudiada. Los valores *on-shell* de la autoenergía se comparan con los resultados del esquema de BHF. Finalmente, se aborda la aparición de estados ligados en el medio en el plano de energías complejo y se propone una conexión con el estado superfluído. En comparación con resultados dentro de BHF, el efecto general de la inclusión de la propagación a-a es de naturaleza repulsiva. Esto es observado tanto en los valores *on-shell* de la autoenergía, como en la ecuación de estado para neutrones a altas densidades. Adicionalmente, la inclusión de la propagación a-a inhibe la posibilidad de estados ligados en el medio de la manera descrita dentro de BHF. A pesar de esto, hemos encontrado la aparición de autoenergías complejas para el problema de estados ligados para densidades menores que 0.08 fm^{-3}. Una característica interesante de estas autoenergías es el comportamiento cualitativo de su parte imaginaria como función de la densidad, el cual se asemeja al comportamiento del gap de energía en la superficie de Fermi en materia neutrónica superfluída.

THESIS ABSTRACT FOR THE DEGREE OF MASTER OF SCIENCE IN PHYSICS
BY:MATÍAS IGNACIO GUTIÉRREZ ESCOBARI
DATE:2023
ADVISOR:HUGO ARELLANO SEPÚLVEDA

STUDY OF ZERO-TEMPERATURE NEUTRON MATTER WITHIN SELF-CONSISTENT GREEN'S FUNCTION THEORY

The properties of zero-temperature normal neutron matter are investigated within the self-consistent Green's function theory (SCGF) in the ladder approximation using the realistic Argonne V18 nucleon-nucleon interaction. Within this framework, the intermediate two-body dynamics is given by both particle-particle (p-p) and hole-hole (h-h) propagation, in contrast to the Brueckner-Hartree-Fock (BHF) approximation, which only accounts for p - p propagation. The appearance of *in-medium* bound states within BHF is reviewed and the formation of these states is explored in the context of SCGF theory. To obtain fully self-consistent stable solutions, we implement a decomposition for the spectral functions to control simultaneously quasi-particle excitations and the dispersion of the particles over energies. We obtain the off-shell structure of the self-energy and spectral functions, together with other relevant quantities, such as momentum distributions, the energy of the system and the *in-medium* neutron mean-free path. The density dependence of the quantities mentioned before is studied. The on-shell values of the self-energy are compared to BHF results. Also, the appearance of *in-medium* bound states in the complex energy plane is addressed and its connection to the superfluid state is proposed. In comparison with BHF results, the overall effect of the inclusion of h-h propagation is of repulsive nature. This is observed both in the on-shell self-energy and in the neutron equation state for higher densities. Moreover, the inclusion of h-h propagation inhibits the possibility of *in-medium* bound states in the way described within BHF. Despite this, we have found the appearance of complex eigenenergies for the bound state problem for densities below 0.08 fm^{-3}. An interesting feature of these eigenergies is the qualitative behavior of their imaginary part as function of the density, which resembles the behavior of the energy gap at the Fermi surface in superfluid neutron matter.

A los cimientos de mi existencia: mis adoradas mamitas Hilda y Reina, y a mi querido papito Dario. Gracias a su amoroso cuidado, hoy florezco y me mantengo vivo, honrando su legado con cada paso que doy.

Agradecimientos

Aunque la tesis está escrita en inglés, me gustaría reservar una página especial para expresar mis sinceros agradecimientos en español.

A mi profesor guía Hugo Arellano, por su invaluable apoyo, sabiduría y orientación a lo largo de este camino.

Al profesor Francisco Brieva, por su capacidad para incentivar desafíos y su valiosa crítica constructiva.

A mi madre Leticia, por su dedicación, sacrificio y cariño. Gracias por ser mi apoyo incondicional.

A mis hermanas Belén y Amanda, por la conexión especial que compartimos. Por ser mis cómplices y amigas.

A Gonzalo, por estar a mi lado en cada paso del camino y por hacerme sentir apoyado en todo momento. También a su familia por darme la bienvenida con los brazos abiertos y por hacerme sentir parte de ese cálido hogar.

A Peter, mi peludo compañero, por su reconfortante presencia tranquila.

A mis abuelas y abuelo, Hilda, Reinaldina y Dario, respectivamente. Gracias por su sabiduría y valores imperecederos.

A Eduardo, por haber propiciado mi comodidad y bienestar al vivir en la capital.

A mi tía Estefanny y a su familia, por ser la chispa de alegría que ilumina cada lugar.

A mis amigos y amigas, Isadora, Javiera, Marcela, César, Israel, Skarlett y Melissa. Gracias por regalarme incontables buenos momentos y risas que llenan mi vida de felicidad y alegría.

A mi padre Pablo, por la ayuda económica necesaria para vivir en la capital. También a Karina, Valentina y Constanza. Saber que están ahí para mí, me llena de gratitud.

TABLE OF CONTENT

List of Tables

List of Figures

Chapter 1

Introduction

A major thrust to nuclear physics has been to account for the properties of interacting nucleons starting from their basic forces. This includes the study of finite nuclei as well as infinite nuclear matter. The former systems consists of a fixed number of nucleons bound in space, while the latter is an hypothetical infinite and homogeneous system. Over the last years, an increasing interest has been given to the study of infinite neutron matter, due to its connections to astrophysics and condensed matter physics [48].

In astrophysics, the outer core of neutron stars is formed mostly by neutron matter [83]. Consequently, the study of the equation of state of neutron matter becomes crucial to understand the structure and evolution of neutron stars. Ongoing astrophysical observations continue to provide new constraints on the mass-radius relation, which in turn gives additional restrictions to the equation of state of dense neutron matter [65, 90, 91]. With the first observation of GW170817 by LIGO and Virgo [1, 2], neutron star mergers have gained prominence in the understanding of heavy-element synthesis and neutron-rich matter [52]. In a future, measurements of gravitational waves coming from neutron star mergers will provide new data to understand the structure of neutron matter [13].

In condensed matter physics, low-density neutron matter is connected to ultracold atoms experiments [11]. If these strong-interacting fermionic systems are diluted with large scattering lengths, one says that the system lies in a unitary regime. In such a limit, if effects of finite range in the interaction are neglected, strong-interacting ultracold atoms and neutron matter exhibit a "universal" behaviour in their dynamics. In this limit the properties of the system would depend only on the product of the Fermi momentum and the scattering length [49]. These properties result proportional to the ones of the free fermionic system [25]. In this way, experiments provide tests for quantum many-body theories.

For microscopic or *ab-initio* studies of nuclear systems, we require the knowledge of the bare interaction. Several nucleon-nucleon (NN) potential models have been developed over the years, where masses and coupling constants are adjusted in order to provide best fits to phase-shifts from scattering data, in addition to properties of the deuteron. Some examples of these models are the Paris [58] , Nijmegen [92], Argonne V18 [100] and a group of chiral effective-field-theory potentials. In the case of chiral potentials, different orders in the expansion parameter have been reported, such as next-to-next-to-next-to-leading order (N^3LO) [41] and next-to-next-to-next-to-next-to-leading order (N^4LO) [40, 42]. In all these constructions, the NN interaction shows a repulsive short-range and attractive long range part, accounted by meson exchange processes.

To obtain properties of complex nuclear systems requires a plausible many-body approach which, under reasonable approximations, provides the best possible description of the system. To this purpose we quote variational techniques [27], Monte Carlo calculations [59], the Coupled Cluster [17] method and diagrammatic approaches. The last ones are based on graphical expansions of the physical quantities that encode the different interactions processes between the system constituents. Some examples are the Brueckner-Hartree-Fock (BHF) [22, 23] approximation and self-consistent Green's function (SCGF) theory approaches [73, 88].

The BHF approximation is based on the Goldstone hole-line expansion for the ground state energy, where only two-hole line diagrams are added up. This framework has been extensively used to study saturation properties of nuclear matter [12, 61, 62, 89], in addition to the construction of effective interactions for microscopic calculations of optical models potentials for nucleon-nucleus scattering [8, 64]. Additionally, a relativistic version of this approximation has been developed, known as the Dirac-Brueckner-Hartree-Fock approximation [6, 21], where the relativistic scattering amplitudes are corrected to account for *in-medium* effects.

Within the BHF approximation, one can also study the formation of *in-medium* structures. In this line, after a careful account for *in-medium* di-nucleons, Arellano *et al.* [10, 54] have reported coexisting single-particle solutions in zero-temperature isospin-symmetric nuclear matter at low densities. In the same way, studies pursued in the case of pure neutron matter lead to neutron-neutron bound states. In general, these bound states exhibit large coherence lengths and their features appear to be robust under the bare NN interaction in use. Additionally, a resemblance is found between the *in-medium* bound states and the Cooper pairs within the Bardeen-Cooper-Schrieffer theory.

In SCGF theory, the one-particle propagator is expanded in terms of diagrams. In contrast with the BHF approximation, where the hole-hole propagation is neglected, forward and backward propagation in time are treated symmetrically. Moreover, within this theory, particles with a given momentum are dispersed over a range of energies (they do not fulfill an energy-momentum relation) but they peak at the position of the quasi-particle energy. Self-consistency arises by considering the propagation of a nucleon interacting with the surrounding nucleons. The last ones are also dispersed over a wide range of energies and are described with the same Green's function. The equations and diagrams that describe the theory are relatively simple to derive, although the implementation of a numerical iterative procedure is a complex task requiring some approximations. To account for correlations in the nuclear medium, the T matrix is introduced. This matrix includes multiple particle-particle and hole-hole scattering processes. This treatment of the *in-medium* effective interaction is known as the ladder approximation. A sustained improvement in the calculation of the full off-shell self-energy within SCGF theory in the ladder approximation has been achieved over the last three decades. This mainly includes the work done by the Barcelona, St. Louis, Rostock, Tübingen, Ghent, and Krakow groups [5, 18–20, 24, 26, 31, 33, 35, 37, 44–46, 53, 66, 67, 70–72, 76, 77, 82, 84–86, 95], among others.

In this work, we will study microscopic properties of zero-temperature neutron matter within SCGF theory, using the realistic Argonne V18 [100] interaction. Approximations and numerical routines have been developed to solve the associated equations. The main motivation is to quantify the effect of the inclusion of h-h propagation in the self-energy and in the appearance of *in-medium* bound states.

The thesis is organized as follows. In Chap. 2 the nuclear-many body problem is introduced, describing the main properties of nucleons and their interaction. Afterwards, a detailed derivation of the equations involved in the SCGF theory at zero-temperature is presented. Additionally, a short derivation of the BHF approximation is obtained, starting from the SCGF equations. In Chap. 3 we review the main features of *in-medium* bound states in both isospin-symmetric nuclear matter and neutron matter. Later on, the manifestation of these states is discussed within SCGF theory. Results are presented in Chap. 4, where we give qualitative and quantitative descriptions of the main microscopic properties of neutron matter, such as the self-energy, spectral functions, momentum distributions, equation of state and *in-medium* mean-free path. Also, the appearance of *in-medium* bound states is discussed. A summary and conclusions of the results obtained from this study are outlined in Chap. 5. Additionally, an annex is included at the end of the thesis, containing some of the equations of the SCGF scheme that are modified when an approximation for the spectral functions is introduced.

Chapter 2

The nuclear many-body problem

One of the main challenges in quantum many-body physics is that of accounting for empirical information of the system, such as the saturation point of isospin-symmetric nuclear matter, starting from the underlying fundamental interaction. We have access to physical properties by extrapolating nuclear data from finite nuclei to infinite matter. The behaviour of the binding energy of a finite nuclei can be represented by the Bethe–Weizsäcker semi-empirical mass formula [14, 15]

$$B(N,Z) = a_V A - a_S A^{2/3} - a_A \frac{(N-Z)^2}{A} - a_C \frac{Z^2}{A^{1/3}} - \delta_P(A) \ , \tag{2.1}$$

where N is the neutron number, Z the proton number and A the mass number of the nucleus. The first term accounts for the bulk binding energy characterized by the parameter a_V, the second one corresponds to the surface correction (a_S), the asymmetry (or Pauli) contribution is given by the third term, the fourth term accounts for the Couloumb energy (a_C) and the last term for pairing energy, which can be either zero or $\pm\delta_0(A)$, depending on the parity of N and Z. In most models, $\delta_0(A)$ takes the form $\delta_0(A) = a_P A^{k_P}$ with k_P some negative exponent.

Considering isospin-symmetric nuclei ($N = Z$) and neglecting the Couloumb energy, one obtains for the binding energy per nucleon

$$\frac{B(N,Z)}{A} = a_V - a_S A^{-1/3} \ . \tag{2.2}$$

In the limit of an infinite system ($A \to \infty$) only the first term remains, leading to

$$\lim_{A\to\infty} \frac{B(N,Z)}{A} = a_V \ . \tag{2.3}$$

By fitting the measured masses of nuclei, the coefficient a_V is calculated leading to $a_V = 16 \pm 1$ MeV [50].

On the other hand, electron scattering experiments are useful to obtain the charge distribution of nuclei, which in the case of heavy nuclei, it is proportional to the total density. The main result from the experiment is that the charge density inside heavy nuclei is roughly constant throughout the nuclear mass table, resulting in a value of $\rho_0 = 0.16 \pm 0.01$ fm^{-3}. This is known as the saturation density of nuclear matter. Thus, any realistic calculation of nuclear matter properties is expected to account for a minimum of energy [50]

$$\frac{E}{A} = -16.0 \pm 1.0 \text{ MeV} , \tag{2.4}$$

at the saturation density

$$\rho_0 = 0.16 \pm 0.01 \text{ fm}^{-3} . \tag{2.5}$$

2.1 The nucleon-nucleon interaction

In the nuclear many-body problem, protons and neutrons are the main constituents of the system. In Tab. 2.1 we show the mass, charge and quark composition of protons and neutrons. Note the small difference, up to about 0.1%, between proton and neutron masses. Considering that electromagnetic interactions are week relative to nuclear strong interactions, protons and neutrons can be conceived as two different states of a same particle, the nucleon (N). This is known as isospin symmetry, where the interaction between pairs of nucleons is described as that for two isospin states.

	proton	neutron
Mass (MeV)	938.27	939.56
Electric charge (e)	+1	0
Quark composition	uud	udd

Table 2.1: Physical properties of the proton and neutron.

Most of the information on the NN interaction is obtained from NN collisions, together with properties of the deuteron, the only NN bound state in free space. Through the analysis of phase shifts, one can infer some properties of the bare NN interaction. At large distance, above 2 fm, the interaction is exponentially attractive. At intermediate distances, between 1 and 2 fm, the interaction becomes stronger. At short distance, below 1 fm, a very strong repulsive core is present. These features are illustrated in Fig. 2.1.

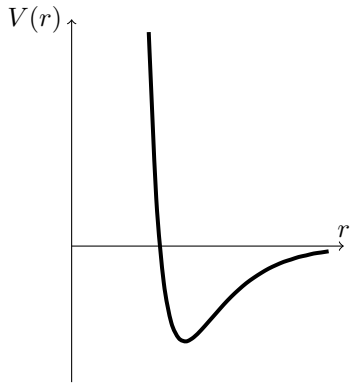

Figure 2.1: Attractive and repulsive features of the NN interaction.

Theoretically, NN potentials are constructed within the framework of meson exchange models. As in quantum electrodynamics, where the photon-exchange process accounts for the Couloumb interaction, the pion-exchange process is responsible for the long range interaction between nucleons. The intermediate range part of the nuclear interaction is explained through the exchange of heavier mesons such as scalar mesons σ, with suitable mass and coupling to reproduce the scattering data. The repulsive core require the exchange of heavy vector mesons, like the ρ and ω mesons [55].

Current approaches to NN interactions are based on chiral effective-field-theory (χEFT) potentials, initially introduced by Weinberg in the early 1990's [97–99]. This theory relies on the chiral symmetry of quantum chromodynamics (QCD) that governs low-energy hadron dynamics. The potentials are constructed by considering nucleons and pions as the relevant degrees of freedom at low-energy scales. A perturbative expansion is made, in powers of $(Q/\Lambda_{\mathrm{QCD}})$, where Q is the energy of the process and Λ_{QCD} is the QCD scale parameter. This leads to different classes of potentials according to the order in the chiral expansion. Some examples are the N^{3}LO [41] and N^{4}LO [40, 42] potentials. Additionally, sub-hadronic physics can be incorporated by means of the low-energy constants (LECs).

NN potential models designed to reproduce the scattering data are called realistic. Some modern realistic NN interaction models are the Paris [58], Nijmegen [92] and Argonne [100] potentials. Also, some χEFT can be considered realistic when the LECs are adjusted to reproduce the NN data. These models are typically constructed to provide the best fit to scattering data below 300 MeV in the laboratory frame system, in addition to the properties of the deuteron.

The deuteron constitutes the only two-nucleon bound state of a proton-neutron pair with a binding energy of -2.22 MeV, isospin $T = 0$ and parity $J^\pi = 1^+$. Experiments in molecular spectroscopy show that the deuteron has a total angular momentum $J = 1$ [63].

For two spin-1/2 nucleons, only total spin $S = 0$ and 1 are allowed. Therefore, the orbital angular momentum is restricted by $J - 1 < L < J + 1$, so $L = 0, 1, 2$ are allowed. Since the parity π is given by $(-1)^L = +1$, then only $L = 0$ and $L = 2$ are allowed. Experiments also measure a certain quadrupole moment for the deuteron. This tells us that the deuteron eigenfunction is a ${}^3S_1$-${}^3D_1$ partial waves mixture, because the wave function can not be a spherically symmetric S-wave. The mixture of these channels can be explained theoretically by including a tensor component in the NN interaction. We have obtained the wavefunctions of the deuteron for the AV18 interaction. The probability densities for $M = 0, 1$ total angular momentum $\hat{z}$ components are shown in Fig. 2.2, together with the radial wave functions for S and D channels.

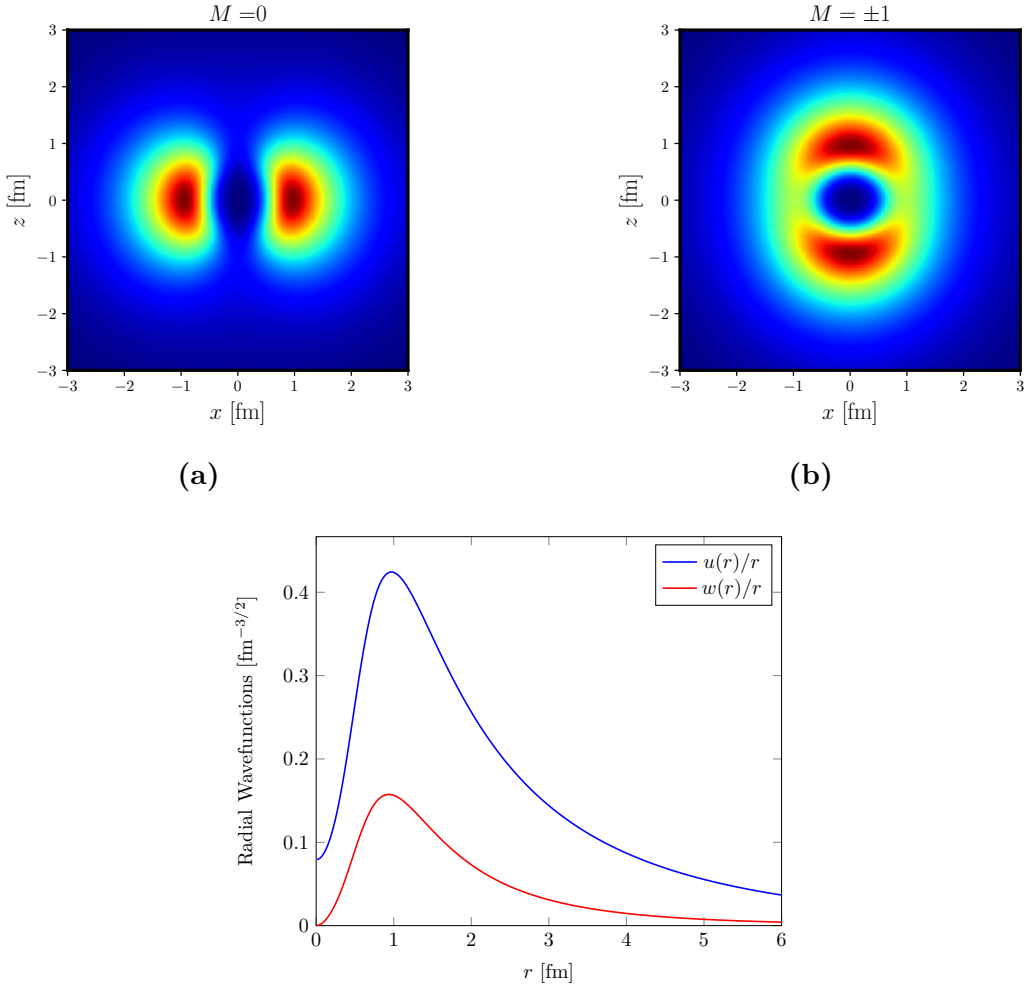

Figure 2.2: Deuteron probability densities for $M = 0$ (a) and $M = \pm 1$ (b) total angular momentum J_z component, together with the radial wave functions (c). In (a) and (b), the red spots correspond to the maximal probability densities, while the blue spots correspond to lower densities. In (c), u and w are the standard reduced radial wavefunctions [80]. The interaction is AV18.

Finally, because of the nucleon is not an elementary particle, it is not guaranteed that the nuclear interaction is described only by two body forces. In general one can expect that the interaction in a system of many nucleons is the sum of the interaction between pairs of nucleons and three nucleons or more nucleon forces. However, it is reasonable to assume, as starting point, that two-body forces (2BF) are dominant.

2.2 Green's functions at zero-temperature

In this section, we review some key elements for the description of many-fermion systems within the real time formalism at zero-temperature. This will help to establish the notation and highlight some analytical results that will be used throughout this Thesis.

2.2.1 Green's Functions

The state of a quantum mechanical system composed of many identical particles can be described in terms of field operators $\hat{\psi}^\dagger(\xi)$ and $\hat{\psi}(\xi)$

$$\begin{aligned} \hat{\psi}(\xi) &= \sum_i \varphi_i(\xi) a_i \ , \\ \hat{\psi}^\dagger(\xi) &= \sum_i \varphi_i^*(\xi) a_i^\dagger \ , \end{aligned} \tag{2.6}$$

with $a_i^\dagger$ and a_i creation and annihilation operators, respectively. Here, $\varphi_i(\xi)$ represents the wave function of the particle in state i. The sum is done over a complete set of single particle quantum numbers. These operators are interpreted as the operators for annihilation or creation of a particle at a given point in ξ-space, whereξ stands for coordinate or momentum. In the case of identical fermions, they obey the anti-commutation relations

$$\begin{aligned} &\{\hat{\psi}(\xi), \hat{\psi}^\dagger(\xi')\} = \delta(\xi - \xi') \ , \\ &\{\hat{\psi}(\xi), \hat{\psi}(\xi')\} = 0 \ , \\ &\{\hat{\psi}^\dagger(\xi), \hat{\psi}^\dagger(\xi')\} = 0 \ . \end{aligned} \tag{2.7}$$

In this representation, the Hamiltonian takes the form ($\hbar = 1$)

$$\begin{aligned} \hat{H} = &\int \left[\frac{1}{2m} \nabla \hat{\psi}^\dagger(\mathbf{r}) \cdot \nabla \hat{\psi}(\mathbf{r}) + U(\mathbf{r}) \hat{\psi}^\dagger(\mathbf{r}) \hat{\psi}(\mathbf{r}) \right] d\mathbf{r} \\ &+ \frac{1}{2} \int \int \hat{\psi}^\dagger(\mathbf{r}) \hat{\psi}^\dagger(\mathbf{r}\,') V(\mathbf{r}, \mathbf{r}\,') \hat{\psi}(\mathbf{r}\,') \hat{\psi}(\mathbf{r}) d\mathbf{r} d\mathbf{r}' \ , \end{aligned} \tag{2.8}$$

where a time-independent external field $U(\mathbf{r})$ and a two-body interaction $V(\mathbf{r},\mathbf{r}')$ was assumed.

In one-body quantum mechanics, the propagator or Green's function gives information of the time evolution of the system. In the case of a many-body quantum system one can define a one-particle Green's function in terms of field operators in the Heisenberg representation $\hat{O}_H(t) = e^{i\hat{H}t}\hat{O}e^{-i\hat{H}t}$, as follows [3, 56]

$$G(1,1') = -i\left\langle \hat{T}[\hat{\psi}_H(1)\hat{\psi}_H^\dagger(1')]\right\rangle \ , \tag{2.9}$$

where 1 and $1'$ stand for points in the space of interest, e.g., 1 and $1'$ can mean $\mathbf{r}_1, t_1$ and $\mathbf{r}_{1'}, t_{1'}$ respectively. In this construction, $\hat{T}$ represents the time-ordering operation, defined as

$$\hat{T}[A(t)B(t')] = A(t)B(t')\theta(t-t') \mp B(t')A(t)\theta(t'-t) \ , \tag{2.10}$$

where the upper(lower) sign corresponds to fermions(bosons). The average is taken over the ground state of the N particle system.

A two-particle Green's function is defined by

$$G_2(12,1'2') = (-i)^2\left\langle \hat{T}[\hat{\psi}_H(1)\hat{\psi}_H(2)\hat{\psi}_H^\dagger(1')\hat{\psi}_H^\dagger(2')]\right\rangle \ . \tag{2.11}$$

In general, one can define an n-particle Green's function as

$$G_n(12\ldots n,1'2'\ldots n') = (-i)^n\left\langle \hat{T}[\hat{\psi}_H(1)\hat{\psi}_H(2)\cdots\hat{\psi}_H(n)\hat{\psi}_H^\dagger(1')\hat{\psi}_H^\dagger(2')\cdots\hat{\psi}_H^\dagger(n')]\right\rangle \ . \tag{2.12}$$

The Green's function $G(1,1')$ describes the propagation of disturbances in which a single particle is added or removed from the many-particle system. Similarly, the two-particle Green's function describes disturbances produced by the removal or addition of two particles.

From the equation of motion for an operator in the Heisenberg representation, one can obtain the equation of motion for the one-body Green's function. Indeed, starting from

$$i\frac{\partial\hat{\psi}_H}{\partial t} = [\hat{\psi}_H, \hat{H}_H] \ , \tag{2.13}$$

considering only two-particle interactions

$$\begin{aligned}\hat{H} = &-\int \frac{1}{2m}\hat{\psi}_H^\dagger(\mathbf{r},t)\nabla^2\hat{\psi}_H(\mathbf{r},t)d\mathbf{r} \\ &+\frac{1}{2}\iint \hat{\psi}_H^\dagger(\mathbf{r},t)\hat{\psi}_H^\dagger(\mathbf{r}',t)V(\mathbf{r},\mathbf{r}')\hat{\psi}_H(\mathbf{r}',t)\hat{\psi}_H(\mathbf{r},t)d\mathbf{r}d\mathbf{r}' \ ,\end{aligned} \tag{2.14}$$

then

$$
\begin{aligned}
i\frac{\partial\hat{\psi}_H}{\partial t}(\mathbf{r},t) = &-\int \frac{1}{2m}[\hat{\psi}_H(\mathbf{r},t)\ ,\ \hat{\psi}_H^\dagger(\mathbf{r}',t)\nabla^2\hat{\psi}_H(\mathbf{r}',t)]d\mathbf{r}' \\
&+\frac{1}{2}\iint[\hat{\psi}_H(\mathbf{r},t)\ ,\ \hat{\psi}_H^\dagger(\mathbf{r}',t)\hat{\psi}_H^\dagger(\mathbf{r}'',t)V(\mathbf{r}',\mathbf{r}'')\hat{\psi}_H(\mathbf{r}'',t)\hat{\psi}_H(\mathbf{r}',t)]d\mathbf{r}'d\mathbf{r}'' \ .
\end{aligned}
\tag{2.15}
$$

The anti-conmutation rules in Eq. (2.7) are also valid for the operators in the Heisenberg representation at equal times. Then, using $[A,BC]=\{A,B\}C-B\{A,C\}$, we obtain

$$
[\hat{\psi}_H(\mathbf{r},t),\hat{\psi}_H^\dagger(\mathbf{r}',t)\nabla^2\hat{\psi}_H(\mathbf{r}',t)] = \delta(\mathbf{r}-\mathbf{r}')\nabla^2\hat{\psi}_H(\mathbf{r}',t)\ ,
\tag{2.16}
$$

and

$$
\begin{aligned}
&[\hat{\psi}_H(\mathbf{r},t)\ ,\ \hat{\psi}_H^\dagger(\mathbf{r}',t)\hat{\psi}_H^\dagger(\mathbf{r}'',t)\hat{\psi}_H(\mathbf{r}'',t)\hat{\psi}_H(\mathbf{r}',t)] \\
=&\delta(\mathbf{r}-\mathbf{r}')\hat{\psi}_H^\dagger(\mathbf{r}'',t)\hat{\psi}_H(\mathbf{r}'',t)\hat{\psi}_H(\mathbf{r}',t) - \delta(\mathbf{r}-\mathbf{r}'')\hat{\psi}_H^\dagger(\mathbf{r}',t)\hat{\psi}_H(\mathbf{r}'',t)\hat{\psi}_H(\mathbf{r}',t)\ .
\end{aligned}
\tag{2.17}
$$

Thus, the equation of motion becomes

$$
i\frac{\partial\hat{\psi}_H}{\partial t}(\mathbf{r},t) = -\frac{1}{2m}\nabla^2\hat{\psi}_H(\mathbf{r},t) - \int V(\mathbf{r},\mathbf{r}')\hat{\psi}_H^\dagger(\mathbf{r}',t)\hat{\psi}_H(\mathbf{r}',t)\hat{\psi}_H(\mathbf{r},t)d\mathbf{r}'\ ,
\tag{2.18}
$$

or

$$
\left(i\frac{\partial}{\partial t}+\frac{1}{2m}\nabla^2\right)\hat{\psi}_H(\mathbf{r},t) = \int V(\mathbf{r},\mathbf{r}')\hat{\psi}_H^\dagger(\mathbf{r}',t)\hat{\psi}_H(\mathbf{r}',t)\hat{\psi}_H(\mathbf{r},t)d\mathbf{r}'\ .
\tag{2.19}
$$

Here, we have assumed $V(\mathbf{r},\mathbf{r}')=V(\mathbf{r}',\mathbf{r})$. A similar procedure yields

$$
\left(-i\frac{\partial}{\partial t}+\frac{1}{2m}\nabla^2\right)\hat{\psi}_H^\dagger(\mathbf{r},t) = \hat{\psi}_H^\dagger(\mathbf{r},t)\int V(\mathbf{r},\mathbf{r}')\hat{\psi}_H(\mathbf{r}',t)\hat{\psi}_H^\dagger(\mathbf{r}',t)d\mathbf{r}'\ .
\tag{2.20}
$$

By differentiating the Green's function with respect to its first time argument

$$
i\frac{\partial}{\partial t_1}G(1,1') = \frac{\partial}{\partial t_1}\left\langle\hat{T}[\hat{\psi}_H(1)\hat{\psi}_H^\dagger(1')]\right\rangle\ ,
\tag{2.21}
$$

we get

$$
\begin{aligned}
\frac{\partial}{\partial t_1}\left\langle\hat{T}[\hat{\psi}_H(1)\hat{\psi}_H^\dagger(1')]\right\rangle &= \delta(t_1-t_{1'})\left\langle\{\hat{\psi}_H(1),\hat{\psi}_H^\dagger(1')\}\right\rangle + \left\langle\hat{T}\left[\frac{\partial\hat{\psi}_H(1)}{\partial t_1}\hat{\psi}_H^\dagger(1')\right]\right\rangle \\
&= \delta(1-1') + \left\langle\hat{T}\left[\frac{\partial\hat{\psi}_H(1)}{\partial t_1}\hat{\psi}_H^\dagger(1')\right]\right\rangle\ .
\end{aligned}
\tag{2.22}
$$

We now replace Eq. (2.19) for $\partial\hat{\psi}_H(1)/\partial t_1$ to obtain

$$\left(i\frac{\partial}{\partial t_1}+\frac{1}{2m}\nabla_1^2\right)G(1,1') = \delta(1-1') \\ - i\int V(\mathbf{r}_1,\mathbf{r}_2)\left\langle \hat{T}\left[\hat{\psi}_H^\dagger(\mathbf{r}_2,t_1)\hat{\psi}_H(\mathbf{r}_2,t_1)\hat{\psi}_H(1)\hat{\psi}_H^\dagger(1')\right]\right\rangle d\mathbf{r}_2\ . \tag{2.23}$$

Here we recognize the two-particle Green's function

$$\left\langle \hat{T}\left[\hat{\psi}_H^\dagger(\mathbf{r}_2,t_1)\hat{\psi}_H(\mathbf{r}_2,t_1)\hat{\psi}_H(1)\hat{\psi}_H^\dagger(1')\right]\right\rangle = -\left\langle \hat{T}\left[\hat{\psi}_H(1)\hat{\psi}_H(2)\hat{\psi}_H^\dagger(1')\hat{\psi}_H^\dagger(2^+)\right]\right\rangle\Big|_{t_2=t_1} \\ = G_2(12,1'2^+)|_{t_2=t_1}\ , \tag{2.24}$$

so that the equation of motion for the one-particle Green's function reads

$$\left(i\frac{\partial}{\partial t_1}+\frac{1}{2m}\nabla_1^2\right)G(1,1') = \delta(1-1') - i\int V(1,2)\ G_2(12,1'2^+)\big|_{t_2=t_1}\, d2\ . \tag{2.25}$$

Here $V(1,2)=\delta(t_1-t_2)V(\mathbf{r}_1,\mathbf{r}_2)$, and 2^+ stands for $\to t_2^+$. As we see, the one-particle Green's function for interacting identical particles depends on the two-particle Green's function. In analogous way the two-particle Green's function depends on the three-particle Green's function and so on. This is known as the Martin-Schwinger hierarchy [94].

2.2.2 Lehmann representation and spectral functions

Let us consider the one-particle Green's function in Eq. (2.9) for $t_1 > t_1'$

$$G(1,1') = G(\mathbf{r}_1,\mathbf{r}_1',t_1-t_1') = -i\left\langle e^{i\hat{H}t_1}\hat{\psi}(\mathbf{r}_1)e^{-i\hat{H}(t_1-t_1')}\hat{\psi}^\dagger(\mathbf{r}_1\,')e^{-i\hat{H}t_1'}\right\rangle\ . \tag{2.26}$$

Inserting a complete set of eigenstates of $\hat{H}$ and omiting the subscripts 1, 1' we obtain

$$G(\mathbf{r},\mathbf{r}',t-t') = -i\sum_{n,N'}\langle {\Phi_0}^N|\hat{\psi}(\mathbf{r})|\Phi_n^{N'}\rangle\,\langle\Phi_n^{N'}|\hat{\psi}^\dagger(\mathbf{r}')|{\Phi_0}^N\rangle\, e^{-i(E_n^{N'}-E_0^N)(t-t')}\ , \tag{2.27}$$

where $\left|{\Phi_n}^N\right\rangle$ is the n-th state of the N particle system in the Heisenberg picture, which corresponds to an energy E_n^N. In the same way, for $t<t'$ we have

$$G(\mathbf{r},\mathbf{r}',t-t') = i\sum_{n,N'}\langle {\Phi_0}^N|\hat{\psi}^\dagger(\mathbf{r}')|\Phi_n^{N'}\rangle\,\langle\Phi_n^{N'}|\hat{\psi}(\mathbf{r})|{\Phi_0}^N\rangle\, e^{i(E_n^{N'}-E_0^N)(t-t')}\ . \tag{2.28}$$

Since the operator $\hat{\psi}(\mathbf{r})$ decreases the number of particles by one unit and $\hat{\psi}(\mathbf{r})^\dagger$ increases the number of particles by one unit, then in Eq. (2.27) only the terms with $N' = N + 1$ remain. Similarly, in Eq. (2.28) only the terms with $N' = N - 1$ remain. Therefore

$$\begin{aligned} G(\mathbf{r}, \mathbf{r}', t - t') = &- i\theta(t - t') \sum_n \langle {\Phi_0}^N | \hat{\psi}(\mathbf{r}) | \Phi_n^{N+1} \rangle \langle \Phi_n^{N+1} | \hat{\psi}^\dagger(\mathbf{r}') | {\Phi_0}^N \rangle \, e^{-i(E_n^{N+1} - E_0^N)(t-t')} \\ &+ i\theta(t' - t) \sum_n \langle {\Phi_0}^N | \hat{\psi}^\dagger(\mathbf{r}') | \Phi_n^{N-1} \rangle \langle \Phi_n^{N-1} | \hat{\psi}(\mathbf{r}) | {\Phi_0}^N \rangle \, e^{i(E_n^{N-1} - E_0^N)(t-t')} \, . \end{aligned} \tag{2.29}$$

As a means to quantify the change of energy of the system under the addition or removal of a particle, the chemical potentials are introduced as

$$\mu^+ = E_0^{N+1} - E_0^N \, , \tag{2.30a}$$

$$\mu^- = E_0^N - E_0^{N-1} \, . \tag{2.30b}$$

Here μ^+ corresponds to the energy absorbed by the system when a particle is added to the N-particle system, while μ^- corresponds to the energy released from the system when a particle is removed from the N-particle system. Additionally, one defines the excitation energy of the $(N + 1)$-particle system as

$$\varepsilon_n^+ = E_n^{N+1} - E_0^{N+1} \, . \tag{2.31}$$

In the same way one defines the excitation energy of the $(N - 1)$-particle system as

$$\varepsilon_n^- = E_n^{N-1} - E_0^{N-1} \, . \tag{2.32}$$

With these definitions we obtain

$$E_n^{N+1} = E_0^N + \mu^+ + \varepsilon_n^+ \, , \tag{2.33a}$$

$$E_n^{N-1} = E_0^N + \varepsilon_n^- - \mu^- \, . \tag{2.33b}$$

By assuming

$$\varepsilon_n^+ = \varepsilon_n^- \, , \tag{2.34a}$$

$$\mu^+ = \mu^- \equiv \mu \, , \tag{2.34b}$$

one introduces an error of order $1/N$ [3, 43]. At zero temperature, μ corresponds to the Fermi energy of the system denoted as ε_F.

To evaluate the Fourier transform of $G(\mathbf{r},\mathbf{r}',t-t')$ in Eq. (2.29) in the time difference $t-t'$, one needs to evaluate the Fourier transform of the Heaviside step function. An integral of this type is defined as the limit,

$$\int_{-\infty}^{\infty} dt\,\theta(t)e^{i\alpha t} = \lim_{\delta\to 0^+}\int_0^{\infty} dt\,e^{i\alpha t-\delta t} = \lim_{\delta\to 0^+}\frac{i}{\alpha+i\delta}\,. \tag{2.35}$$

In the same way

$$\int_{-\infty}^{\infty} dt\,\theta(-t)e^{i\alpha t} = -\lim_{\delta\to 0^+}\frac{i}{\alpha-i\delta}\,. \tag{2.36}$$

With these considerations, the Fourier transform of the one-particle Green's function reads

$$\begin{aligned} G(\mathbf{r},\mathbf{r}',\omega) = &\sum_n \frac{\langle {\Phi_0}^N|\hat{\psi}(\mathbf{r})|\Phi_n^{N+1}\rangle\,\langle\Phi_n^{N+1}|\hat{\psi}^\dagger(\mathbf{r}')|{\Phi_0}^N\rangle}{\omega-\varepsilon_n-\varepsilon_F+i\eta} \\ &+\sum_n \frac{\langle {\Phi_0}^N|\hat{\psi}^\dagger(\mathbf{r}')|\Phi_n^{N-1}\rangle\,\langle\Phi_n^{N-1}|\hat{\psi}(\mathbf{r})|{\Phi_0}^N\rangle}{\omega+\varepsilon_n-\varepsilon_F-i\eta}\,, \end{aligned} \tag{2.37}$$

where $\eta\to 0^+$ is understood. Eq. (2.37) is known as the Lehmann representation of the one-particle Green's function.

Considering invariance of nuclear matter under translations and rotations in space, then the one-particle Green's function depends on the difference $\mathbf{r}-\mathbf{r}'$. Additionally, it is convenient to work with momentum or k-space representation. Thus, $\hat{\psi}(\mathbf{r}) = e^{-i\hat{\mathbf{P}}\cdot\mathbf{r}}\hat{\psi}(\mathbf{0})e^{i\hat{\mathbf{P}}\cdot\mathbf{r}}$, where $\hat{\mathbf{P}}$ is the momentum operator given by

$$\hat{\mathbf{P}} = \int \hat{\psi}(\mathbf{r})^\dagger(-i\nabla)\hat{\psi}(\mathbf{r})d\mathbf{r}\,. \tag{2.38}$$

Since $\hat{\mathbf{P}}$ is a constant of motion, the complete set of states can also be taken to be eigenstates of the momentum operator, that is $\hat{\mathbf{P}}\,|\Phi_n^{N+1}\rangle = \mathbf{P}_n\,|\Phi_n^{N+1}\rangle$. Setting $\mathbf{P}_0=\mathbf{0}$, the Lehmann representation for the propagator reads

$$\begin{aligned} G(\mathbf{r}-\mathbf{r}',\omega) = &\sum_n \frac{|\,\langle {\Phi_0}^N|\hat{\psi}(\mathbf{0})|\Phi_n^{N+1}\rangle\,|^2 e^{i\mathbf{P}_n\cdot(\mathbf{r}-\mathbf{r}')}}{\omega-\varepsilon_n-\varepsilon_F+i\eta} \\ &+\sum_n \frac{|\,\langle \Phi_n^{N-1}|\hat{\psi}(\mathbf{0})|{\Phi_0}^N\rangle\,|^2 e^{-i\mathbf{P}_n\cdot(\mathbf{r}-\mathbf{r}')}}{\omega+\varepsilon_n-\varepsilon_F-i\eta}\,. \end{aligned} \tag{2.39}$$

Fourier transforming Eq. (2.39) in the difference $(\mathbf{r}-\mathbf{r}')$ yields

$$\begin{aligned} G(\mathbf{p},\omega) =& (2\pi)^3 \sum_n \frac{|\,\langle {\Phi_0}^N|\hat{\psi}(\mathbf{0})|\Phi_n^{N+1}\rangle\,|^2}{\omega-\varepsilon_n-\varepsilon_F+i\eta}\delta(\mathbf{p}+\mathbf{P}_n) \\ &+ (2\pi)^3 \sum_n \frac{|\,\langle \Phi_n^{N-1}|\hat{\psi}(\mathbf{0})|{\Phi_0}^N\rangle\,|^2}{\omega+\varepsilon_n-\varepsilon_F-i\eta}\delta(\mathbf{p}-\mathbf{P}_n)\ . \end{aligned} \tag{2.40}$$

The first term vanishes unless $|\Phi_n^{N+1}\rangle$ is an state with momentum $-\mathbf{p}$. In the same way the second term vanishes unless $|\Phi_n^{N-1}\rangle$ is an state with momentum $\mathbf{p}$. Therefore

$$\begin{aligned} G(\mathbf{p},\omega) =& (2\pi)^3 \sum_{\mathbf{P}_n=-\mathbf{p}} \frac{|\,\langle {\Phi_0}^N|\hat{\psi}(\mathbf{0})|\Phi_n^{N+1}\rangle\,|^2}{\omega-\varepsilon_n-\varepsilon_F+i\eta} \\ &+ (2\pi)^3 \sum_{\mathbf{P}_n=\mathbf{p}} \frac{|\,\langle \Phi_n^{N-1}|\hat{\psi}(\mathbf{0})|{\Phi_0}^N\rangle\,|^2}{\omega+\varepsilon_n-\varepsilon_F-i\eta}\ . \end{aligned} \tag{2.41}$$

The particle $A_p(\mathbf{p},E)$ and hole $A_h(\mathbf{p},E)$ spectral functions are defined

$$\begin{aligned} G(\mathbf{p},\omega) &= \int_0^\infty \left[\frac{A_p(\mathbf{p},\varepsilon_F+E)}{\omega-\varepsilon_F-E+i\eta}+\frac{A_h(\mathbf{p},\varepsilon_F-E)}{\omega-\varepsilon_F+E-i\eta}\right]dE \\ &= \int_{-\infty}^{\varepsilon_F}\frac{A_h(\mathbf{p},E)}{\omega-E-i\eta}dE+\int_{\varepsilon_F}^\infty\frac{A_p(\mathbf{p},E)}{\omega-E+i\eta}dE\ . \end{aligned} \tag{2.42}$$

Taking the imaginary part of $G(\mathbf{p},\omega)$ yields

$$\begin{aligned} A_p(\mathbf{p},E) &= -\frac{1}{\pi}\mathrm{Im}[G(\mathbf{p},E)] = (2\pi)^3\sum_{\mathbf{P}_n=-\mathbf{p}}|\,\langle {\Phi_0}^N|\hat{\psi}(\mathbf{0})|\Phi_n^{N+1}\rangle\,|^2\delta[E-(\varepsilon_F+\varepsilon_n)], \quad E>\varepsilon_F \\ A_h(\mathbf{p},E) &= \frac{1}{\pi}\mathrm{Im}[G(\mathbf{p},E)] = (2\pi)^3\sum_{\mathbf{P}_n=\mathbf{p}}|\,\langle \Phi_n^{N-1}|\hat{\psi}(\mathbf{0})|{\Phi_0}^N\rangle\,|^2\delta[E-(\varepsilon_F-\varepsilon_n)], \qquad E<\varepsilon_F \end{aligned} \tag{2.43}$$

In obtaining the imaginary part we have used the Sokhotski-Plemelj formula

$$\frac{1}{E\pm i\eta} = \mathcal{P}\frac{1}{E}\mp i\pi\delta(E)\ . \tag{2.44}$$

These functions are related to the probability distribution for the transition from the ground state of N particles to the $(N\pm1)$-particle excited states.

The anticonmutator rules for fermionic fields embody important restrictions to spectral functions. Starting from

$$\delta(\mathbf{r}-\mathbf{r}') = \left\langle\{\hat{\psi}(\mathbf{r})\hat{\psi}^\dagger(\mathbf{r}')\}\right\rangle = \langle\hat{\psi}(\mathbf{r})\hat{\psi}^\dagger(\mathbf{r}')\rangle+\langle\hat{\psi}^\dagger(\mathbf{r}')\hat{\psi}(\mathbf{r})\rangle\ , \tag{2.45}$$

we can insert a complete set of eigenstates as done for the one-particle Green's function. In this way one obtains

$$\delta(\mathbf{r}-\mathbf{r}') = \sum_n |\langle \Phi_0^N|\hat{\psi}(\mathbf{0})|\Phi_n^{N+1}\rangle|^2 e^{i\mathbf{P_n}\cdot(\mathbf{r}-\mathbf{r}')} + \sum_n |\langle \Phi_n^{N-1}|\hat{\psi}(\mathbf{0})|\Phi_0^N\rangle|^2 e^{-i\mathbf{P_n}\cdot(\mathbf{r}-\mathbf{r}')} \ . \quad (2.46)$$

Multiplying by $e^{i\mathbf{p}\cdot(\mathbf{r}-\mathbf{r}')}$ and integrating over $(\mathbf{r}-\mathbf{r}')$ we obtain

$$1 = (2\pi)^3 \left(\sum_{\mathbf{P}_n=-\mathbf{p}} |\langle \Phi_0^N|\hat{\psi}(\mathbf{0})|\Phi_n^{N+1}\rangle|^2 + \sum_{\mathbf{P}_n=\mathbf{p}} |\langle \Phi_n^{N-1}|\hat{\psi}(\mathbf{0})|\Phi_0^N\rangle|^2 \right) \ . \quad (2.47)$$

Combining with Eq. (2.43) we get

$$1 = \int_{-\infty}^{\varepsilon_F} A_h(\mathbf{p},E)dE + \int_{\varepsilon_F}^{\infty} A_p(\mathbf{p},E)dE \ , \quad (2.48)$$

result known as the sum rule for spectral functions.

2.2.3 Free Green's function

In the context of this formalism let us examine the case of uncorrelated particles, where we set $V=0$ in Eq. (2.25). Then

$$\left(i\frac{\partial}{\partial t_1} + \frac{1}{2m}\nabla_1^2\right) G_0(1,1') = \delta(1-1') \ , \quad (2.49)$$

where G_0 denotes the free one-particle Green's function. By Fourier transforming the equation of motion in both space and time, we get

$$\left(\omega - \frac{k^2}{2m}\right) G_0(\mathbf{k},\omega) = 1 \ , \quad (2.50)$$

where we have defined

$$G_0(\mathbf{k},\omega) = \int d(t-t') \int d(\mathbf{r}-\mathbf{r}') e^{i[\mathbf{k}\cdot(\mathbf{r}-\mathbf{r}')-\omega(t-t')]} G_0(\mathbf{r}-\mathbf{r}', t-t') \ . \quad (2.51)$$

Therefore

$$G_0(\mathbf{k},\omega) = \frac{1}{\omega - \frac{k^2}{2m}} \ , \quad (2.52)$$

which combined with Eq. (2.42) yields for the spectral functions

$$A_p(\mathbf{k},E) = A_h(\mathbf{k},E) = \delta\left(E - \frac{k^2}{2m}\right) \ . \quad (2.53)$$

The inverse of the $G_0(k,\omega)$ operator is defined such that

$$\int d\mathbf{r}_2 G_0^{-1}(1,2)G_0(2,1') = \delta(1-1') \; , \tag{2.54}$$

so that

$$G_0^{-1}(1,1') = \left(i\frac{\partial}{\partial t_1} + \frac{1}{2m}\nabla_1^2 \right) \delta(1-1') \; . \tag{2.55}$$

Consequently

$$G_0^{-1}(\mathbf{k},\omega) = \omega - \frac{k^2}{2m} \; . \tag{2.56}$$

As we will see, the free one-particle Green's function and it's inverse appear recurrently in many expressions.

2.2.4 Self-energy and Dyson equation

The equation of motion for the one-particle Green's function, as in Eq. (2.25), can be rewritten by removing the two-particle Green's function. This is achieved with the introduction of a one-body operator $\Sigma(1,1')$ called the self-energy and defined as

$$\int d\mathbf{r}_2 \Sigma(1,2)G(2,1') = -i \int V(1,2)G_2(12,1'2^+)\big|_{t_2=t_1} d2 \; . \tag{2.57}$$

In this way, Eq. (2.25) becomes

$$\left(i\frac{\partial}{\partial t_1} + \frac{1}{2m}\nabla_1^2 \right) G(1,1') = \delta(1-1') + \int d2 \; \Sigma(1,2)G(2,1') \; . \tag{2.58}$$

This equation is known as the Dyson equation in differential form. In order to obtain its associated integral equation, we rewrite the above equation as

$$\int d2 \left(i\frac{\partial}{\partial t_1} + \frac{1}{2m}\nabla_1^2 \right) \delta(1-2)G(2,1') = \int d2 \; G_0^{-1}(1,2)G(2,1') = \delta_{11'} + \int d2 \; \Sigma(1,2)G(2,1') \; . \tag{2.59}$$

Multiplying by $G_0(1'',1)$ and integrating over 1 we obtain

$$G(1'',1') = G_0(1'',1') + \int d2 \int d1 G_0(1'',1)\Sigma(1,2)G(2,1') \; . \tag{2.60}$$

In operator form this becomes

$$G = G_0 + G_0 \Sigma G \; . \tag{2.61}$$

In this way, one can solve for the exact one-particle propagator

$$G = (G_0^{-1} - \Sigma)^{-1} \ , \tag{2.62}$$

which projected in $\mathbf{k}$ space yields

$$G(\mathbf{k}, \omega) = \frac{1}{\omega - \frac{k^2}{2m} - \Sigma(\mathbf{k}, \omega)} \ . \tag{2.63}$$

Taking the imaginary part to Eq. (2.63), one finds the spectral function in terms of the self-energy

$$A(\mathbf{k}, \omega) = -\frac{\text{sign}(\omega - \varepsilon_F)}{\pi} \frac{\text{Im}\Sigma(\mathbf{k}, \omega)}{\left(\omega - \frac{k^2}{2m} - \text{Re}\Sigma(\mathbf{k}, \omega)\right)^2 + \left(\text{Im}\Sigma(\mathbf{k}, \omega)\right)^2} \ . \tag{2.64}$$

This result is very useful in the self-consistent scheme that we will introduce as it establishes a direct link between the one-particle Green's function and the self-energy through the spectral function.

2.2.5 Diagrammatic methods

If the Hamiltonian of the system is decomposed as $H = H_0 + H_1$, with H_0 the Hamiltonian of free fermions and H_1 the interaction term, it is possible to expand the Green's function in a perturbation series, in terms of free one-particle Green's functions G_0 and the two-body interaction V. A full derivation can be found in literature [3, 34, 43]. In summary, a time dependent perturbation theory is applied. Using the differential equation for the time evolution operator $\hat{U}$ in the interaction picture, namely

$$i\frac{\partial}{\partial t}\hat{U}(t, t_0) = \hat{H}_1 \hat{U}(t, t_0) \ , \tag{2.65}$$

after integrating and iterating, one obtains

$$\hat{U}(t, t_0) = \sum_{n=0}^{\infty} \frac{(-i)^n}{n!} \int_{t_0}^{t} dt_1 \cdots \int_{t_0}^{t} dt_n \hat{T}[\hat{H}_1(t_1) \cdots \hat{H}_1(t_n)] \ .$$

Here, the time ordering operator $\hat{T}$ introduced in Eq. (2.10) is generalized to include more than two operators. It arranges the operators in such a way that the time arguments decrease from left to right, including a minus sign for each required interchange between two fermion

operators. In the end, the propagator in any one-particle basis becomes

$$G(\alpha,\beta;t,t_0) = -i\sum_{n=0}^{\infty}\frac{(-i)^n}{n!}\int_{t_0}^{t}dt_1\cdots\int_{t_0}^{t}dt_n\left\langle\Psi_0^N\right|\hat{T}[\hat{H}_1(t_1)\cdots\hat{H}_1(t_n)]a_{I\alpha}(t)\alpha^{\dagger}{}_{I\beta}(t_0)\left|\Psi_0^N\right\rangle_C\ , \tag{2.66}$$

where the subscript I in the operators stands for the interaction picture, with C indicating that only connected contributions are considered. Wick's theorem simplifies this expansion leting the time ordered product of field operators be written as products of free Green's functions. In this way, each term in the sum can be represented by a Feynman diagram. Each diagram of order n contains a different arrangement of n interactions. In order to establish a correspondence between each term in the perturbation expansion and a Feynman diagram, a set of rules are introduced.

In this work the free propagator is represented by a single line ($-$), the full propagator is represented by a double fermion line ($=$) and the interaction V is represented by a wavy line ($\sim$). In simple words, each diagram can be understood as an incoming fermion line with momentum $\mathbf{k}$ and energy ω that scatters a given number of times to finally become an outgoing line with the same initial momentum and energy. For example, the Feynman diagrams that contribute to the Green's function up to first order are shown in Fig. 2.3.

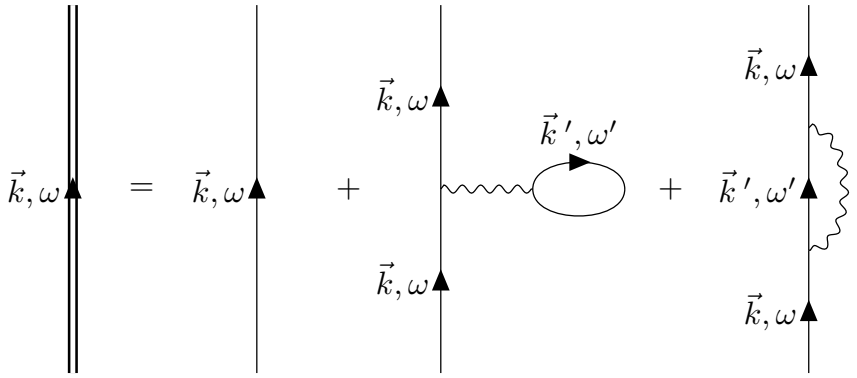

Figure 2.3: Green's function Feynman diagrams up to first order.

In Fig. 2.4 we show all the terms that contribute up to second order to the one-particle Green's function. We note that diagrams (a)-(d) are composed by the repetition of first order diagrams in a sequential way. The diagrams (c)-(h) are also formed by a repetition of two first order diagrams, but one of them is inserted in an intermediate line in another. The only diagrams of second order that cannot be conceived as repetition of first order diagrams are (i) and (j), which are entirely new second order diagrams.

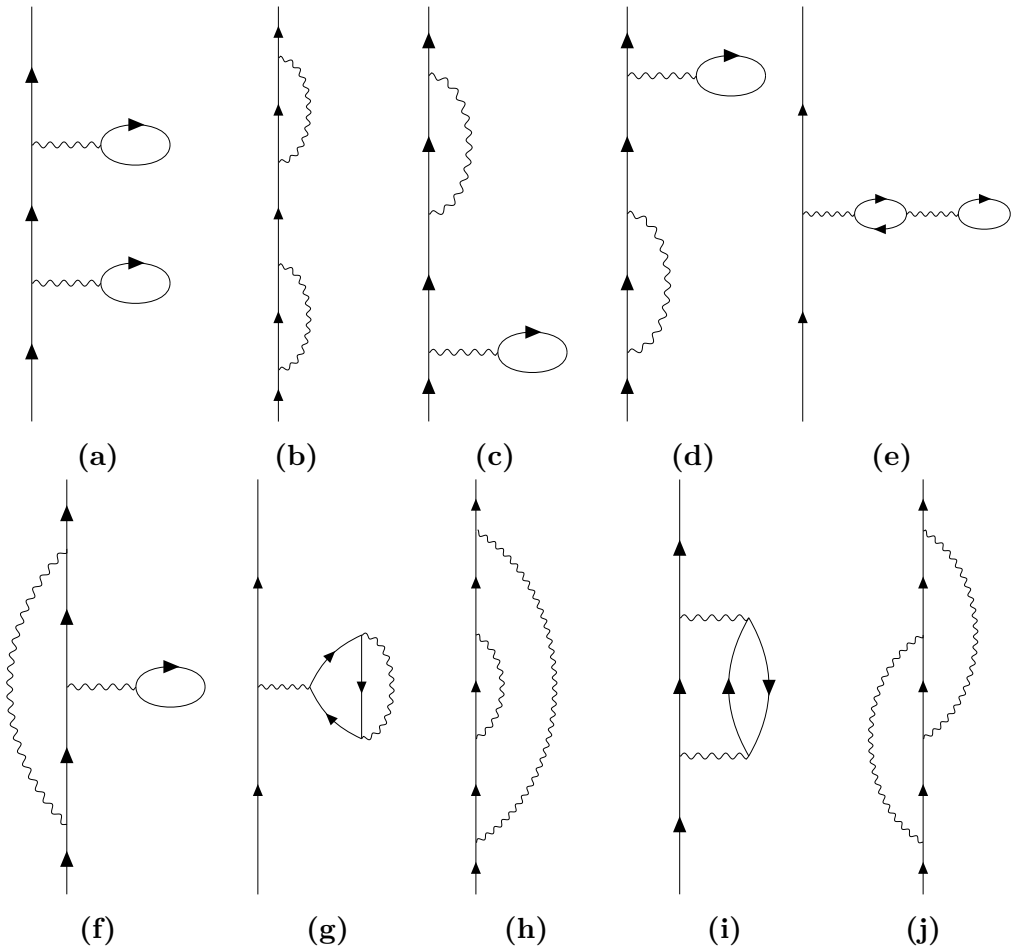

Figure 2.4: Second order diagrams that contribute to the one-particle Green's function.

As expected, the third order diagrams can be obtained by the sequential inclusion of one first order diagram and one second order diagram, or by the insertion of a first order diagram into an intermediate line of a second order diagram and vice versa. There will be, of course, entirely new third order diagrams. This self-contained structure can be studied in detail introducing the reducible and irreducible self-energies, which we discuss below.

The one-particle Green's function contains, at zeroth order the free Green's function G_0 with all remaining terms contained in the reducible self-energy Σ^R. This is graphically represented in Fig. 2.5. A first reorganization of all contributions in the reducible self-energy is obtained by considering only irreducible terms. This means that such diagrams do not contain two or more parts that are only connected by an unperturbed single particle Green's function G_0. The sum of all irreducible terms is known as the irreducible self-energy Σ. The reducible self-energy diagrams can be obtained at all orders by the insertion of irreducible self-energy diagrams, as it is shown in Fig. 2.6. This automatically includes the self contained structure mentioned before.

It can be easily seen from the diagrams that the irreducible self-energy contains the one-particle Green's function. This is represented in Fig. 2.7, corresponding to the Dyson equation (2.61).

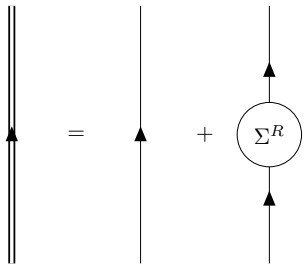

Figure 2.5: Diagrammatic representation of the one-particle propagator.

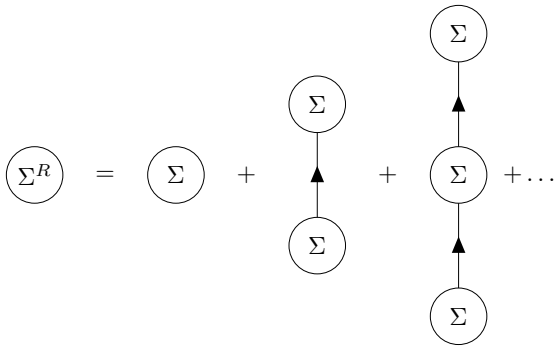

Figure 2.6: Decomposition of the reducible self-energy in terms of irreducible self-energy insertions.

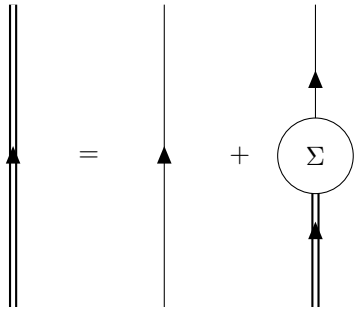

Figure 2.7: Diagrammatic representation of the Dyson equation.

The diagrammatic series expansion discussed here makes it clear that only one-particle irreducible self-energy diagrams need to be considered. However, if one increases the order of the diagrams their structure become more and more complicated. In fact, an exact calculation of all irreducible self-energy diagrams is currently unfeasible, being more convenient to select some dominant diagrams based on physical arguments.

As it was mentioned above, only one-particle irreducible self-energy diagrams need to be considered. Thus, for the rest of this thesis the word self-energy shall refer to the irreducible self-energy Σ, unless stated otherwise.

2.3 The ladder approximation

It is useful at this point to recall that the interaction between two nucleons features a short-range repulsion and long range attraction. When the interparticle separation is much greater than the interaction short-range part, one is dealing with a low-density interacting Fermi gas. In nuclear matter one can consider a saturation density of about $\rho = 0.16$ fm^{-3}, corresponding to an interparticle separation of $r_0 \simeq 1.8$ fm. This interparticle separation compared to the short-range repulsion of the core, of about 0.5 fm, tells us that the nuclear matter can be approximately considered as an interacting low-density Fermi gas. With this in mind, one may expect that two-body collisions in a low-density medium can be related to two-body scattering in free space. Motivated by this, one proceeds in the same way as in free space, summing all ladder diagrams.

2.3.1 Ladder approximation for G_2

The ladder approximation can be expressed in terms of the two-particle Green's function. Starting from the Martin-Schwinger hierarchy for G_2 we have

$$\left(i\frac{\partial}{\partial t_1} + \frac{1}{2m}\nabla_1^2\right) G_2(12,1'2') = \delta(1-1')G(2,2') - \delta(1-2')G(2,1') - i\int V(1,3)G_3(123,1'2'3^+)d3\ . \tag{2.67}$$

This hierarchy is truncated by approximating the three-particle Green's function G_3 in terms of products of one and two-particles Green's functions G and G_2. In this way one expresses G_3 as [53]

$$G_3(123,1'2'3') \simeq G_2(13,1'3')G(2,2') + G_2(13,2'1')G(2,3') + G_2(13,3'2')G(2,1')\ , \tag{2.68}$$

leaving the third particle as spectator of the other two interacting particles. Replacing this approximation in Eq. (2.67) and using the equation of motion for the one-particle Green's function [Eq. (2.25)] one gets

$$\left(i\frac{\partial}{\partial t_1} + \frac{1}{2m}\nabla_1^2\right)\{G_2(12,1'2') + G(1,2')G(2,1') - G(1,1')G(2,2')\} = i\int G(2,3^+)V(1,3)G_2(13,1'2')d3\ . \tag{2.69}$$

Its associated integral equation becomes

$$\begin{aligned} G_2(1''2,1'2') =& G(1'',1')G(2,2') - G(1'',2')G(2,1') \\ &+ i\int d1 \int d3 G_0(1'',1)G(2,3^+)V(1,3)G_2(13,1'2') \ . \end{aligned} \tag{2.70}$$

The diagrammatic representation of this equation is shown in Fig. 2.8.

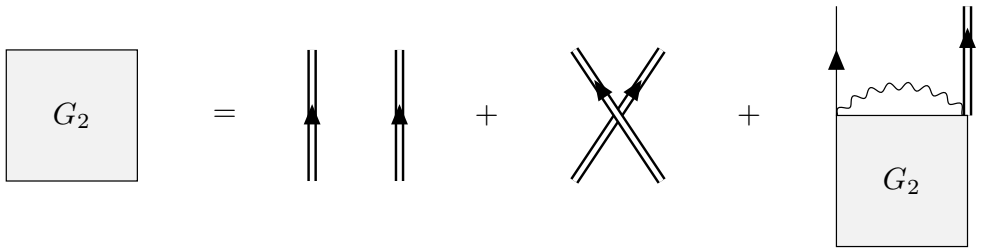

Figure 2.8: Diagrammatic representation of the two-particle Green's function by approximating the three-particle Green's function.

Strictly speaking, Eq. (2.70) does not treat the ladder approximation in a self-consistent way, because of the free one-particle Green's function that appears in the top left vertex of G_2. The ladder structure appears when the free one-particle Green's function is replaced by a full or "dressed" one-particle Green's function [53], as shown in Fig. 2.9 and expressed by

$$\begin{aligned} G_2(12,1'2') =& G(1,1')G(2,2') - G(1,2')G(2,1') \\ &+ i\int d1'' \int d3 G(1,1'')G(2,3^+)V(1'',3)G_2(1''3,1'2') \ . \end{aligned} \tag{2.71}$$

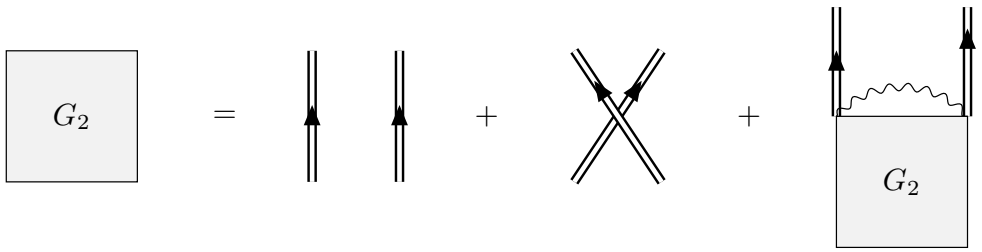

Figure 2.9: Diagrammatic representation of the two-particle Green's function in the ladder approximation.

The iteration of Eq. (2.71) is shown in Fig. 2.10, when one recognizes the ladder structure.

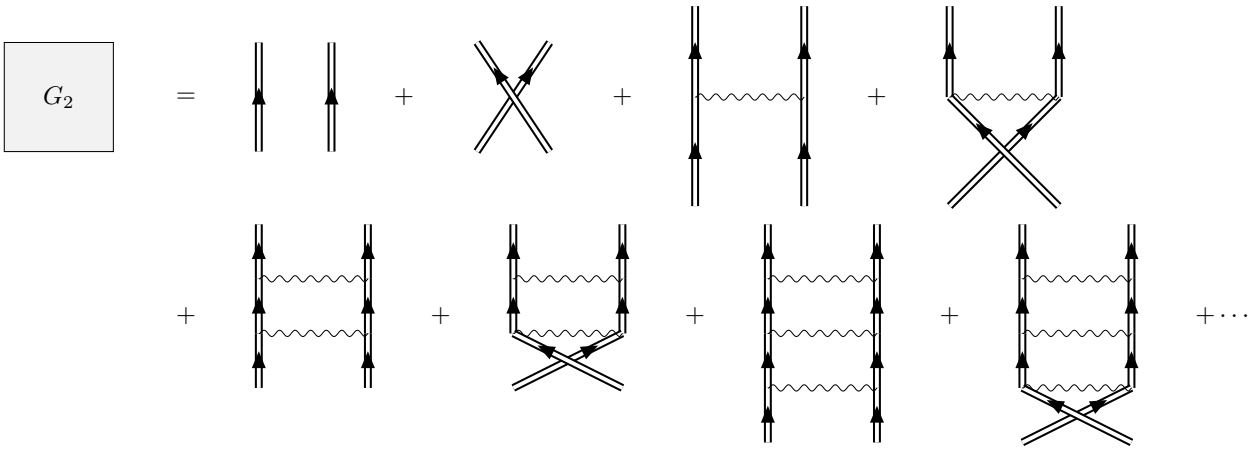

Figure 2.10: Diagrammatic expansion of the two-particle Green's function in the ladder approximation.

2.3.2 Effective interaction or $T-$matrix

In order to solve the equation for the two-particle Green's function within the ladder approximation, one introduces the so-called *in-medium* or effective interaction T matrix [56]

$$\begin{aligned} T(12,1'2') =& \delta(1-1')\delta(2-2')V(1,2) \\ &+ i\int d1''\int d2'' T(12,1''2'')G(1'',1')G(2'',2')V(1',2') \ . \end{aligned} \tag{2.72}$$

Diagrammatically the T matrix can be expressed as in Figs. 2.11 and 2.12. In the low density limit, this matrix reduces to the scattering T matrix.

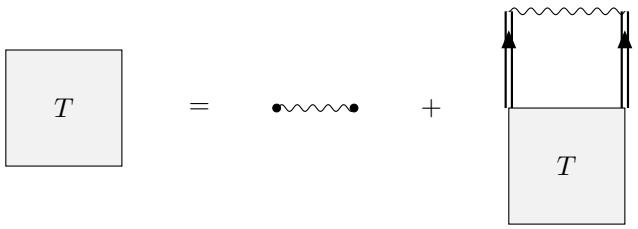

Figure 2.11: Diagrammatic representation of the effective interaction.

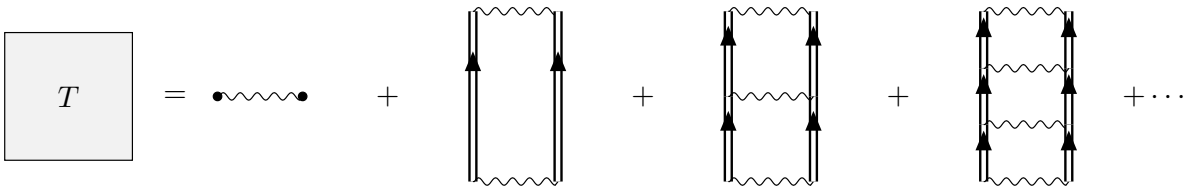

Figure 2.12: Diagrammatic expansion of the effective interaction.

Note that in the definition of the T matrix, the product GG appears. This product is similar to the first term of the expansion for G_2 within the ladder approximation. This term will be denoted G_2^0, as shown in Fig. 2.13 corresponding to

$$G_2^0(12, 1'2') = iG(1, 1')G(2, 2') \ . \tag{2.73}$$

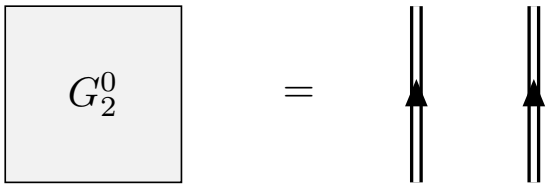

Figure 2.13: Diagrammatic representation of G_2^0.

To obtain a relationship between G_2 and T we write Eqs. (2.71) and (2.72) in matrix form

$$G_2 = GG - GG + iGGVG_2 \ , \tag{2.74a}$$
$$T = V + iTGGV \ , \tag{2.74b}$$

or equivalently

$$(1 - iGGV)G_2 = GG - GG \ , \tag{2.75a}$$
$$T(1 - iGGV) = V \ . \tag{2.75b}$$

Therefore

$$VG_2 = T(GG - GG) \ . \tag{2.76}$$

More explicitly

$$V(1, 2)G_2(12, 1'2') = \int d1'' \int d2'' T(12, 1''2'') \left\{ G(1'', 1')G(2'', 2') - G(1'', 2')G(2'', 1') \right\} \ . \tag{2.77}$$

This equation is interesting as it shows that even if the potential is infinite, T can be finite provided G_2 vanishes at small distances. This may occur in the case of a hard-core potential, where correlations between particles ensure that there can not be particles closer than a distance. The equation is also useful because the product of VG_2 appears explicitly in the equation of motion for the one-particle Green's function G. An equivalent definition of T

can be made if one expands Eq. (2.74b) for T

$$\begin{aligned} T &= V + TG_2^0V = V + VG_2^0V + VG_2^0VG_2^0V + VG_2^0VG_2^0VG_2^0V + \dots \\ &= V + VG_2^0(V + VG_2^0V + VG_2^0VG_2^0V + \dots) \\ &= V + VG_2^0T \ . \end{aligned} \tag{2.78}$$

In terms of matrix elements this is expressed as

$$\begin{aligned} T(12,1'2') =& \delta(1-1')\delta(2-2')V(1,2) \\ &+ \int d1'' \int d2'' V(1,2) G_2^0(12,1''2'') T(1''2'',1'2') \ . \end{aligned} \tag{2.79}$$

Note the similarity with a Lippmann-Schwinger with a dressed two-body propagator G_2^0. Standard numerical techniques to solve integral equations will allow the calculation of the effective interaction by means of Eq. 2.78.

Considering instantaneous interactions, $V(1,2)$ carries a factor $\delta(t_{1'} - t_{2'})$. This enables to express the matrix elements of T as

$$T(12,1'2') = \delta(t_1 - t_2)\delta(t_{1'} - t_{2'}) \left\langle \mathbf{r}_1\mathbf{r}_2 \right| T(t_1 - t_{1'}) \left| \mathbf{r}_{1'}\mathbf{r}_{2'} \right\rangle \ . \tag{2.80}$$

As a result, the temporal Fourier transform of Eq. (2.79) depends only on one energy known as the starting energy. For this reason, G_2^0 is evaluated at $t_1 = t_2$, and $t_{1'} = t_{2'}$, so that

$$\begin{aligned} G_2^0(\mathbf{r}_1t_1,\mathbf{r}_2t_1;\mathbf{r}_{1'}t_{1'},\mathbf{r}_{2'}t_{1'}) &= iG(\mathbf{r}_1 - \mathbf{r}_{1'}, t_1 - t_{1'})G(\mathbf{r}_2 - \mathbf{r}_{2'}, t_1 - t_{1'}) \\ &= \left\langle \mathbf{r}_1\mathbf{r}_2 \right| G_2^0(t_1 - t_{1'}) \left| \mathbf{r}_{1'}\mathbf{r}_{2'} \right\rangle \ . \end{aligned} \tag{2.81}$$

Note that G_2 becomes a function of the difference $t_1 - t_{1'}$.

Applying a Fourier transform in time to Eq. (2.79) yields

$$\begin{aligned} \left\langle \mathbf{r}_1\mathbf{r}_2 \right| T(\omega) \left| \mathbf{r}_{1'}\mathbf{r}_{2'} \right\rangle &= \delta(\mathbf{r}_1 - \mathbf{r}_{1'})\delta(\mathbf{r}_2 - \mathbf{r}_{2'})V(\mathbf{r}_1 - \mathbf{r}_2) \\ + \int d\mathbf{r}_{1''} \int d\mathbf{r}_{2''} V(\mathbf{r}_1 - \mathbf{r}_2) &\left\langle \mathbf{r}_1\mathbf{r}_2 \right| G_2^0(\omega) \left| \mathbf{r}_{1''}\mathbf{r}_{2''} \right\rangle \left\langle \mathbf{r}_{1''}\mathbf{r}_{2''} \right| T(\omega) \left| \mathbf{r}_{1'}\mathbf{r}_{2'} \right\rangle \ , \end{aligned} \tag{2.82}$$

which transformed to momentum variables yields

$$\begin{aligned} \left\langle \mathbf{k}_1\mathbf{k}_2 \right| T(\omega) \left| \mathbf{k}_{1'}\mathbf{k}_{2'} \right\rangle &= \left\langle \mathbf{k}_1\mathbf{k}_2 \right| V \left| \mathbf{k}_{1'}\mathbf{k}_{2'} \right\rangle \\ + \int \frac{d\mathbf{k}_3}{(2\pi)^3} \int \frac{d\mathbf{k}_4}{(2\pi)^3} \int \frac{d\mathbf{k}_{3'}}{(2\pi)^3} \int \frac{d\mathbf{k}_{4'}}{(2\pi)^3} &\left\langle \mathbf{k}_1\mathbf{k}_2 \right| V \left| \mathbf{k}_3\mathbf{k}_4 \right\rangle \left\langle \mathbf{k}_3\mathbf{k}_4 \right| G_2^0(\omega) \left| \mathbf{k}_{3'}\mathbf{k}_{4'} \right\rangle \left\langle \mathbf{k}_{3'}\mathbf{k}_{4'} \right| T(\omega) \left| \mathbf{k}_{1'}\mathbf{k}_{2'} \right\rangle \ . \end{aligned} \tag{2.83}$$

By applying the convolution theorem to Eq. (2.81) for G_2 we have

$$\left\langle \mathbf{r}_1\mathbf{r}_2 \left| G_2^0(\omega) \right| \mathbf{r}_{1'}\mathbf{r}_{2'} \right\rangle = i\int_{-\infty}^{\infty} \frac{dE}{2\pi} G(\mathbf{r}_1 - \mathbf{r}_{1'}, E) G(\mathbf{r}_2 - \mathbf{r}_{2'}, \omega - E) \ , \tag{2.84}$$

leading to

$$\left\langle \mathbf{k}_1\mathbf{k}_2 \left| G_2^0(\omega) \right| \mathbf{k}_{1'}\mathbf{k}_{2'} \right\rangle = i(2\pi)^6 \delta(\mathbf{k}_1 - \mathbf{k}_{1'}) \delta(\mathbf{k}_2 - \mathbf{k}_{2'}) \int_{-\infty}^{\infty} G\left(\mathbf{k}_1 E\right) G\left(\mathbf{k}_2, \omega - E\right) dE \ . \tag{2.85}$$

We replace this result in Eq. (2.83) to obtain

$$\begin{aligned} &\langle \mathbf{k}_1\mathbf{k}_2 \,|\, T(\omega) \,|\, \mathbf{k}_{1'}\mathbf{k}_{2'} \rangle = \langle \mathbf{k}_1\mathbf{k}_2 \,|\, V \,|\, \mathbf{k}_{1'}\mathbf{k}_{2'} \rangle \\ &+ \int \frac{d\mathbf{k}_3}{(2\pi)^3} \int \frac{d\mathbf{k}_4}{(2\pi)^3} \langle \mathbf{k}_1\mathbf{k}_2 \,|\, V \,|\, \mathbf{k}_3\mathbf{k}_4 \rangle \left\langle \mathbf{k}_3\mathbf{k}_4 \left| G_2^0(\omega) \right| \mathbf{k}_3\mathbf{k}_4 \right\rangle \langle \mathbf{k}_3\mathbf{k}_4 \,|\, T(\omega) \,|\, \mathbf{k}_{1'}\mathbf{k}_{2'} \rangle \ . \end{aligned} \tag{2.86}$$

It is convenient at this point to define the center of mass and relative momenta

$$\mathbf{K} = \mathbf{k}_1 + \mathbf{k}_2 \tag{2.87}$$

and

$$\mathbf{k} = \frac{\mathbf{k}_1 - \mathbf{k}_2}{2} \ , \tag{2.88}$$

respectively. Thus, $\langle \mathbf{k}_1\mathbf{k}_2 \,|\, V \,|\, \mathbf{k}_{1'}\mathbf{k}_{2'} \rangle = \delta(\mathbf{K} - \mathbf{K}') \langle \mathbf{k} \,|\, V \,|\, \mathbf{k}' \rangle$. Additionally,

$$\left\langle \mathbf{k}_1\mathbf{k}_2 \left| G_2^0(\mathbf{K}, \omega) \right| \mathbf{k}_1\mathbf{k}_2 \right\rangle = i(2\pi)^6 \int_{-\infty}^{\infty} \frac{dE}{2\pi} G\left(\frac{\mathbf{K}}{2} + \mathbf{k}, E\right) G\left(\frac{\mathbf{K}}{2} - \mathbf{k}, \omega - E\right) \ , \tag{2.89}$$

so that

$$\langle \mathbf{k} \,|\, T(\mathbf{K}, \omega) \,|\, \mathbf{k}' \rangle = \langle \mathbf{k} \,|\, V \,|\, \mathbf{k}' \rangle + \int d\mathbf{p} \, \langle \mathbf{k} \,|\, V \,|\, \mathbf{p} \rangle \, G_2^0(\mathbf{K}, \mathbf{p}, \omega) \, \langle \mathbf{p} \,|\, T(\mathbf{K}, \omega) \,|\, \mathbf{k} \rangle \ . \tag{2.90}$$

Here we have defined

$$G_2^0(\mathbf{K}, \mathbf{k}, \omega) = i\int_{-\infty}^{\infty} \frac{dE}{2\pi} G\left(\frac{\mathbf{K}}{2} + \mathbf{k}, E\right) G\left(\frac{\mathbf{K}}{2} - \mathbf{k}, \omega - E\right) \ . \tag{2.91}$$

Eq. (2.90), in principle, allows to solve for the effective interaction or T matrix in momentum space. The challenge here is to compute the function $G_2^0(\mathbf{K}, \mathbf{k}, \omega)$, the non-interacting two-body dressed propagator.

2.3.3 The non-interacting two-particle dressed propagator

The non-interacting two-particle dressed Green's function G_2^0 can be obtained using the spectral representation of the one-particle propagator in Eq. (2.42). Denoting $\mathbf{k}_\pm = \frac{\mathbf{K}}{2} \pm \mathbf{k}$, after replacing in Eq. (2.91) we get

$$\begin{aligned} G_2^0(\mathbf{K},\mathbf{k},\omega) = i\int_{-\infty}^{\infty} \Bigg(& \int_{-\infty}^{\varepsilon_F}\int_{-\infty}^{\varepsilon_F} \frac{A_h(\mathbf{k}_+,E')A_h(\mathbf{k}_-,E'')}{(E-E'-i\eta)(\omega-E-E''-i\eta)}dE'dE'' \\ & + \int_{-\infty}^{\varepsilon_F}\int_{\varepsilon_F}^{\infty} \frac{A_h(\mathbf{k}_+,E')A_p(\mathbf{k}_-,E'')}{(E-E'-i\eta)(\omega-E-E''+i\eta)}dE'dE'' \\ & + \int_{\varepsilon_F}^{\infty}\int_{-\infty}^{\varepsilon_F} \frac{A_p(\mathbf{k}_+,E')A_h(\mathbf{k}_-,E'')}{(E-E'+i\eta)(\omega-E-E''-i\eta)}dE'dE'' \\ & + \int_{\varepsilon_F}^{\infty}\int_{\varepsilon_F}^{\infty} \frac{A_p(\mathbf{k}_+,E')A_p(\mathbf{k}_-,E'')}{(E-E'+i\eta)(\omega-E-E''+i\eta)}dE'dE'' \Bigg) \frac{dE}{2\pi} \ . \end{aligned} \tag{2.92}$$

By contour integration in the complex energy plane we have

$$\begin{aligned} \int_{-\infty}^{\infty} \frac{1}{(E-E'\pm i\eta)(\omega-E-E''\pm i\eta)}dE &= \mp\frac{2\pi i}{\omega-E'-E''\pm i\eta} \ , \\ \int_{-\infty}^{\infty} \frac{1}{(E-E'\pm i\eta)(\omega-E-E''\mp i\eta)}dE &= 0 \ , \end{aligned} \tag{2.93}$$

which used in Eq. 2.92 for $G_2^0(\mathbf{K},\mathbf{k},\omega)$ we obtain

$$\begin{aligned} G_2^0(\mathbf{K},\mathbf{k},\omega) = & \int_{\varepsilon_F}^{\infty}\int_{\varepsilon_F}^{\infty} \frac{A_p(\mathbf{k}_+,E)A_p(\mathbf{k}_-,E')}{\omega-E-E'+i\eta}dEdE' \\ & - \int_{-\infty}^{\varepsilon_F}\int_{-\infty}^{\varepsilon_F} \frac{A_h(\mathbf{k}_+,E)A_h(\mathbf{k}_-,E')}{\omega-E-E'-i\eta}dEdE' \ . \end{aligned} \tag{2.94}$$

As one can see, it is composed by two terms. The first term contains a particle-particle (p-p) propagation, while the second term contains a hole-hole (h-h) propagation. The terms will be denoted G_{2pp}^0 and G_{2hh}^0, respectively. Therefore

$$G_2^0(\mathbf{K},\mathbf{k},\omega) = G_{2pp}^0(\mathbf{K},\mathbf{k},\omega) - G_{2hh}^0(\mathbf{K},\mathbf{k},\omega) \ . \tag{2.95}$$

It will be useful to compute the imaginary part of G_2^0. From Eq. (2.94) we obtain

$$\begin{aligned} \text{Im}\ G_2^0(\mathbf{K},\mathbf{k},\omega) = & -\theta(\omega-2\varepsilon_F)\pi\int_{\varepsilon_F}^{\omega-\varepsilon_F} A_p(\mathbf{k}_+,E)A_p(\mathbf{k}_-,\omega-E)dE \\ & -\theta(2\varepsilon_F-\omega)\pi\int_{\omega-\varepsilon_F}^{\varepsilon_F} A_h(\mathbf{k}_+,E)A_h(\mathbf{k}_-,\omega-E)dE \ . \end{aligned} \tag{2.96}$$

Its real part can be obtained by a dispersion relation

$$\mathrm{Re}G_2^0(\mathbf{K},\mathbf{k},\omega) = \frac{1}{\pi}\mathcal{P}\int_{-\infty}^{2\varepsilon_F} \frac{\mathrm{Im}G_2^0(\mathbf{K},\mathbf{k},E)}{\omega - E}dE - \frac{1}{\pi}\mathcal{P}\int_{2\varepsilon_F}^{\infty} \frac{\mathrm{Im}G_2^0(\mathbf{K},\mathbf{k},E)}{\omega - E}dE \ , \tag{2.97}$$

as may be readily verified from the real part of equation (2.94). The dispersion relation can be expressed in a single formula as

$$G_2^0(\mathbf{K},\mathbf{k},\omega) = \frac{1}{\pi}\int_{-\infty}^{2\varepsilon_F} \frac{\mathrm{Im}\ G_2^0(\mathbf{K},\mathbf{k},E)}{\omega - E - i\eta}dE - \frac{1}{\pi}\int_{2\varepsilon_F}^{\infty} \frac{\mathrm{Im}\ G_2^0(\mathbf{K},\mathbf{k},E)}{\omega - E + i\eta}dE \ . \tag{2.98}$$

This relation is very useful since it enables us to calculate the real part of a complicated function from its imaginary part. As observed in Eq. (2.96), the calculation of Im G_2^0 requires the evaluation of a single energy integral.

2.3.4 The ladder self-energy

As discussed above, the T matrix is directly related to the two-particle Green's function G_2 in the ladder approximation. The equations presented on this section will become very useful to obtain the self-energy within this approximation, hereafter denoted as Σ_L. Replacing Eq. (2.77) in Eq. (2.57) yields

$$\begin{aligned} &\int \Sigma_L(1,2)G(2,1')d2 \\ &= -i\int d2 \int d1'' \int d2'' T(12,1''2'') \left\{G(1'',1')G(2'',2^+) - G(1'',2^+)G(2'',1')\right\}|_{t_2=t_1} \ . \end{aligned} \tag{2.99}$$

After some manipulation, this equation can be rewritten as

$$\int \Sigma_L(1,2)G(2,1')d2 = -i\int d2 \int d1'' \int d2'' \left\{T(12'',21'') - T(12'',1''2)\right\} G(1'',2''^+)G(2,1')|_{t_{2''}=t_1} \ . \tag{2.100}$$

Therefore

$$\Sigma_L(1,2) = -i\int d1'' \int d2'' \left\langle 12''|T|21''\right\rangle_A G(1'',2''^+)|_{t_{2''}=t_1} \ , \tag{2.101}$$

where the subscript A stands for antisymmetrization, namely

$$\left\langle 12|T|1'2'\right\rangle_A = T(12,1'2') - T(12,2'1') \ . \tag{2.102}$$

The self-energy within the ladder approximation is represented diagrammatically in Fig. 2.14.

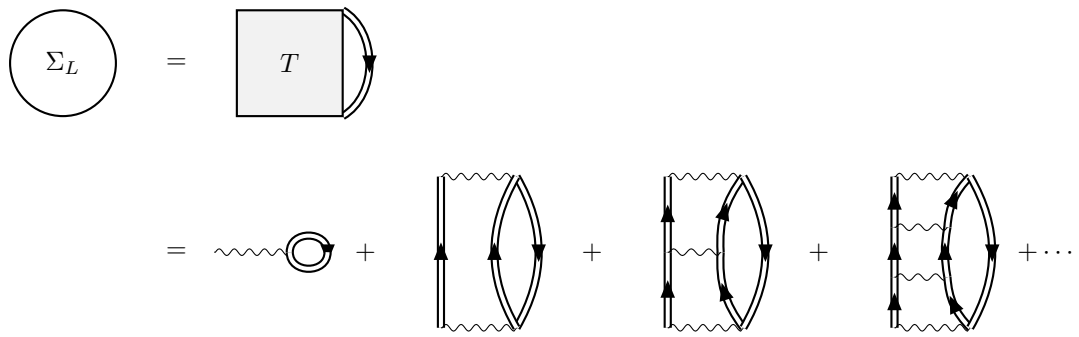

Figure 2.14: Diagrammatic representation of the ladder self-energy Σ_L.

From Eq. (2.101) one has

$$\langle \mathbf{r}_1 \,|\, \Sigma_L(t_1 - t_2) \,|\, \mathbf{r}_2 \rangle = -i \int d\mathbf{r}_{1'} \int d\mathbf{r}_{2'} \, \langle \mathbf{r}_1 \mathbf{r}_{2'} | T(t_1 - t_2) | \mathbf{r}_2 \mathbf{r}_{1'} \rangle_A \, G(\mathbf{r}_{1'} - \mathbf{r}_{2'}, t_2 - t_1^+) \; . \quad (2.103)$$

By Fourier transforming in time and space we obtain

$$\langle \mathbf{k}_1 \,|\, \Sigma_L(\omega) \,|\, \mathbf{k}_2 \rangle = -i \int \frac{d\mathbf{k}'}{(2\pi)^3} \int \frac{dE}{2\pi} e^{iE\delta} \, \langle \mathbf{k}_1 \mathbf{k}' | T(\omega + E) | \mathbf{k}_2 \mathbf{k}' \rangle_A \, G(\mathbf{k}', E) \; , \quad (2.104)$$

where $\delta \to 0^+$. Making use of momentum conservation in the T matrix and expressing it in terms of the center-of-mass and relative momenta, we obtain

$$\Sigma_L(\mathbf{k}, \omega) = -i \int \frac{d\mathbf{k}'}{(2\pi)^3} \int \frac{dE}{2\pi} e^{iE\delta} \left\langle \frac{\mathbf{k} - \mathbf{k}'}{2} \right| T_{\mathbf{k}+\mathbf{k}'}(\omega + E) \left| \frac{\mathbf{k} - \mathbf{k}'}{2} \right\rangle_A G(\mathbf{k}', E) \; . \quad (2.105)$$

In order to compute Σ_L as in Eq. (2.105) it is convenient to keep in mind the analytic structure of the T matrix. A dispersion relation holds as a result of the Lehmann representation of the two-time two-particle propagator [34]

$$T(\omega) = V + \frac{1}{\pi} \int_{-\infty}^{2\varepsilon_F} \frac{\mathrm{Im}\, T(E)}{\omega - E - i\eta} dE - \frac{1}{\pi} \int_{2\varepsilon_F}^{\infty} \frac{\mathrm{Im}\, T(E)}{\omega - E + i\eta} dE \; . \quad (2.106)$$

Replacing this in Eq. (2.105) together with the Lehmann representation of G [Eq. (2.42)] we find for the first energy-independent (Hartree-Fock) term

$$\Sigma_{HF}(\mathbf{k}) = \int \frac{d\mathbf{k}'}{(2\pi)^3} \left\langle \frac{\mathbf{k} - \mathbf{k}'}{2} \right| V \left| \frac{\mathbf{k} - \mathbf{k}'}{2} \right\rangle_A n(\mathbf{k}') \; . \quad (2.107)$$

In the above we have used

$$-\frac{i}{2\pi} \int e^{iE\delta} G(\mathbf{k}, E) dE = \int_{-\infty}^{\varepsilon_F} A_h(\mathbf{k}, E) dE \equiv n(\mathbf{k}) \; , \quad (2.108)$$

where we have introduced the momentum occupation number

$$n(\mathbf{k}) = \int_{-\infty}^{\varepsilon_F} A_h(\mathbf{k},\omega)d\omega \ . \tag{2.109}$$

The next term in Eq. (2.105) is given by

$$\Sigma_{\uparrow}(\mathbf{k},\omega) = -\frac{i}{2\pi^2}\int e^{iE\delta}dE\int_{-\infty}^{2\varepsilon_F} dE'\int \frac{d\mathbf{k}'}{(2\pi)^3}\left\langle \frac{\mathbf{k}-\mathbf{k}'}{2}\right| \mathrm{Im}T_{\mathbf{k}+\mathbf{k}'}(E')\left|\frac{\mathbf{k}-\mathbf{k}'}{2}\right\rangle_A \frac{G(\mathbf{k}',E)}{\omega+E-E'-i\eta} \ . \tag{2.110}$$

Considering that

$$\int \frac{G(\mathbf{k}',E)e^{iE\delta}}{\omega+E-E'-i\eta}dE = -2\pi i\int_{\varepsilon_F}^{\infty} dE''\frac{A_p(\mathbf{k}',E'')}{\omega+E''-E'-i\eta} \ , \tag{2.111}$$

then

$$\Sigma_{\uparrow}(\mathbf{k},\omega) = -\frac{1}{\pi}\int_{-\infty}^{2\varepsilon_F} dE'\int_{\varepsilon_F}^{\infty} dE''\int \frac{d\mathbf{k}'}{(2\pi)^3}\left\langle \frac{\mathbf{k}-\mathbf{k}'}{2}\right| \mathrm{Im}T_{\mathbf{k}+\mathbf{k}'}(E')\left|\frac{\mathbf{k}-\mathbf{k}'}{2}\right\rangle_A \frac{A_p(\mathbf{k}',E'')}{\omega+E''-E'-i\eta} \ . \tag{2.112}$$

Here the up arrow ($\uparrow$) indicates that the function has a pole in the upper-half complex-energy plane. From this equation we also notice that the pole exists for energies below the Fermi energy. Analogously, the last term in Eq. (2.105) yields

$$\Sigma_{\downarrow}(\mathbf{k},\omega) = -\frac{1}{\pi}\int_{2\varepsilon_F}^{\infty} dE'\int_{-\infty}^{\varepsilon_F} dE''\int \frac{d\mathbf{k}'}{(2\pi)^3}\left\langle \frac{\mathbf{k}-\mathbf{k}'}{2}\right| \mathrm{Im}T_{\mathbf{k}+\mathbf{k}'}(E')\left|\frac{\mathbf{k}-\mathbf{k}'}{2}\right\rangle_A \frac{A_h(\mathbf{k}',E'')}{\omega+E''-E'+i\eta} \ , \tag{2.113}$$

with poles in the lower-half complex-energy plane, indicated by the down arrow ($\downarrow$), at energies above the Fermi-energy. This self-energy also fulfills a dispersion relation [34] given by

$$\Sigma_L(\omega) = \Sigma_{HF} + \frac{1}{\pi}\int_{-\infty}^{\varepsilon_F}\frac{\mathrm{Im}\ \Sigma_L(E)}{\omega-E-i\eta}dE - \frac{1}{\pi}\int_{\varepsilon_F}^{\infty}\frac{\mathrm{Im}\ \Sigma_L(E)}{\omega-E+i\eta}dE \ . \tag{2.114}$$

The imaginary part of $\Sigma_{\uparrow}$ and $\Sigma_{\downarrow}$ are given by

$$\begin{aligned}
\mathrm{Im}\ \Sigma_{\downarrow}(\mathbf{k},\omega) =& \theta(\omega-\varepsilon_F)\int_{2\varepsilon_F-\omega}^{\varepsilon_F} dE''\int \frac{d\mathbf{k}'}{(2\pi)^3}\left\langle \frac{\mathbf{k}-\mathbf{k}'}{2}\right| \mathrm{Im}\ T_{\mathbf{k}+\mathbf{k}'}(\omega+E'')\left|\frac{\mathbf{k}-\mathbf{k}'}{2}\right\rangle_A A_h(\mathbf{k}',E'') \ , \\
\mathrm{Im}\ \Sigma_{\uparrow}(\mathbf{k},\omega) =& -\theta(\varepsilon_F-\omega)\int_{\varepsilon_F}^{2\varepsilon_F-\omega} dE''\int \frac{d\mathbf{k}'}{(2\pi)^3}\left\langle \frac{\mathbf{k}-\mathbf{k}'}{2}\right| \mathrm{Im}\ T_{\mathbf{k}+\mathbf{k}'}(\omega+E'')\left|\frac{\mathbf{k}-\mathbf{k}'}{2}\right\rangle_A A_p(\mathbf{k}',E'') \ .
\end{aligned} \tag{2.115}$$

These relations enable us to calculate the imaginary part of $\Sigma_L(\omega)$ from

$$\text{Im } \Sigma_L(\omega) = \text{Im } \Sigma_\downarrow(\mathbf{k},\omega) + \text{Im } \Sigma_\uparrow(\mathbf{k},\omega) \ , \tag{2.116}$$

and the real part can be evaluated using the dispersion relation from Eq. (2.114), namely

$$\text{Re } \Sigma_L(\omega) = \Sigma_{HF} + \frac{1}{\pi}\mathcal{P}\int_{-\infty}^{\varepsilon_F} \frac{\text{Im } \Sigma_L(E)}{\omega - E} dE - \frac{1}{\pi}\mathcal{P}\int_{\varepsilon_F}^{\infty} \frac{\text{Im } \Sigma_L(E)}{\omega - E} dE \ . \tag{2.117}$$

For our purposes we have found an expedite way to compute the self-energy. First, the Hartree-Fock term is calculated, together with the imaginary part of the energy-dependent term. Then, the dispersion relation is used to obatin the real part of Σ_L.

2.4 Brueckner-Hartree-Fock approximation

The BHF approximation was developed in the 50's by Brueckner and collaborators [22, 23]. This was one of the first successful theories in describing nuclear matter properties starting from microscopic NN interactions.

Goldstone showed that one can make an expansion of the ground state energy of the system in terms of time ordered diagrams. Then, wherever there is a hole line in a diagram, there is an integral in an internal variable $\mathbf{p}$, over $p < k_F$. At low densities, as $n \sim k_F^3$, then k_F is small and contributions from hole-lines are assumed to be very small compared to contributions from particle lines. Therefore, the dominant diagrams will be those with the least number of hole diagrams.

In order to sum these diagrams one introduces the Brueckner reaction matrix or g matrix, similar to the T matrix discussed before. This g matrix also fulfills a Lippmann-Schwinger-type equation. It is convenient for the aim of this Thesis to modify the equations seen above to obtain the BHF scheme. This can be done neglecting the hole-hole propagation in G_2^0 together with a quasi-particle approximation for the spectral functions, given by

$$A(\mathbf{k},\omega) = \delta[\omega - e(\mathbf{k})] \ , \tag{2.118}$$

where the quasi-particle spectrum $e(\mathbf{k})$ is obtained by solving

$$e(\mathbf{k}) = \frac{k^2}{2m} + \text{Re } \Sigma[\mathbf{k}, e(\mathbf{k})] \ . \tag{2.119}$$

This approximation is equivalent to neglecting the imaginary part of the self-energy. The above leads to the following two-particle Green's function

$$\lambda(\mathbf{K},\mathbf{k},\omega) = \frac{\theta[e(\mathbf{k}_+)-\varepsilon_F]\theta[e(\mathbf{k}_-)-\varepsilon_F]}{\omega - e(\mathbf{k}_+) - e(\mathbf{k}_-) + i\eta} \ , \tag{2.120}$$

which is used to solve for the g-matrix through the equation

$$g = V + V\lambda g \ . \tag{2.121}$$

Then the single-particle energy (sp) is determined by Eq. (2.119), but only for hole states ($k < k_F$) [16]. For sp momenta k above k_F one can choose a suitable sp energy to improve the convergence of the series. One possible choice emerges naturally from the Green's function prescription and consist in considering Eq. (2.119) both for particles and holes. With this choice one obtains a continuous spectrum, which is why it is called "continuous choice".

For the self-energy, if the hole-hole propagation is neglected, then Im $g(\omega)=0$, for $\omega < 2\varepsilon_F$ (Eq. (2.96)), and the g matrix reads

$$g(\omega) = V - \frac{1}{\pi}\int_{2\varepsilon_F}^{\infty} \frac{\text{Im } g(E)}{\omega - E + i\eta} dE \ . \tag{2.122}$$

The term $\Sigma_\uparrow(\mathbf{k},\omega)$ vanishes so that the BHF self-energy Σ_{BHF} becomes

$$\Sigma_{BHF}(\mathbf{k},\omega) = \Sigma_{HF}(\mathbf{k}) + \Sigma_\downarrow(\mathbf{k},\omega) \ . \tag{2.123}$$

Therefore

$$\begin{aligned}
\Sigma_{BHF}(\mathbf{k},\omega) = &\int_{-\infty}^{\varepsilon_F} \int d\mathbf{k}' \left\langle \frac{\mathbf{k}-\mathbf{k}'}{2} \right| V \left| \frac{\mathbf{k}-\mathbf{k}'}{2} \right\rangle_A A_h(\mathbf{k}', E'') dE'' \\
&- \frac{1}{\pi}\int_{2\varepsilon_F}^{\infty} dE' \int_{-\infty}^{\varepsilon_F} dE'' \int d\mathbf{k}' \left\langle \frac{\mathbf{k}-\mathbf{k}'}{2} \right| \text{Im} g_{\mathbf{k}+\mathbf{k}'}(E') \left| \frac{\mathbf{k}-\mathbf{k}'}{2} \right\rangle_A \frac{A_h(\mathbf{k}', E'')}{\omega + E'' - E' + i\eta} \\
= &\int_{-\infty}^{\varepsilon_F} dE'' \int d\mathbf{k}' \left\langle \frac{\mathbf{k}-\mathbf{k}'}{2} \right| g_{\mathbf{k}+\mathbf{k}'}(\omega + E'') \left| \frac{\mathbf{k}-\mathbf{k}'}{2} \right\rangle_A A_h(\mathbf{k}', E'') \ .
\end{aligned} \tag{2.124}$$

Since we are considering quasi-particle spectral functions, $A_h(\mathbf{k},\omega) = \delta[\omega - e(\mathbf{k})]$. With this the BHF self-energy becomes

$$\Sigma_{BHF}(\mathbf{k},\omega) = \int_{e(\mathbf{k}')<e_F} d\mathbf{k}' \left\langle \frac{\mathbf{k}-\mathbf{k}'}{2} \right| g_{\mathbf{k}+\mathbf{k}'}[\omega + e(\mathbf{k}')] \left| \frac{\mathbf{k}-\mathbf{k}'}{2} \right\rangle_A \ . \tag{2.125}$$

In this scheme, self-consistency is achieved in terms of the quasi-particle energy spectrum $e(\mathbf{k})$, so it is sufficient to compute the on-shell self-energy

$$U(\mathbf{k}) = \text{Re}\ \Sigma_{BHF}[\mathbf{k}, e(\mathbf{k})]\ , \tag{2.126}$$

usually called the sp potential.

The theoretical framework presented in the preceding sections allow us to depart from the BHF approach in the continuous choice, with the inclusion of the imaginary part of the self-energy in the spectral functions.

2.5 Energy of the system

The energy of the system, as given by the energy per nucleon, as a function of the density of the system is known as the equation of state. In the case of symmetric nuclear matter, it allows to predict the saturation point of the system, therefore it is used to asses many-body theories and calculations. On the other hand, the equation of state of pure neutron matter has important implications for the description of the mass-radius relation in neutron stars in hydrostatic equilibrium.

The energy of the system can be expressed as

$$\langle \hat{H} \rangle = \int \frac{d\mathbf{p}}{(2\pi)^3} \frac{p^2}{2m} \left\langle \psi^\dagger(\mathbf{p},t)\psi(\mathbf{p},t) \right\rangle + \frac{1}{2} \iint \frac{d\mathbf{p}}{(2\pi)^3} \frac{d\mathbf{p}'}{(2\pi)^3} V(\mathbf{p},\mathbf{p}') \left\langle \psi^\dagger(\mathbf{p},t)\psi^\dagger(\mathbf{p}',t)\psi(\mathbf{p}',t)\psi(\mathbf{p},t) \right\rangle\ . \tag{2.127}$$

The one- and two-particle Green's functions can be identified as

$$\left\langle \psi^\dagger(\mathbf{p},t)\psi(\mathbf{p},t) \right\rangle = -i \lim_{t' \to t^+} G(\mathbf{p}t, \mathbf{p}t')\ , \tag{2.128}$$

and

$$\left\langle \psi^\dagger(\mathbf{p},t)\psi^\dagger(\mathbf{p}',t)\psi(\mathbf{p}',t)\psi(\mathbf{p},t) \right\rangle = \lim_{t' \to t^+} G_2(\mathbf{p}'t, \mathbf{p}t; \mathbf{p}t', \mathbf{p}'t')\ . \tag{2.129}$$

From the equation of motion for G in momentum space (Eq. (2.25)), it can be obtained that

$$\lim_{t' \to t^+} \int \frac{d\mathbf{p}'}{(2\pi)^3} V(\mathbf{p},\mathbf{p}') G_2(\mathbf{p}'t, \mathbf{p}t; \mathbf{p}t', \mathbf{p}'t^+) = \frac{\partial}{\partial t} G(\mathbf{p}t, \mathbf{p}t^+) + i \frac{p^2}{2m} G(\mathbf{p}t, \mathbf{p}t^+)\ . \tag{2.130}$$

Therefore

$$\langle \hat{H} \rangle = \frac{1}{2} \int \frac{d\mathbf{p}}{(2\pi)^3} \left[-i \frac{p^2}{2m} G(\mathbf{p}t, \mathbf{p}t^+) + \frac{\partial}{\partial t} G(\mathbf{p}t, \mathbf{p}t^+) \right]\ .$$

The one-time one-particle Green's function is evaluated as

$$G(\mathbf{p}t, \mathbf{p}t^+) = \int \frac{d\omega}{2\pi} G(\mathbf{p}, \omega) e^{-\omega(t-t^+)i} = i \int_{-\infty}^{\varepsilon_F} A_h(\mathbf{p}, \omega) d\omega \ , \tag{2.131}$$

so that

$$\frac{\partial}{\partial t} G(\mathbf{p}t, \mathbf{p}t^+) = -i \int \frac{d\omega}{2\pi} \omega G(\mathbf{p}, \omega) e^{-\omega(t-t^+)i} = \int_{-\infty}^{\varepsilon_F} \omega A_h(\mathbf{p}, \omega) d\omega \ . \tag{2.132}$$

Here the Lehmann representation [Eq. (2.42)] for the one-particle Green's function was used. The energy per particle is obtained by dividing the energy by the density of the system. Additionally, the spin and isospin quantum numbers must be accounted for, therefore a degeneracy factor ν appears in the formula, where $\nu = 2$ (4), for neutron (isospin-symmetric nuclear) matter. With this the Galistkii-Midgal-Koltun [47, 57] sum rule is obtained,

$$\frac{E_{\mathrm{SCGF}}}{N} = \frac{\nu}{\rho} \int \frac{d\mathbf{p}}{(2\pi)^3} \int_{-\infty}^{\varepsilon_F} d\omega \frac{1}{2} \left(\frac{p^2}{2m} + \omega \right) A_h(\mathbf{p}, \omega) \ . \tag{2.133}$$

The BHF internal energy is recovered by introducing the quasi-particle approximation for the spectral function, resulting in

$$\begin{aligned} \frac{E_{\mathrm{BHF}}}{N} &= \frac{\nu}{\rho} \int_{e(\mathbf{p})<\varepsilon_F} \frac{d\mathbf{p}}{(2\pi)^3} \frac{1}{2} \left[\frac{p^2}{2m} + e(\mathbf{p}) \right] \\ &= \frac{\nu}{\rho} \int_{e(\mathbf{p})<\varepsilon_F} \frac{d\mathbf{p}}{(2\pi)^3} \left[\frac{p^2}{2m} + \frac{1}{2} U(\mathbf{p}) \right] \ . \end{aligned} \tag{2.134}$$

Chapter 3

In-medium bound states in nuclear matter

It is a well known fact that there is a single two-nucleon bound state between a proton and a neutron in vacuum: the deuteron. In principle, deuterons could also exist in an infinite nuclear system. Actually, *in-medium* deuterons are found within BHF in low-density symmetrical nuclear matter [10]. In the case of neutrons the situation is drastically different. There is no bound state of two neutrons in free space, despite the attractive interaction between them. However, it is possible that they bound together when they are in the nuclear medium, as it is also found for low density neutron and symmetrical nuclear matter within BHF [10, 54].

In this section, we review aspects of di-nucleons within BHF approximation. Along the same line we investigate the possible occurrence of these bound states in the context of SCGF theory.

3.1 Di-nucleons within BHF

Results presented in this section are based on Refs. [10, 54]. The starting point of these studies is the appeareance of singularities in the g matrix at low densities. According to Eq. (2.125), these singularities make the evaluation of the self-energy difficult. However, Arellano showed that the BHF self-energy is finite, therefore the integral of Eq. (2.125) should be feasible.

Theoretically, the g matrix is related to the *in-medium* scattering between two-nucleons. The relevant two-body propagator within BHF is given by Eq. (2.120), which can be expressed as

$$\lambda(\omega) = Q(\omega - h_1 - h_2 + i\eta)^{-1} \,, \tag{3.1}$$

where Q is the Pauli blocking, which acts in the following way over momentum states

$$Q\,|\mathbf{k}_1,\mathbf{k}_2\rangle = \theta(k_1-k_F)\theta(k_2-k_F)\,|\mathbf{k}_1,\mathbf{k}_2\rangle\ . \tag{3.2}$$

Furthermore, h_1 and h_2 are the single particle effective Hamiltonians for particles with momenta $\mathbf{k}_1$ and $\mathbf{k}_2$, respectively. In momentum representation one has

$$h_{1,2} = \frac{k_{1,2}^2}{2m} + U(k_{1,2})\ . \tag{3.3}$$

On the other hand, the equation for the g matrix reads

$$g = V + g\lambda V\ . \tag{3.4}$$

One can rewrite this equation in the following way

$$g = V + VG_{II}V\ , \tag{3.5}$$

where the operator G_{II} has been introduced, which should satisfy the equation

$$G_{II} = \lambda + \lambda V G_{II} = (\lambda(\omega)^{-1} - V)^{-1}\ . \tag{3.6}$$

In this way, the relation $VG_{II} = g\lambda$ is fulfilled. The two-particle Green's function within the ladder approximation is related to this operator as follows

$$iG_2(12,1'2') = G_{II}(12,1'2') - G_{II}(12,2'1')\ . \tag{3.7}$$

From Eq. (3.1) one finds

$$G_{II}(\omega) = Q(\omega - H + i\eta)^{-1}\ , \tag{3.8}$$

where $H = h_1 + h_2 + V$, is the effective Hamiltonian for two particles in the medium. Consequently, in order to solve for *in-medium* bound states, one should find the eigenvalues E_b and eigenstates $|\psi_b\rangle$ of

$$H\,|\psi_b\rangle = (h_1 + h_2 + V)\,|\psi_b\rangle = E_b\,|\psi_b\rangle\ . \tag{3.9}$$

Following Eq. (3.5), the spectral contribution of this bound state to the g matrix near E_b is given by

$$g(\omega) \simeq \frac{VQ\,|\psi_b\rangle\,\langle\psi_b|\,QV}{\omega - E_b}\ , \tag{3.10}$$

which evidences the singular behaviour of the g matrix near an eigenvalue of H.

One way to find these eigenvalues can be obtained from the formal solution of equation (3.4)

$$g(\omega) = [1 - \lambda(\omega)V]^{-1}V \ , \tag{3.11}$$

where it is assumed that the inverse of $(1 - \lambda V)$ exists. As the inverse of a matrix is proportional to the inverse of its determinant, when $\det(1 - \lambda V) \to 0$, the g matrix becomes singular. Therefore the criterion used to determine the eigenvalues is

$$\det[1 - \lambda(E_b)V] = 0 \ . \tag{3.12}$$

Moreover, the eigenstates can be found. Near the real axis one has

$$g(E_b + i\eta) \simeq \frac{VQ\left|\psi_b\right\rangle\left\langle\psi_b\right|QV}{i\eta} \ , \tag{3.13}$$

taking the limit $\eta \to 0$ we obtain

$$\lim_{\eta\to 0} i\eta g(E_b + i\eta) = VQ\left|\psi_b\right\rangle\left\langle\psi_b\right|QV \ . \tag{3.14}$$

On the other hand, from equation (3.9) in momentum space, the wave function can be inferred for a total momentum of the pair K and a relative momentum k as

$$Q\psi_{b,\mathbf{K}}(\mathbf{k}) = \frac{\left\langle\mathbf{k}\right| VQ\left|\psi_b\right\rangle}{E_b - e(\mathbf{k}_+) - e(\mathbf{k}_-)} \ , \tag{3.15}$$

where the numerator can be obtained from the diagonal matrix elements of Eq. (3.14).

Finally, the coordinate-space representation is given by a Fourier transform, which for a bound state with orbital momentum L reads

$$\Psi_{b,\mathbf{K}}(r) = \sqrt{\frac{2}{\pi}} \int_{\bar{q}}^{\infty} \psi_{b,\mathbf{K}}(k) j_L(kr) k^2 dk \ . \tag{3.16}$$

In this equation, $\bar{q}$ is the lowest value of momentum allowed by the Pauli blocking.

In practice, for stability in self-consistent calculations of the self-energy at low-densities, the occurrence of singularities in the g matrix is controlled by making [10]

$$g(\omega) \to g(\omega) \frac{\omega - E_b}{(\omega - E_b)^2 + \varepsilon^2} \ . \tag{3.17}$$

In actual calculations $\varepsilon \simeq 1$ keV is used. Some of the results obtained with this theoretical framework will be given in the following subsections.

3.1.1 Binding energies

The *in-medium* bound state energies (if any) are obtained from Eq. (3.12). The di-nucleon binding energy is defined as [10]

$$b_{nn} = E_b - E_{\rm th} \ ,$$

where $E_{\rm th}$ is the p-p energy at the Fermi surface given by $E_{\rm th} = e(\mathbf{k}_+) + e(\mathbf{k}_-)|_{k=k_F}$.

Fig. 3.1 shows the magnitude of the binding energies of di-neutrons in the ${}^1S_0$ channel in neutronic matter (nM), while Fig. 3.2 illustrates these energies in symmetric nuclear matter (SNM) for the ${}^1S_0$ and ${}^3SD_1$ channels. The results are presented relative to the magnitude of the vacuum deuteron energy $E_D = 2.224$ MeV. Zero values of the plot signal the nonexistence of di-nucleons.

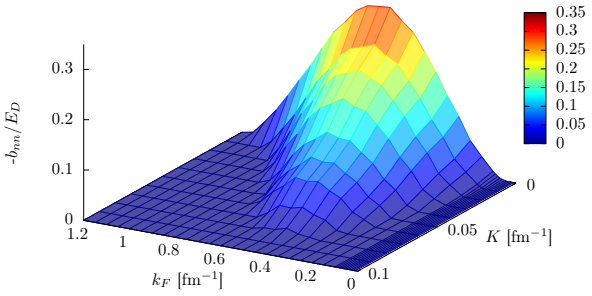

Figure 3.1: ${}^1S_0$ di-neutron binding energies in neutron matter, relative to the deuteron energy in vacuum, as a function of the Fermi momentum k_F and the pair momentum K. The interaction is AV18.

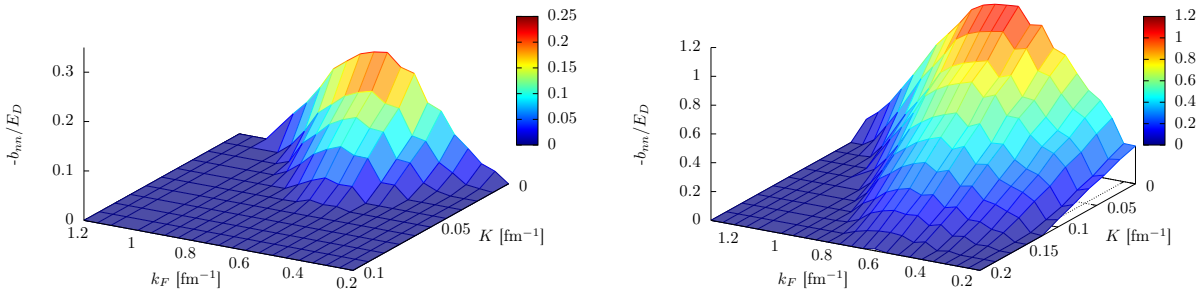

(a) ${}^1S_0$ **(b)** ${}^3SD_1$

Figure 3.2: Di-nucleon binding energies in isospin-symmetric nuclear matter for (a) ${}^1S_0$ and (b) ${}^3SD_1$ channels, relative to the deuteron energy in vacuum, as a function of the Fermi momentum k_F and the pair momentum K. The interaction is AV18.

In general, it can be observed that the binding becomes weaker as the momentum of the pair K increases. In fact, no di-nucleons are found above a certain value of K. Conversely, in all cases, as function of k_F, the binding energies describe a maximum absolute value at nearly $k_F \simeq 0.6$ fm^{-1}. Particularly, for the $K = 0$ case, in neutron matter this maximum binding is about 35% the vacuum deuteron energy, meanwhile in symmetric nuclear matter, the maximum value is 0.25 and 1.2 times the vacuum deuteron energy for the $^1S_0$ and $^3SD_1$ channels, respectively. It is worth mentioning that the *in-medium* deuteron is more bound than in vacuum, for some range of densities.

3.1.2 Eigenfunctions and spatial characterization

Wavefunctions $\Psi(r)$ in coordinate space are obtained from Eq. (3.16). The radial probabilities $r^2|\Psi(r)|$ for pairs without translational motion are shown in Fig. 3.3 for neutron matter and symmetrical nuclear matter. For S waves, one can see that the probability densities describe an oscillatory behaviour which extends to high distances, with a spatial period around ~ 5 fm. The $^3D_1$ also behaves in this way, though not seen properly in Fig. 3.3 since the radial probability is considerably smaller than the S waves probabilities.

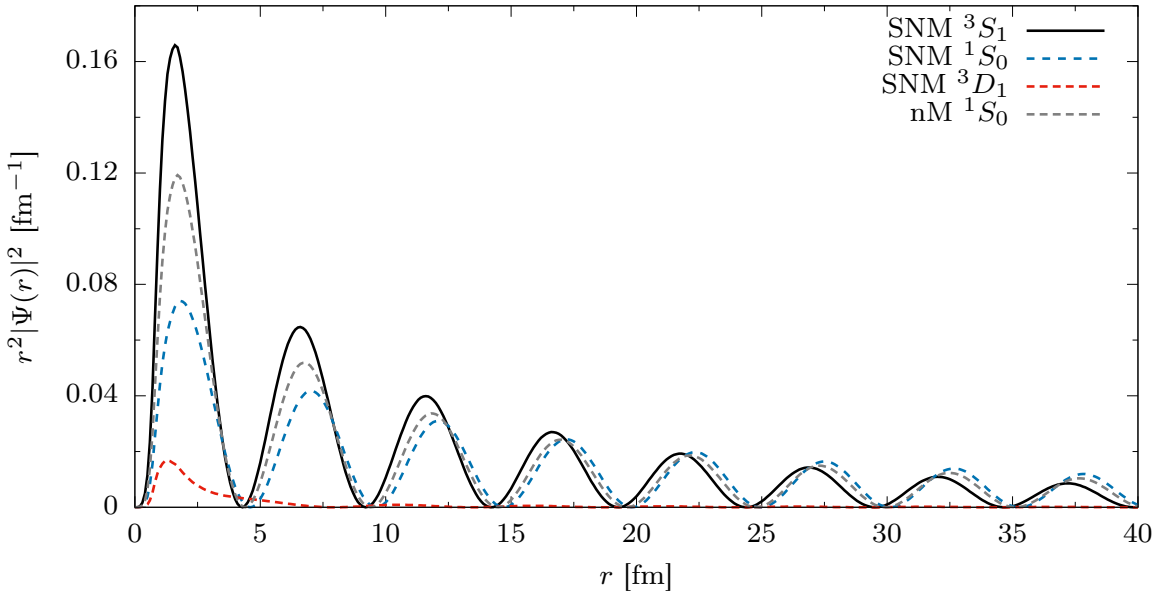

Figure 3.3: Radial probability densities for in-medium di-nucleon solutions in neutron and symmetric nuclear matter, as functions of the relative distance r. The interaction is AV18.

To characterize the spatial extension of the radial probabilities, the mean and mean squared radius can be found ($\langle r \rangle$ and $\langle r^2 \rangle$, respectively). Due to the slowly decrease of the oscillatory behaviour in the functions, a straightforward integration is not reliable to obtain these quantities. Therefore, the Laplace transform of the function is considered [10]

$$F(s) = \int_0^\infty e^{-sr} r^2 |\Psi(r)|^2 dr \ .$$

In this way, for small values of s one has $F(s) \simeq F(0)\,(1 - \langle r \rangle\, s + \langle r^2 \rangle\, s^2/2 - \ldots)$ and $\langle r \rangle$, $\langle r^2 \rangle$ are obtaind by a linear fit of the function

$$f(s) = \frac{1}{s}\left(1 - \frac{F(s)}{F(0)}\right) = \langle r \rangle - \frac{\langle r^2 \rangle}{2} s + \ldots \ .$$

The mean and root-mean-squared radii obtained with this technique are shown in Fig. 3.4 for neutron and symmetric nuclear matter, for $K = 0$ fm^{-1}. They are given in units of the mean internucleon separation $L = \rho^{-1/3}$ for a given density ρ. As it can be seen, except for the $^3D_1$ channel in SNM at low densities, these quantities are greater than L. For some densities, they reach values greater than $10^2 L$. These long-range correlated wave functions are similar to the ones obtained in superfluid nuclear matter within Bardeen-Cooper-Schrieffer (BCS) theory [54].

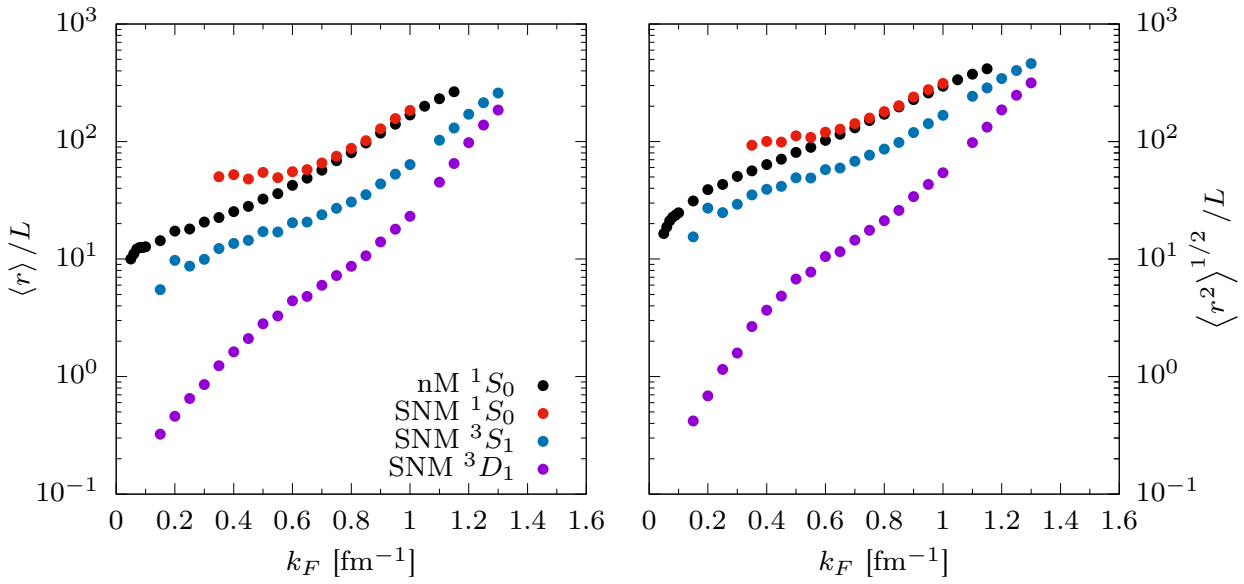

Figure 3.4: Mean radii, relative to the inter-nucleon distance, for *in-medium* bound states in neutron and symmetrical nuclear matter as function of k_F. The interaction is AV18.

3.2 Quest for di-nucleons within SCGF

The search for bound states within SCGF theory can be pursued in analogous way to that applied in the BHF approximation. Starting from the equation for the *in-medium* T-matrix

$$T = V + TG_2^0V \ , \tag{3.18}$$

one can introduce the operator G_{II} related to G_2 by

$$iG_2(12, 1'2') = G_{II}(12, 1'2') - G_{II}(12, 2'1') \ , \tag{3.19}$$

which satisfies

$$G_{II} = G_2^0 + G_2^0VG_{II} = (G_2^0(\omega)^{-1} - V)^{-1} \ . \tag{3.20}$$

In this way we obtain $VG_{II} = TG_2^0$, leading to

$$T = V + VG_{II}V \ . \tag{3.21}$$

On the other hand, the eigenvalue problem in equation (3.9) can be recast as

$$G_{II}(E_b)^{-1} \left|\psi_b\right\rangle = 0 \ . \tag{3.22}$$

Taking inspiration from this, the eigenvalue problem of the two *in-medium* particles is generalized with Eq. (3.22). In fact, this is sustained by the spectral decomposition of the two-time two-particle propagator [34]

$$\begin{aligned} -iG_2(\mathbf{r}_1\mathbf{r}_2, \mathbf{r}_{1'}\mathbf{r}_{2'}; \omega) = &\sum_n \frac{\left\langle \Phi_0^N \right| \hat{\psi}(\mathbf{r}_1)\hat{\psi}(\mathbf{r}_2) \left|\Phi_n^{N+2}\right\rangle \left\langle \Phi_n^{N+2}\right| \hat{\psi}^\dagger(\mathbf{r}_{1'})\hat{\psi}^\dagger(\mathbf{r}_{2'}) \left|\Phi_0^N\right\rangle}{\omega - (E_n^{N+2} - E_0^N) + i\eta} \\ &- \sum_n \frac{\left\langle \Phi_0^N \right| \hat{\psi}^\dagger(\mathbf{r}_{1'})\hat{\psi}^\dagger(\mathbf{r}_{2'}) \left|\Phi_n^{N-2}\right\rangle \left\langle \Phi_n^{N-2}\right| \hat{\psi}(\mathbf{r}_1)\hat{\psi}(\mathbf{r}_2) \left|\Phi_0^N\right\rangle}{\omega - (E_0^N - E_n^{N-2}) - i\eta} \ . \end{aligned} \tag{3.23}$$

Consequently, a possible bound state appears as a discrete simple pole in equation (3.23), which translates to a zero in $G_2(E_b)^{-1}$. Moreover, G_2 is proportional to the antisymmetrized G_{II}, so the pole would also be present in G_{II}. Therefore the T-matrix is singular for an energy equal to E_b and the (possible) eigenvalue can be found as that which satisfies

$$\det[1 - G_2^0(E_b)V] = 0 \ . \tag{3.24}$$

However, as seen from the imaginary part of G_2^0 (Eq. 2.96) as a function of energy, this quantity never vanishes. Consequently, one does not expect *in-medium* bound states with real eigenenergies. In contrast, within BHF, this is possible because the imaginary part of

the propagator involved in the g matrix is zero for energies below $2\varepsilon_F$, leaving room for real eigenvalues in this range.

A way to obtain *in-medium* bound states within SCGF theory is by including a gap in the spectrum, as in superfluid nuclear matter. This causes a discontinuity at k_F leading to two Fermi energies, ε_F^- and ε_F^+, for k_F^- and k_F^+, respectively. In this way, the equations are modified, and the imaginary part of G_2^0 vanishes for energies between $2\varepsilon_F^-$ and $2\varepsilon_F^+$ [36, 96]. With these considerations, *in-medium* bound state eigenenergies are not forbidden in this range. A self-consistent treatment of superfluid nuclear matter is beyond the scope of this work.

It is worth mentioning that complex energy solutions can be obtained for Eq. (3.24). This can be achieved by extending G_2^0 to complex energies. Particulary, complex conjugate eigenvalues have been found using mean-field approximations and quasi-particle spectral functions [78, 79]. In this case, these complex energies are used to obtain an accurate estimate of the pairing gap in the superfluid state.

Chapter 4

Neutron matter within SCGF theory

In this chapter, we present the results for infinite neutron matter within SCGF theory in the ladder approximation. Particular attention is paid to the calculation of spectral functions including the imaginary part of the self-energy. Numerical strategies are explained together with numerical approximations. Results within SCGF theory are compared with those in the BHF approximation.

4.1 Iterative scheme

In Tab. 4.1 we summarize the main equations we make use within the SCGF scheme. To initialize the self-consistent calculations we need to specify a desired density ρ and bare NN interaction, both fixed during the whole calculation. Every calculation starts with an initial self-energy $\Sigma(k,\omega)$, which is guessed or loaded from a previous iteration. The initial $\Sigma(k,\omega)$ allows to calculate the spectral functions $A(\mathbf{k},\omega)$, as indicated in the first step in Tab. 4.1. Since the spectral functions are sharp near the quasi-particle energy, the calculation of the quasi-particle spectrum $e(k)$ is crucial to accurately evaluate integrals involving $A(k,\omega)$. This is why we evaluate $e(k)$ in the second step of our iterative scheme. The third step consists of finding the Fermi energy ε_F by solving

$$\rho = \nu \int \frac{d\mathbf{k}}{(2\pi)^3} n(\mathbf{k}) = \nu \int \frac{d\mathbf{k}}{(2\pi)^3} \int_{-\infty}^{e_F} d\omega \, A(\mathbf{k},\omega) \, , \tag{4.1}$$

where ρ is already specified. The fourth step is to compute the imaginary part of the two-particle Green's function by making use of Eq. (2.96). This imaginary part is then used in the fifth step, making use of the dispersion relation [Eq. (2.97)] to get the real part of G_2^0.

Step	Equation	Reference
1	$A(\mathbf{k},\omega) = -\dfrac{\mathrm{sign}(\omega-\varepsilon_F)}{\pi}\dfrac{\mathrm{Im}\ \Sigma(\mathbf{k},\omega)}{\left(\omega-\frac{k^2}{2m}-\mathrm{Re}\ \Sigma(\mathbf{k},\omega)\right)^2+\left(\mathrm{Im}\ \Sigma(\mathbf{k},\omega)\right)^2}$	(2.64)
2	$e(k) = \dfrac{k^2}{2m} + \mathrm{Re}\ \Sigma(k, e(k))$	(2.119)
3	$\rho = \nu \int \dfrac{d\mathbf{k}}{(2\pi)^3}\int_{-\infty}^{e_F} d\omega\ A(\mathbf{k},\omega)$	(4.1)
4	$\mathrm{Im}G_2^0(\mathbf{K},\mathbf{k},\omega) = -\theta(\omega-2\varepsilon_F)\pi\int_{\varepsilon_F}^{\omega-\varepsilon_F} A(\mathbf{k}_+,E)A(\mathbf{k}_-,\omega-E)dE$ $-\theta(2\varepsilon_F-\omega)\pi\int_{\omega-\varepsilon_F}^{\varepsilon_F} A(\mathbf{k}_+,E)A(\mathbf{k}_-,\omega-E)dE$	(2.96)
5	$\mathrm{Re}G_2^0(\mathbf{K},\mathbf{k},\omega) = \dfrac{1}{\pi}\mathcal{P}\int_{-\infty}^{2\varepsilon_F}\dfrac{\mathrm{Im}G_2^0(\mathbf{K},\mathbf{k},E)}{\omega-E}dE - \dfrac{1}{\pi}\mathcal{P}\int_{2\varepsilon_F}^{\infty}\dfrac{\mathrm{Im}G_2^0(\mathbf{K},\mathbf{k},E)}{\omega-E}dE$	(2.97)
6	$\bar{G_2^0}(K,k,\omega) = \dfrac{1}{2}\int_{-1}^{1} d(\cos\theta)G_2^0(\mathbf{K},\mathbf{k},\omega)$	(4.6)
7	$\langle\mathbf{k}\,|\,T(\mathbf{K},\omega)\,|\,\mathbf{k}'\rangle = \langle\mathbf{k}\,|\,V\,|\,\mathbf{k}'\rangle + \int d\mathbf{p}\,\langle\mathbf{k}\,|\,V\,|\,\mathbf{p}\rangle\,\bar{G_2^0}(K,p,\omega)\,\langle\mathbf{p}\,|\,T(\mathbf{K},\omega)\,|\,\mathbf{k}\rangle$	(2.90)
8	$\mathrm{Im}\Sigma(\mathbf{k},\omega) =$ $\theta(\omega-\varepsilon_F)\int_{2\varepsilon_F-\omega}^{\varepsilon_F} dE''\int\frac{d\mathbf{k}'}{(2\pi)^3}\left\langle\frac{\mathbf{k}-\mathbf{k}'}{2}\right\vert\mathrm{Im}T_{\mathbf{k}+\mathbf{k}'}(\omega+E'')\left\vert\frac{\mathbf{k}-\mathbf{k}'}{2}\right\rangle_A A(\mathbf{k}',E'')$ $-\theta(\varepsilon_F-\omega)\int_{\varepsilon_F}^{2\varepsilon_F-\omega} dE''\int\frac{d\mathbf{k}'}{(2\pi)^3}\left\langle\frac{\mathbf{k}-\mathbf{k}'}{2}\right\vert\mathrm{Im}T_{\mathbf{k}+\mathbf{k}'}(\omega+E'')\left\vert\frac{\mathbf{k}-\mathbf{k}'}{2}\right\rangle_A A(\mathbf{k}',E'')$	(2.115)
9	$\Sigma_{HF}(\mathbf{k}) = \int\dfrac{d\mathbf{k}'}{(2\pi)^3}\left\langle\dfrac{\mathbf{k}-\mathbf{k}'}{2}\right\vert V\left\vert\dfrac{\mathbf{k}-\mathbf{k}'}{2}\right\rangle_A\int_{-\infty}^{\varepsilon_F} A(\mathbf{k}',E)dE$	(2.107)
10	$\mathrm{Re}\Sigma(\omega) = \Sigma_{HF} + \dfrac{1}{\pi}\mathcal{P}\int_{-\infty}^{\varepsilon_F}\dfrac{\mathrm{Im}\ \Sigma(E)}{\omega-E}dE - \dfrac{1}{\pi}\mathcal{P}\int_{\varepsilon_F}^{\infty}\dfrac{\mathrm{Im}\ \Sigma(E)}{\omega-E}dE$	(2.117)

Table 4.1: Iterative scheme employed to solve the SCGF theory equations.

The sixth step consists in calculating an angle-averaged propagator $\bar{G}_2^0$ (this will be clarified later). In the seventh step, we use this angle-averaged propagator and the bare NN potential $V(k,k')$ to solve for the *in-medium* T matrix, $T(K,\omega)$, for various energies ω and momenta of the pair K, by means of Eq. (2.90). In the eighth step, this effective interaction is evaluated in all the points needed to calculate the integrals in Eq. (2.115) to obtain the imaginary part of the self-energy. In the ninth step, the imaginary part of the self-energy is used in the dispersion relations of Eq. (2.117) to obtain the energy dependent contribution to Re $\Sigma(k,\omega)$. The tenth step consists in calculating the Hartree-Fock or static contribution $\Sigma_{HF}(k)$ using the spectral function $A(k,\omega)$ and the bare NN potential, by means of Eq. (2.107). With all the steps described above, a new self-energy is obtained, which can be loaded again in the iterative procedure. The scheme is repeated several times until self-consistency is achieved.

For a global view on how the quantities involved in the calculation are interrelated, in Fig. 4.1 we show a flowchart illustrating their interdependence. An arrow from one frame to another indicates that the quantity inside the first frame is required for the calculation of the quantity encapsulated in the second one. Both ρ and V are the external inputs of the program.

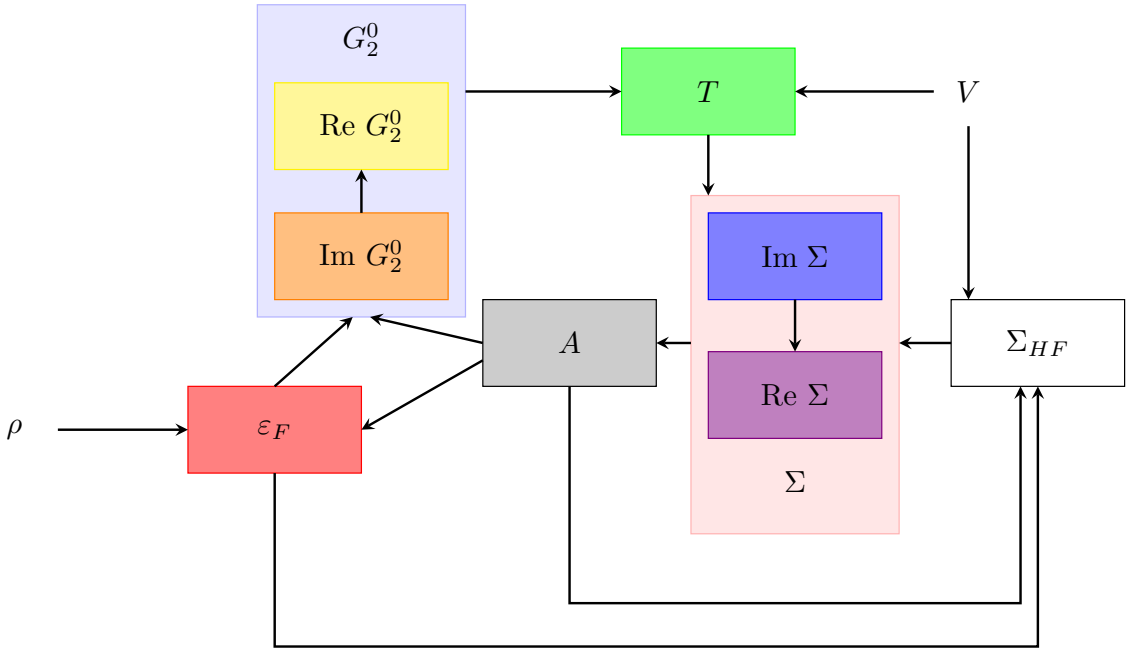

Figure 4.1: Graphical representation of the interrelation between the quantities involved in the SCGF iterative scheme.

A substantial part of this work has been devoted to the development of computational programs that implement the iterative scheme described above. Numerical techniques and details can be found in Refs. [44, 51, 53].

4.2 Numerical implementation

The iterative procedure described has been implemented numerically within the use of FORTRAN language, together with UNIX scripts. These programs are based on general numerical considerations, such as the discretization of all the continuous integrals. Additionally, numerical cuttoffs have been tested to ensure convergence of some of the infinite integrals appearing in the scheme.

A crucial approximation was needed for the treatment of the sharpness of the spectral function around the Fermi surface. As one can see from Eq. (2.64), the spectral function is nearly a Lorentzian distribution centered at the quasi-particle energy $e(\mathbf{k})$. Additionally, from Eq. (2.43), the spectral function must be positive for all energies and momenta. Consequently, $\mathrm{Im}\Sigma(\mathbf{k},\omega) \geq 0$, for $\omega < e_F$, and $\mathrm{Im}\Sigma(\mathbf{k},\omega) \leq 0$, for $\omega > e_F$. Assuming that the imaginary part of the self-energy is a smooth continuous function, then it should have a zero at $\omega = e_F$. Then, the spectral function tends to a delta function near the Fermi surface, feature difficult to handle numerically. Different strategies have been proposed to address this issue [32, 60, 77]. In this work, we decompose the spectral function in a quasi-particle narrow peak superposed to a soft background function [29], namely

$$A(\mathbf{k},\omega) = Z(\mathbf{k})\delta[\omega - e(\mathbf{k})] + B(\mathbf{k},\omega) \ , \tag{4.2}$$

with

$$B(\mathbf{k},\omega) = -\frac{\mathrm{sign}(\omega - e_F)}{\pi}\frac{\mathrm{Im}\Sigma(\mathbf{k},\omega)}{\lambda(\mathbf{k},\omega)} \ . \tag{4.3}$$

Here

$$\lambda(\mathbf{k},\omega) = \max\left\{\left[\omega - \frac{k^2}{2m} - \mathrm{Re}\ \Sigma(\mathbf{k},\omega)\right]^2 + \left[\mathrm{Im}\ \Sigma(\mathbf{k},\omega)\right]^2, \lambda_0\right\} \ . \tag{4.4}$$

The λ_0 parameter has been arbitrarily set to 16 MeV^2. The strength of the quasi-particle peak $Z(\mathbf{k})$, is then adjusted to fulfill the sum rule for the spectral function [Eq. (2.48)]. In this way the quasi-particle delta function contribution can be handled analytically (see Annex), with the background contribution handled numerically.

On the other hand, to calculate the *in-medium* T matrix, as well as the Hartree-Fock contribution to the self energy, the anti-symmetrized diagonal matrix elements are needed. These are obtained making use of partial wave decompositions. For the bare potential, for example,

$$\langle \mathbf{k}|V|\mathbf{k}\rangle_A = \sum_\alpha n_\alpha \langle \mathbf{k}|V^\alpha|\mathbf{k}\rangle \ , \tag{4.5}$$

where α denotes spin, isospin and angular momentum states. n_α is a factor containing

degeneracy and geometrical factors. More details on this partial wave decomposition can be found in references [44] and [53]. A finite number of partial waves are considered to terminate the sums. In this work, waves up to $J = 9$ are considered in the Hartree-Fock's contribution to the self-energy. For the energy dependent part we consider waves up to $J = 2$.

The *in-medium* T matrix must be calculated for each channel α needed for the partial wave decomposition. This would be done by expanding the Lippmann-Schwinger-type equation [Eq. (2.90)], however, the exact two-particle Green's function G_2^0 depends explicitly on the angle between the center of mass momentum and the relative momentum. This leads to the coupling of partial waves with different total angular momentum J [81], which means that the total angular momentum of two nucleons in the medium is not conserved. To bypass this difficulty, an angle-averaged propagator is introduced as

$$\bar{G_2^0}(K, k, \omega) = \frac{1}{2} \int_{-1}^{1} d(\cos\theta) G_2^0(\mathbf{K}, \mathbf{k}, \omega) \ . \tag{4.6}$$

In this way, the equation can be written as a one-dimensional integral equation for each partial wave, namely

$$\langle q| \, T_{LL'}^{JST}(K, \omega) \, |q'\rangle = \langle q| \, V_{LL'}^{JST} \, |q'\rangle + \frac{2}{\pi} \sum_{\ell} \int_0^{\infty} p^2 dp \, \langle q| \, V_{L\ell}^{JST} \, |p\rangle \, \bar{G_2^0}(K, p, \omega) \, \langle p| \, T_{\ell L'}^{JST}(K, \omega) \, |q'\rangle \ , \tag{4.7}$$

where the summation over ℓ takes place only for coupled partial waves. Some efforts have been made to include the angular dependence of the two-body Green's function into the effective interaction, mostly in BHF calculations [9, 81, 93]. Small deviations from the angle-averaged approach were found.

Eq. (4.7) for the T matrix is discretized in the relative momentum variable p. A pole substraction in required for the quasi-particle contribution to the propagator, coming from the decomposition of the spectral function [Eq. (4.2)]. The resulting matrix is solved by means of standard inversion procedures [10, 44, 51, 53]

With all the considerations described above, stable self-consistent results are obtained. About 6 to 13 iterations are needed to reach a numerical convergence of less or equal than 0.05%. The number of iterations depends on the initial loaded self-energy. In this work, the first run was carried out with an initial guess constructed with a set of gaussian functions [77]. Afterwards, the converged self-energy was used as the starting point for other densities. During the calculation, the real and imaginary parts of the on-shell self-energy at zero relative momentum, together with the Fermi energy are monitored after each iteration to assess whether numerical convergence is achieved.

4.3 Neutron matter results

In this section, we focus on results for neutron matter. We pay attention to relevant microscopic properties of the system and compare with similar results obtained by other studies [24, 73, 76, 86]. The calculations were done using the Argonne V18 potential.

4.3.1 Self-energy

In Fig. 4.2, we show surface plots for the real and imaginary parts of the self-energy $\Sigma(k,\omega)$ for neutron matter at density ρ =0.08 fm^{-3}. The resulting Fermi energy is $\varepsilon_F = 12.77$ MeV and the corresponding Fermi momentum is $k_F = 1.34$ fm^{-1}. We observe that near the Fermi energy and low momenta, the imaginary part of Σ has a maximum below ε_F, and a smaller minimum above ε_F. This wavy structure near ε_F stems from the structure of Im Σ in Eq. (2.115), specifically from the shape of the spectral function and Im T, as studied in Ref. [44].

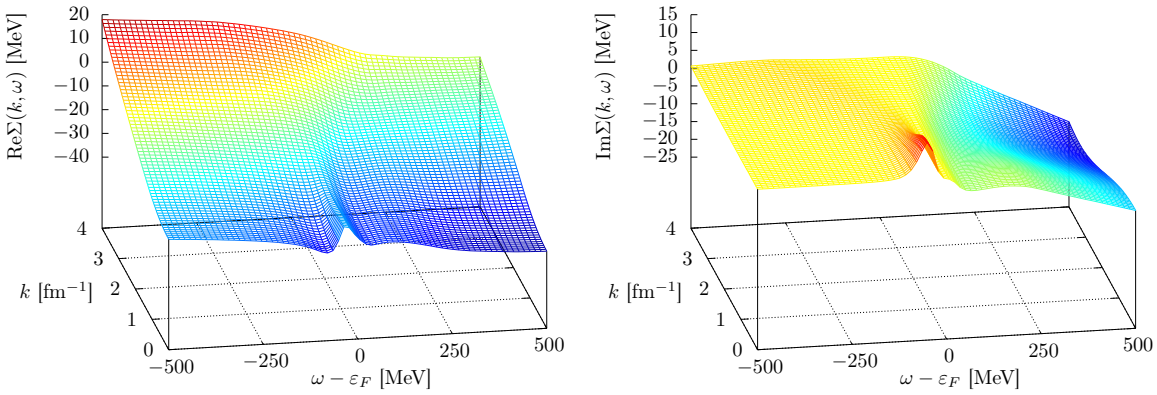

(a) Real part of $\Sigma(k,\omega)$. **(b)** Imaginary part of $\Sigma(k,\omega)$.

Figure 4.2: Energy and momentum dependence of the self-energy in neutron matter at density $\rho = 0.08$ fm^{-3}.

The behaviour of the peaks and minima of the self-energy at various densities, is shown in Fig. 4.3, as a function of energy and for relative momenta $k = 0$ (a), $k = k_F$ (b) and $k = 2k_F$ (c). We notice that the peak increases its maximum value with increasing density, while the local minimum vanishes as the density increases.

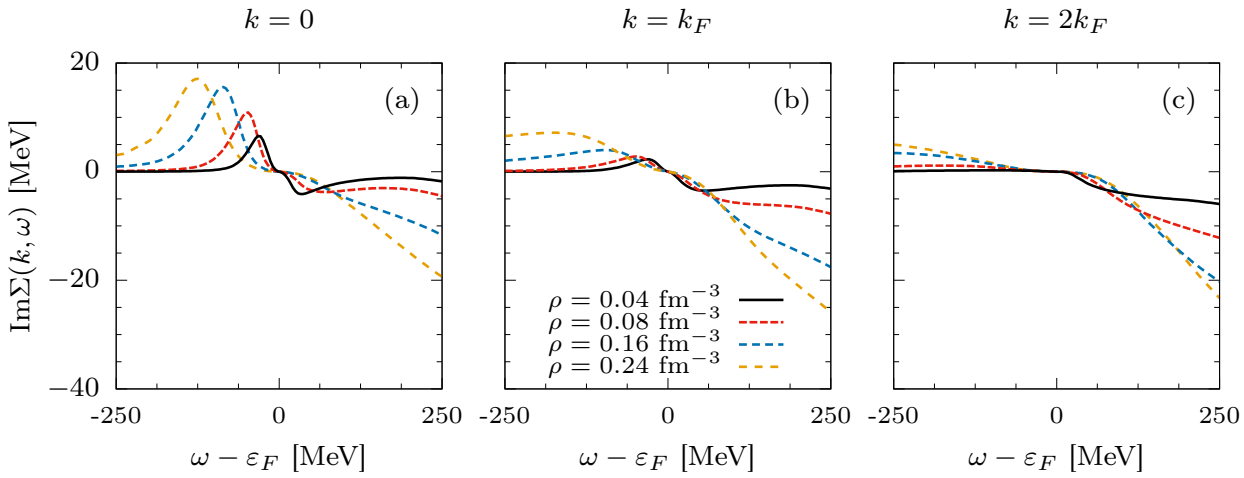

Figure 4.3: Imaginary part of the self-energy in neutron matter for different densities and for relative momenta 0 (a), k_F (b) and $2k_F$ (c).

In Fig. 4.4, we show the tails of the imaginary part of the self-energy as function of the energy $\omega - \varepsilon_F$. Here we consider zero relative momentum at different densities. We observe that both (positive- and negative-energy) tails decrease with decreasing densities. The same trend was observed at higher relative momenta, but the energy structures were more spread.

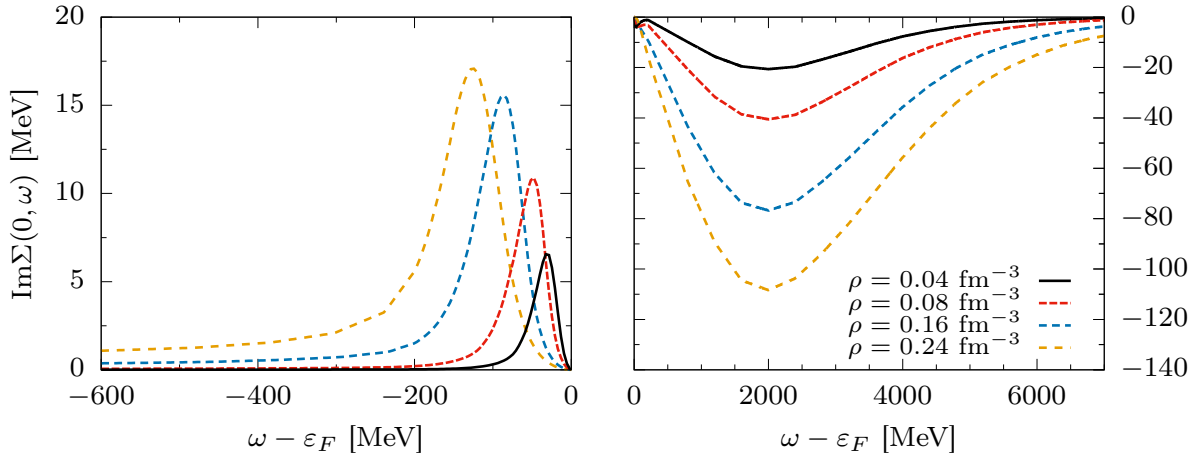

Figure 4.4: Energy tails of the imaginary part of the self-energy in neutron matter for different densities. The relative momentum is $k = 0$.

The real part of the self-energy is calculated making use of the dispersion relation shown in Eq. (2.97), combined with the Hartree-Fock contribution Σ_{HF}. The energy dependence of Re Σ is shown in Fig. 4.5, exhibiting qualitative resemblance to that for Im Σ, due to the dispersion relation. However, it is less pronounced. This resemblance can be understood by the non-dispersive Hartree-Fock contribution, which easily dominates the dispersive part. The momentum dependence is also dominated by this contribution, which is an increasing function with respect to momentum. This implies that Re Σ becomes repulsive at large momenta, as observed in Fig. 4.5.

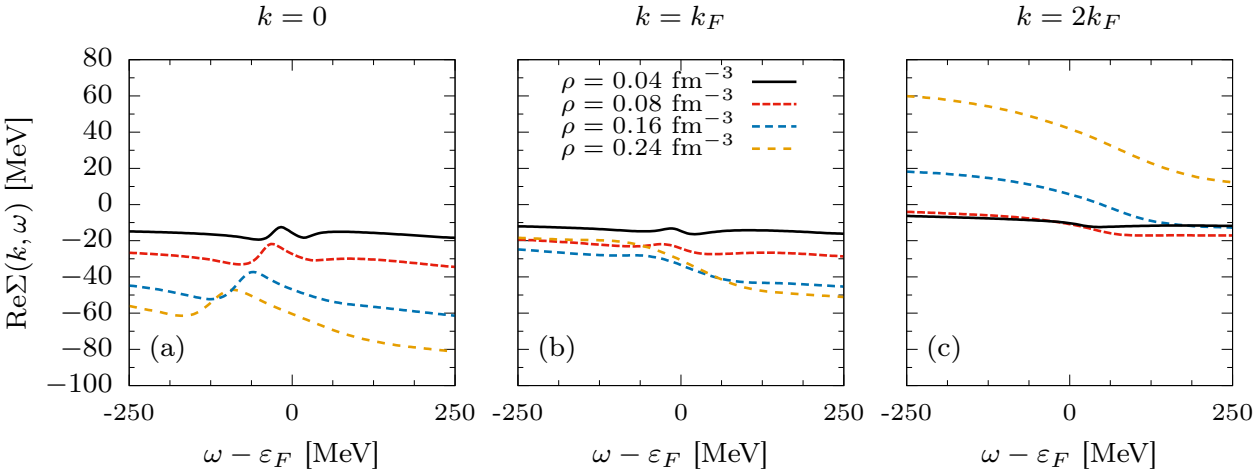

Figure 4.5: Real part of the self-energy in neutron matter for different densities and for relative momenta 0 (a), k_F (b) and $2k_F$ (c).

To compare the results presented above with those within the BHF approximation, we need to calculate the quasi-particle energy and especially, the on-shell self-energy $\Sigma(k, e(k))$. In Fig. 4.6 we plot the sp potential $U(k) = \text{Re}\Sigma(k, e(k))$ at three densities. Results based on the SCGF theory and the BHF approximation are shown with red and black curves, respectively. We observe that the SCGF results are more repulsive at lower momenta than those from BHF. This difference depends on the density. For $\rho = 0.08$ fm^{-3}, the sp potential is about 8 MeV more repulsive in SCGF scheme than in BHF approximation. This difference increases to 15 MeV at $\rho = 0.16$ fm^{-3}, and to $\sim$25 MeV at $\rho = 0.24$ fm^{-3}. Keep in mind that the main differences between BHF and SCGF frameworks are the inclusion of hole-hole propagation, in addition to the self-consistent dressing of the ladders. Effects of repulsive nature have been reported with the inclusion of intermediate hole-hole propagation in a quasi-particle level [5]. The findings reported in this work are in line with those reported in Ref. [76].

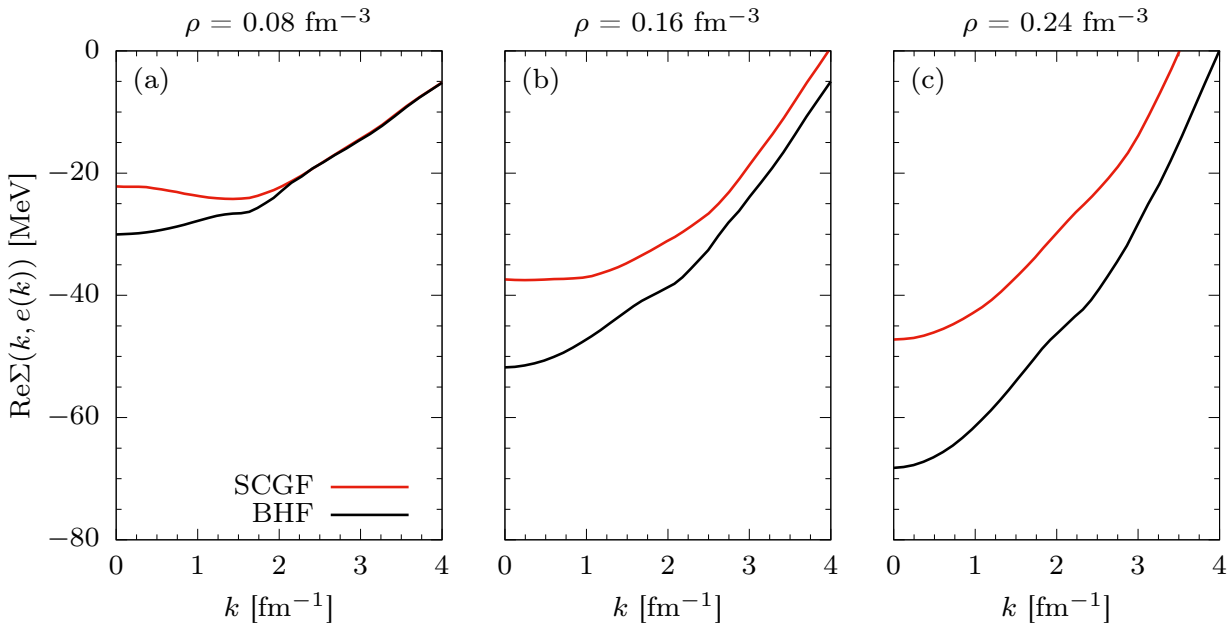

Figure 4.6: Real part of the on-shell self-energy in neutron matter within the SCGF theory (red curves) and the BHF approximation (black curves) for densities $\rho = 0.08$ (a), 0.16 (b) and 0.24 (c) fm^{-3}.

The on-shell imaginary part of the self-energy is related to the energy-width of a particle or hole state of momentum k. Moreover, when the quasi-particle spectral function is introduced into the one-particle propagator, it can be demonstrated that for long times, the time dependent one-particle Green's function behaves as [39]

$$G_{\rm qp}(\mathbf{k}, t) \propto \exp\left[-i\, e(\mathbf{k})t - \Gamma(\mathbf{k})t\right] \ , \tag{4.8}$$

where $\Gamma(k) = |\text{Im}\ \Sigma(\mathbf{k}, e(\mathbf{k}))|$. This represents a state with a defined energy $e(\mathbf{k})$ that decays with a rate given by $\tau(\mathbf{k}) = \Gamma(\mathbf{k})^{-1}$. Consequently, the on-shell imaginary part of the self-energy is also related to the inverse lifetime of a quasi-particle state decay. In Fig. 4.7, the absolute values of Im $\Sigma(k, e(k))$ are shown as function of the relative momentum k, for three different densities. An obvious difference with the BHF scheme is the non-vanishing on-shell width for hole states, because, as it was mentioned before, the BHF framework does not include hole-hole propagation, resulting in a zero imaginary part for $k < k_F$. In general, $|\Sigma(k, e(k))|$ increases with the density for states far from k_F. Near the Fermi momentum the vanishing minimum signals infinite lifetimes of quasi-particle states at the Fermi surface. For particle states, the on-shell SCGF imaginary part of Σ is slightly smaller in absolute value, than the one obtained within BHF. Their differences fluctuate between 3 to 5 MeV.

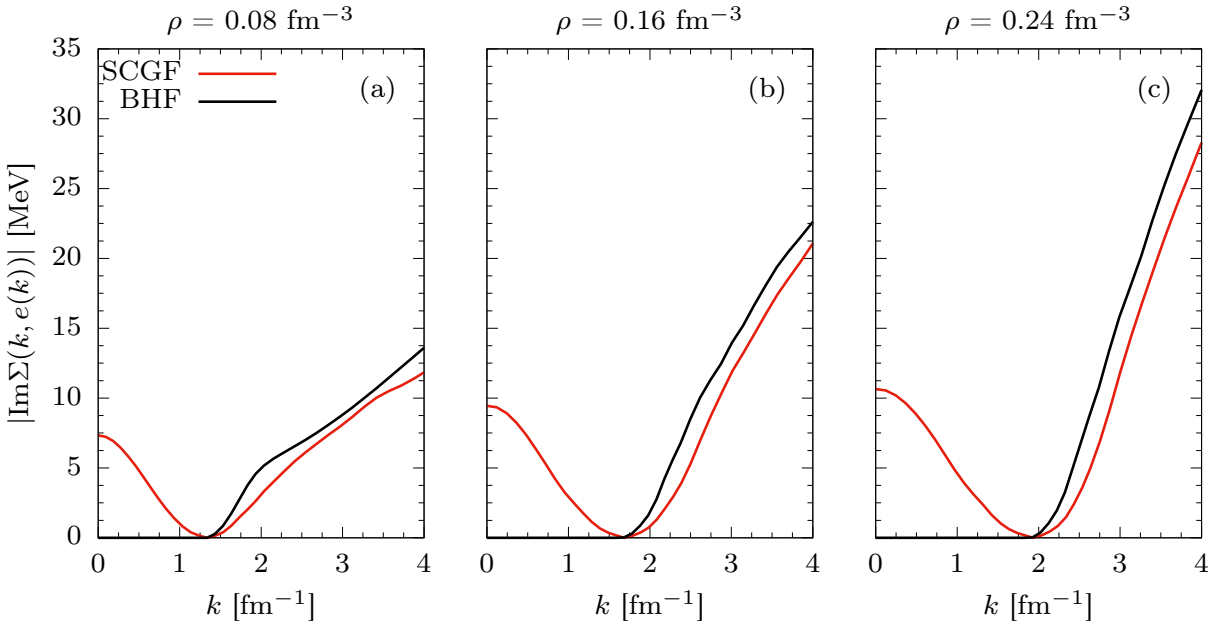

Figure 4.7: Absolute value of the imaginary part of the on-shell self-energy in neutron matter within the SCGF theory (red curves) and the BHF approximation (black curves) at densities $\rho = 0.08$ (a), 0.16 (b) and 0.24 (c) fm^{-3}.

The on-shell self-energy at evenly-spaced densities is presented in Fig. 4.8. The densities are $\rho = 0.02(0.02)0.20$ fm^{-3}. It is worth mentioning that the zero momentum values of the real part increase uniformly with decreasing density. In contrast, the imaginary part, decreases with larger successive differences between consecutive curves. Additionally, both real and imaginary parts, show a small valley, which becomes more pronounced at smaller densities. This valley takes place at momentum slightly above k_F.

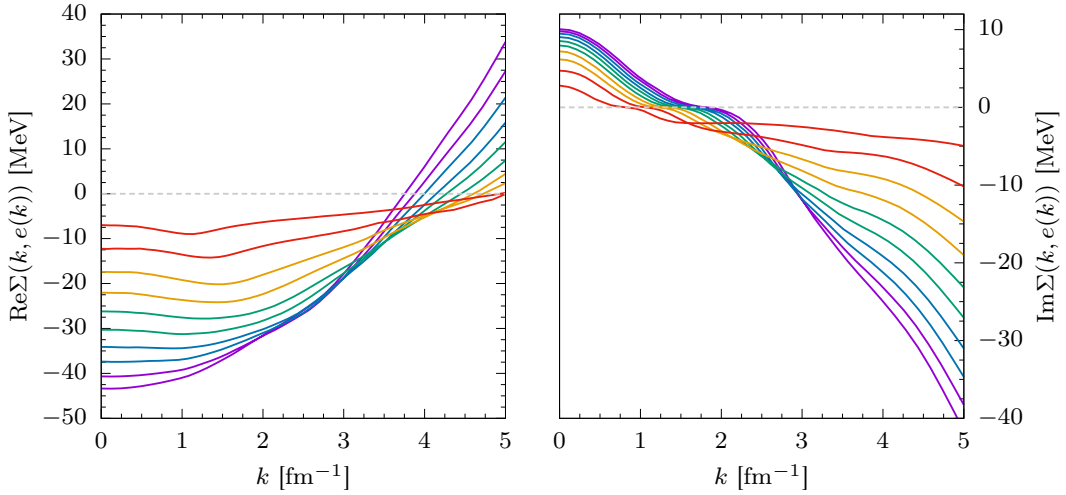

Figure 4.8: On-shell self-energy at various densities. The left(right) frame shows the real(imaginary) part. The outmost purple(red) curves correspond to $\rho = 0.20(0.02)$ fm^{-3}. The density difference between consecutive curves is 0.02 fm^{-3}.

In Tab. 4.2 we summarize the densities, Fermi momenta and Fermi energies corresponding to the curves included in Fig. 4.8.

ρ [fm^{-3}]	k_F [fm^{-1}]	ε_F [MeV]
0.02	0.84	6.36
0.04	1.06	8.81
0.06	1.21	11.22
0.08	1.34	12.77
0.10	1.44	15.78
0.12	1.53	18.41
0.14	1.61	21.64
0.16	1.69	25.81
0.18	1.76	29.86
0.20	1.82	35.14

Table 4.2: Densities ρ, Fermi momenta k_F and Fermi energies ε_F corresponding to the curves included in Fig. 4.8.

4.3.2 Spectral function and momentum distribution

Once the self-energy is determined, the spectral function can be evaluated using Eq. (2.64). These functions give information about the correlations between particles in the system. In Fig. 4.9 we show the spectral function $A(k,\omega)$ as function the energy. We consider different densities and three momenta. In Fig. 4.10 we show the spectral function at $\rho = 0.08$ fm^{-3} in the energy-momentum plane for five momenta.

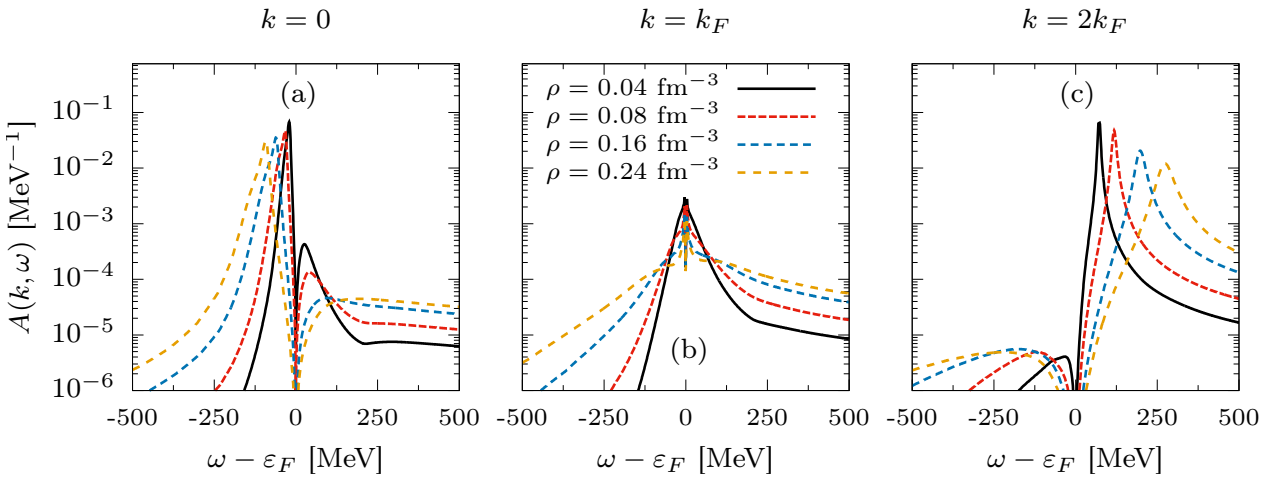

Figure 4.9: Spectral function as a function of energy for different densities and for momenta $k = 0$ (a), k_F (b) and $2k_F$ (c)

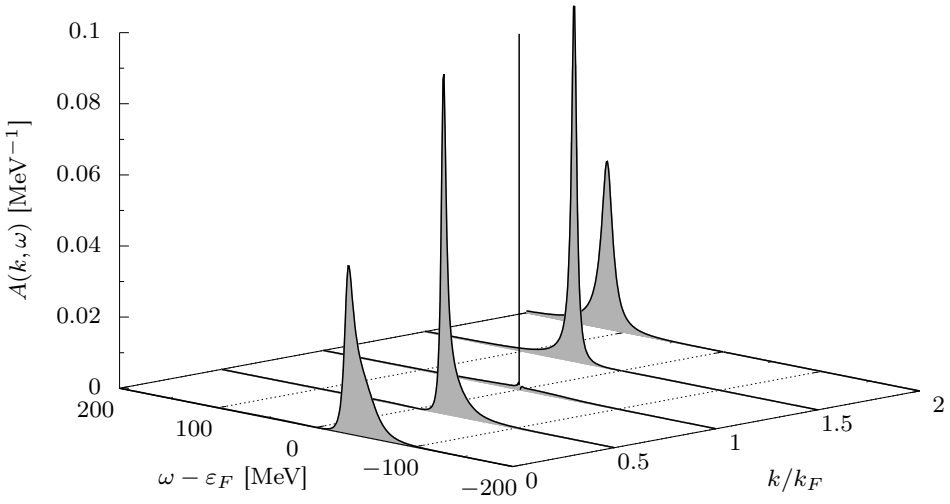

Figure 4.10: Spectral function in the energy-momentum plane for momenta $k = 0$, $k_F/2$, k_F, $3k_F/2$ and $2k_F$. The density is 0.08 fm^{-3}.

In all cases, the global maxima signal the position of the quasi-particle peak, where in our approximation, is given by a delta function. For simplicity, we omit these delta contributions in the plots, but one should keep in mind their presence.

The zero-momentum spectral functions present a quasi-particle peak at $\omega < \varepsilon_F$ (hole states), which is displaced to lower energies as the density increases. This reflects the fact that for higher densities, the particles with lower momenta are more bound. Conversely, for $k=2k_F$, the spectral functions describe a quasi-particle peak at $\omega > \varepsilon_F$ (particle states) that moves to higher energies with increasing density, reflecting repulsiveness at high momenta states in higher density. At the Fermi surface ($k = k_F$) the quasi-particle peak remains fixed at the Fermi energy, for all densities, becoming narrower with decreasing density. The functions also present a dip at ε_F, caused by the vanishing value of Im $\Sigma(k, \varepsilon_F)$. Except for this numerical valley, the functions show larger width at higher densities. This means that the particles are more spread out over energies, that is to say, more correlated.

Another quantity that measures the correlation between particles is the momentum distribution $n(k)$. Once the spectral function is known, one can calculate this function from

$$n(k) = \int_{-\infty}^{\varepsilon_F} A(k,\omega) d\omega \tag{4.9}$$

In Fig. 4.11, the momentum distribution is shown for different densities. For a non-correlated system, this distribution becomes a Heaviside step function, $n(k) = \theta(k_F - k)$. In contrast,

for correlated infinite nuclear matter, the hole states suffer a depletion and higher momentum states get populated. Microscopically, a pair of nucleons can reach high relative momentum when they are at a small relative distances. Thus, the depletion is caused by the short-range repulsive nature of the interaction. Quantitatively, this depletion is nearly constant for low momentum states and is weakly dependent on the density. For the AV18 interaction studied in this work, about 2.5-6 % of the hole states are depleted over a large range of densities. For higher momenta, the occupation diminishes slowly. This can be observed in panel (b) of Fig. 4.11, disclosing the way it diminishes with k/k_F.

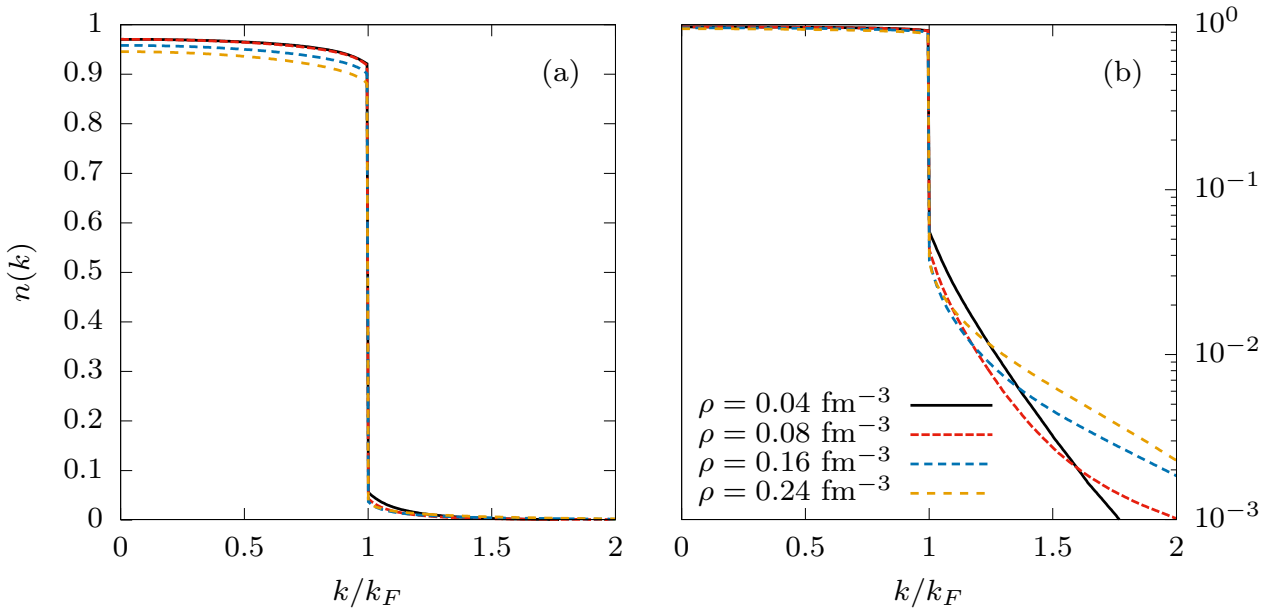

Figure 4.11: Momentum distribution in neutron matter for three different densities $\rho = 0.04$, 0.08, 0.16 and 0.24 fm^{-3}. The distribution is shown on a linear (a) and a logarithmic scale (b).

The momentum distribution also exhibits a discontinuity at the Fermi surface. Making use of the decomposition of the spectral function given by Eq. (4.2), the discontinuity can be expressed as

$$\lim_{\eta \to 0^+} [n(k_F - \eta) - n(k_F + \eta)] = Z(k_F) \, . \tag{4.10}$$

Thus, the discontinuity matches the quasi-particle strength at k_F. We obtain $Z(k_F)$ between 0.84 and 0.86.

In Fig. 4.12 we show the quasi-particle strength $Z(k)$ as a function of the ratio k/k_F. We observe that $Z(k)$ has a maximum at $k = k_F$, directly related to the infinite lifetimes of quasi-particles at the Fermi surface. For lower and higher momenta, the strength vanishes

sharply. We also observe that $Z(k)$ gets wider with decreasing density. This is in agreement with the fact that the imaginary part of the self-energy diminishes in absolute value, at smaller densities. Thus, to fulfill the sum rule the spectral strength gets distributed mostly around the quasi-particle peak.

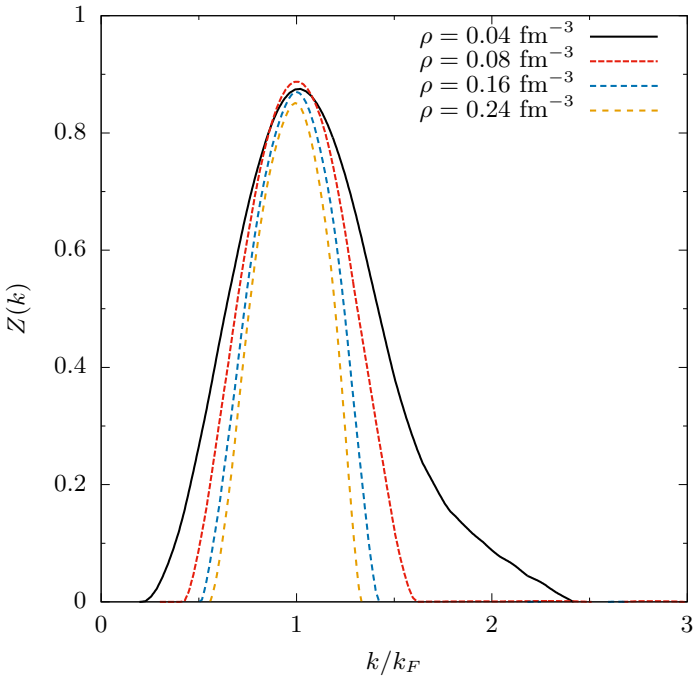

Figure 4.12: Quasi-particle strength as a function of momentum, in neutron matter at various densities.

4.3.3 Energy per nucleon

In order to characterize the energy of the neutron medium as a function of its density, we proceed to calculate the energy per nucleon (E/N) in neutron matter. To do so we use Eqs. (2.133) and (2.133). In Fig. 4.13 we plot E/N as a function of the density. Red and black curves denotes results for SCGF and BHF, respectively. Small differences are observed between both schemes at densities below 0.08 fm^{-3}. This fact reinforces the validity of using the BHF approximation at low densities to obtain properties of low density nuclear matter. At higher densities, however, the SCGF results depart from the BHF ones. As observed, their difference increase at higher densities, with the SCGF energies above the BHF results. This overall trend can be explained by the repulsive effect introduced by h-h propagation, which gets enhanced at higher densities.

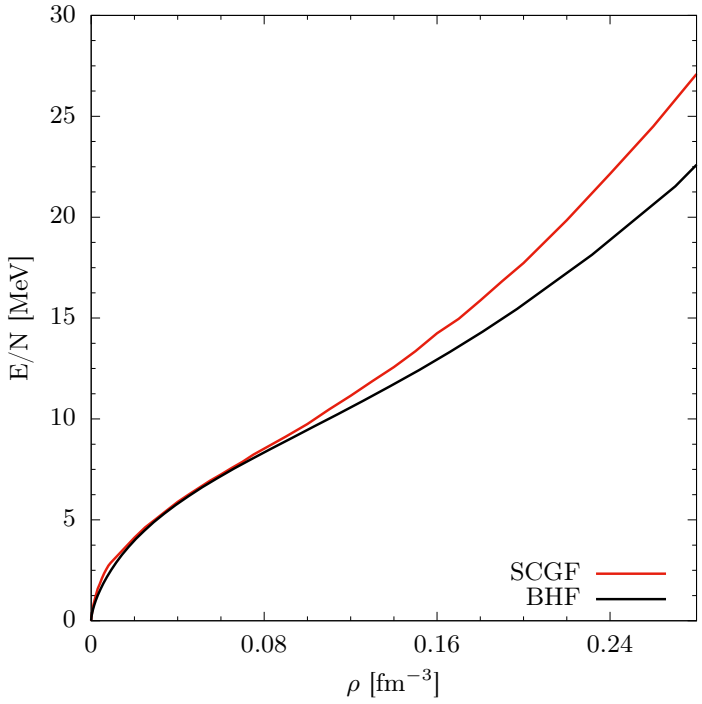

Figure 4.13: Energy per nucleon in neutron matter within the SCGF theory (red curve) and the BHF approximation (black curve), as a function of density.

An interesting feature observed in Fig. 4.13 is steepest behaviour of E/N as a function of ρ. Since the the pressure of the system is given by

$$P = \frac{\partial(E/N)}{\partial\rho} \,, \tag{4.11}$$

its use in the study of hydrostatic equilibrium in neutron stars might allow for more massive stars. On the other hand, astrophysical observations in the last decades have measured neutron stars with masses greater than two solar masses [7, 28, 30]. Thus, it would be interesting to construct an equation of state within SCGF to see whether it is feasible to explain some of these observations. However, the results shown here are conditioned to the bare interaction, which in our case (AV18) reproduces scattering data up to 300 MeV in the laboratory system. Therefore, other NN interactions should be considered. A possible candidate is the inversion potential above pion-production threshold, recently developed by Adriazola *et al.* [4].

4.3.4 Neutron mean-free path in the medium

An interesting transport property of nuclear matter is the *in-medium* mean-free path. This quantity is defined as [75, 87]

$$\lambda(k) = \frac{v(k)}{|\Gamma(k)|} \ . \tag{4.12}$$

Here, $v(k)$ is the group velocity, given by $v(k) = \partial\varepsilon/\partial k$, where $\varepsilon(k)$ is the quasi-particle spectrum, and $\Gamma(k)$ is the quasi-particle inverse lifetime. An extension of the Green's functions techniques to the complex energy plane has been introduced by Rios and Somà [75, 87] where the quasi-particle pole can be extracted from the one-body propagator.

The one-particle propagator can naturally be extended to the complex energy plane as

$$G(\mathbf{k}, z) = \int_{-\infty}^{\varepsilon_F} \frac{A_h(\mathbf{k}, \mathbf{p})}{z - E} dE + \int_{\varepsilon_F}^{\infty} \frac{A_p(\mathbf{k}, \mathbf{p})}{z - E} dE \ , \tag{4.13}$$

being this a unique complex-variable function, analytic off the real axis. The real valued propagator is recovered by evaluating the complex valued function near the real axis, as

$$G(\omega) = \begin{cases} \lim_{\eta \to 0^+} G(\omega + i\eta) & , \omega > \varepsilon_F \\ \lim_{\eta \to 0^+} G(\omega - i\eta) & , \omega < \varepsilon_F \end{cases} \ . \tag{4.14}$$

This propagator also fulfills a Dyson equation, extended to complex energies by

$$G(\mathbf{k}, z) = \frac{1}{z - \frac{k^2}{2m} - \Sigma(\mathbf{k}, z)} \ . \tag{4.15}$$

Thus, the complex-energy self-energy is given by

$$\Sigma(\mathbf{k}, z) = \Sigma_{HF}(\mathbf{k}) + \frac{1}{\pi} \int_{-\infty}^{\varepsilon_F} \frac{\text{Im}\ \Sigma(k, E)}{z - E} dE - \frac{1}{\pi} \int_{\varepsilon_F}^{\infty} \frac{\text{Im}\ \Sigma(k, E)}{z - E} dE \ .$$

What we are actually considering is the analytical continuation of the propagator $\tilde{G}(k, \omega)$, computed from the Dyson equation using the analytical continuation of the self-energy. The last one is given by $\tilde{\Sigma}(k, z) = \Sigma(k, z)$, for $\text{Im}z > 0$, and $\tilde{\Sigma}(k, z) = \Sigma^*(k, z)$, for $\text{Im}z \leq 0$.

The main features of the propagators discussed above are shown in Fig. 4.14. In panels (a) and (c) [(b) and (d)] we plot the real (imaginary) part of $G(0, z)$ and $\tilde{G}(0, z)$, respectively. Although we observe in panel (a) that the real part of G is continuous in the complex energy plane, from panel (b) we notice that the imaginary part is discontinuous across the real axis and thus, non-analytic. The discontinuity is recognized by the abrupt change of color. Conversely, we observe in panels (c) and (d) that both real and imaginary parts of $\tilde{G}$ are

continuous functions across the real axis. but have a pole in the lower-half complex energy plane. By the Dyson equation, the position of the pole of $\tilde{G}(k,z)$ is obtained as

$$z(k) = \frac{k^2}{2m} + \mathrm{Re}\tilde{\Sigma}(\mathbf{k}, z(k)) + \mathrm{Im}\tilde{\Sigma}(\mathbf{k}, z(k))i = \varepsilon(k) + \Gamma(k)i \; . \tag{4.16}$$

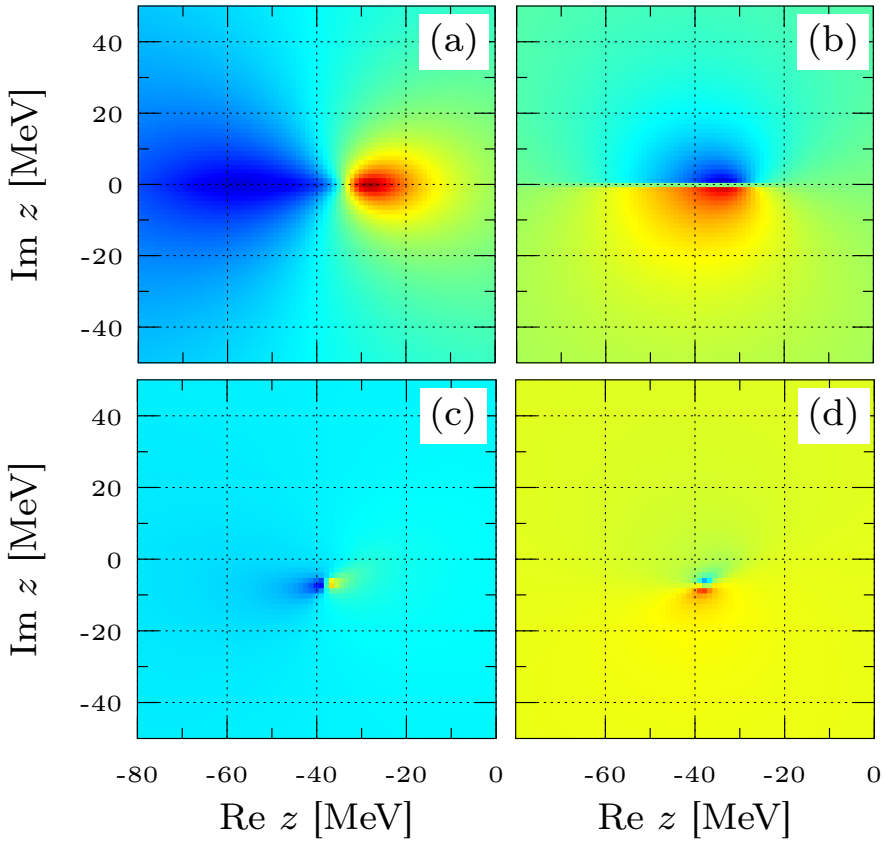

Figure 4.14: Real (a) and imaginary (b) parts of the one-particle Green's function at zero momentum $G(0,z)$, and real (c) and imaginary (d) parts of its analytical continuation at zero momentum $\tilde{G}(0,z)$ in the complex energy plane. The density is $\rho = 0.08$ fm^{-3}.

Thus, the pole in this propagator leads to an equation for the fully dressed quasi-particle spectrum $\varepsilon(k)$ and inverse lifetime $\Gamma(k)$. This spectrum can be compared with the approximations usually employed. To lowest order, known as *first renormalization*, one neglects the imaginary part in Σ. This leads to

$$\begin{aligned} \varepsilon_1(k) &= \frac{k^2}{2m} + \mathrm{Re}\ \Sigma[k, \varepsilon_1(k)] \\ \Gamma_1(k) &= \mathrm{Im}\ \Sigma[k, \varepsilon_1(k)] \; . \end{aligned} \tag{4.17}$$

Fig. 4.15 shows the absolute value of the analytically continued propagator for relative momenta 0, k_F and $2k_F$, in panels (a), (b) and (c), respectively. Also, we include the fully dressed quasi-particle pole (crosses) and the *first renormalization* pole (red circles). A clear difference between the fully dressed quasi-particle pole and the one obtained at the lowest order of the approximation, is evidenced for $k = 0$. For $k \geq k_F$, differences between both poles become negligible. To see this feature more clearly, the momentum dependence of the fully dressed and *first normalization* quasi-particle spectra, together with the inverse lifetimes, are shown in Fig. 4.16 for $\rho = 0.08$ fm $^{-3}$. We observe that the difference between both results diminishes gradually at higher momenta. These findings are consistent with those reported by Rios and Somà in isospin-symmetric nuclear matter [75, 87].

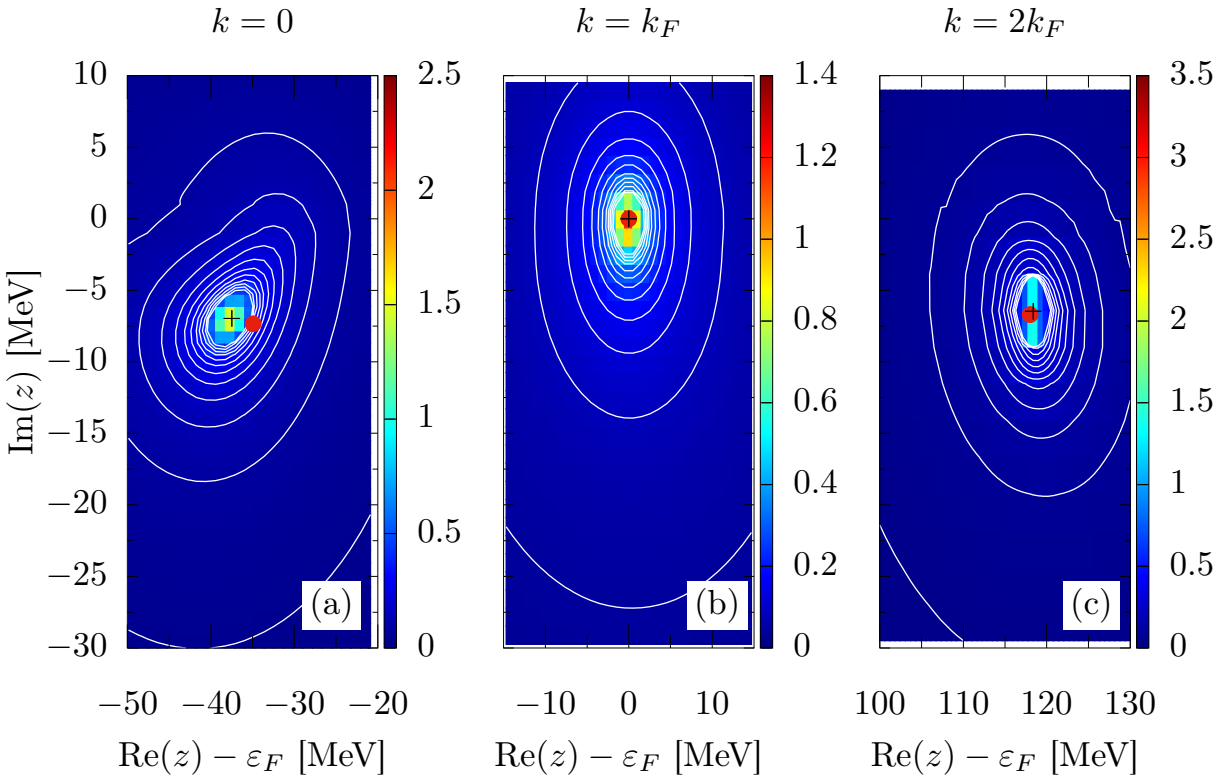

Figure 4.15: Modulus of $\tilde{G}(k, \omega)$ for $k = 0$ (a), k_F (b) and $2k_F$ (c) at $\rho = 0.08$ fm^{-3}. Crosses indicate the fully dressed quasi-particle pole, while red circles denote the *first renormalization* quasi-particle one.

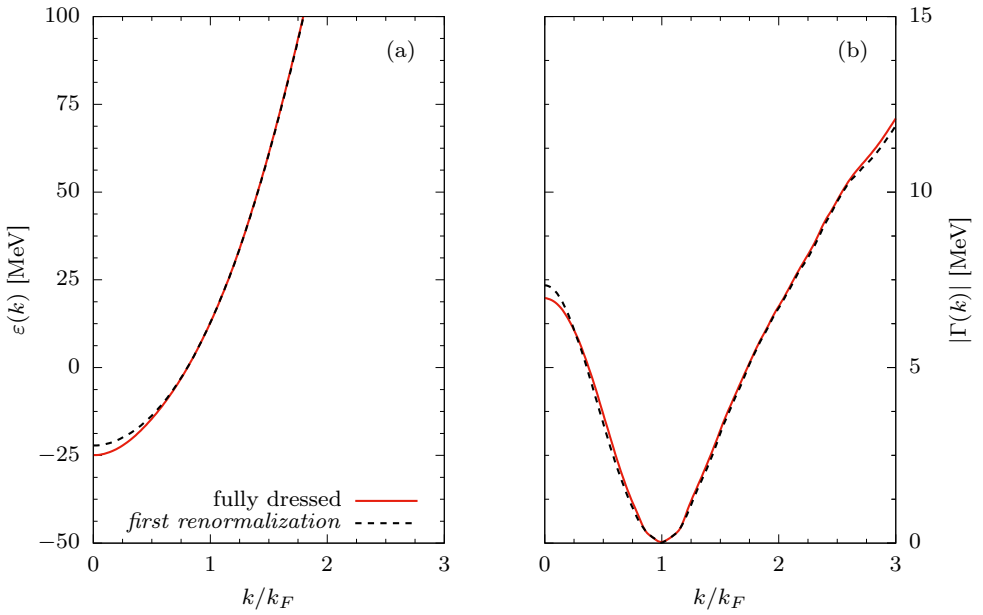

Figure 4.16: Fully dressed (solid red curves) and *first renormalization* (dashed black curves) quasi-particle spectra (a), and inverse lifetimes (b), at $\rho = 0.08$ fm $^{-3}$.

Once the quasi-particle spectrum is determined, we evaluate the group velocity, giving access to the *in-medium* mean-free path [Eq. (4.12)]. Note that the quasi-particle spectrum is a strictly increasing function of momentum, therefore it can be used unambiguously to express the momentum in terms of the quasi-particle energy $k(\varepsilon)$. Thus, we express the mean-free path in terms of the energy as

$$\lambda(\varepsilon) = \frac{[\partial k(\varepsilon)/\partial\varepsilon]^{-1}}{|\Gamma[k(\varepsilon)]|} \,. \tag{4.18}$$

In Fig. 4.17 we show the neutron mean-free path λ relative to the mean internucleon separation $L = \rho^{-1/3}$, as function of the difference between the quasi-particle and Fermi energies $\varepsilon - \varepsilon_F$, for different densities. These values have been obtained using the fully dressed quasi-particle spectrum. However, since the *first renormalization* spectrum only differs from the fully dressed one at low momenta, the only considerable differences take place for hole energies ($\varepsilon < \varepsilon_F$). Additionally, we observe that the mean-free path increases with the energy for $\varepsilon < \varepsilon_F$. For $\varepsilon > \varepsilon_F$, instead, it decreases reaching a plateau. At the Fermi energy, it becomes infinite, due to the infinite lifetimes of quasi-particles at the Fermi surface. The asymptotic values at high energies are approximately λ/L=1.0, 0.4, 0.16 and 0.11, for densities 0.04, 0.08, 0.16 and 0.24 fm^{-3}, respectively.

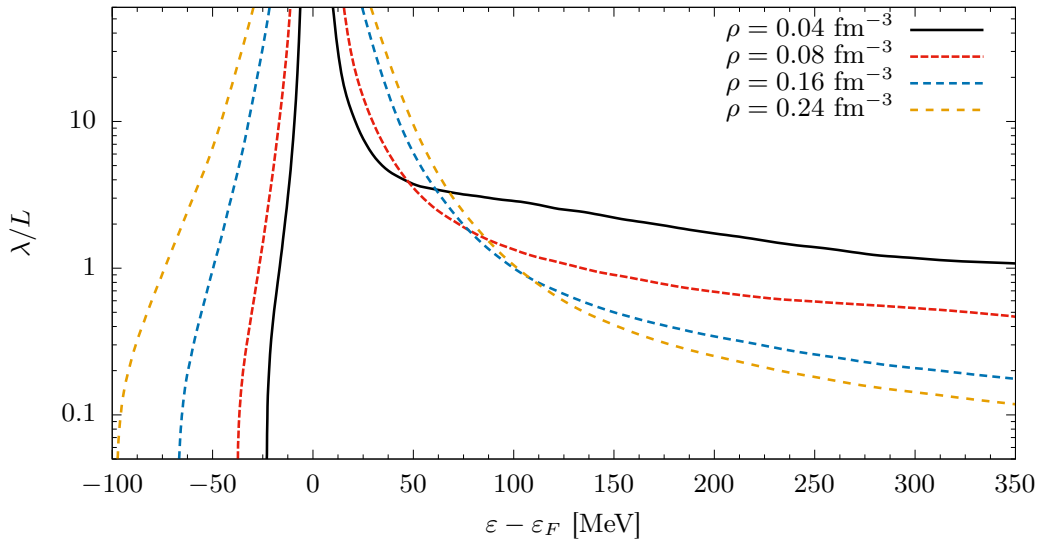

Figure 4.17: *In-medium* neutron mean-free path relative to the mean internucleon separation, as a function of energy at various densities. The results are shown on a logarithmic scale.

An asymmetric dependence of λ/L on the density is observed. For energies below the Fermi energy, the mean-free path increases with increasing the density. Conversely, for energies much greater than ε_F, for example, above $\varepsilon_F + 100$ MeV, an increase in the density yields a decrease of the mean-free path. Additionally, near the Fermi energy the mean-free path increases with increasing density.

4.4 *In-medium* bound states and pairing gap

Stable self-consistent solutions are obtained with the considerations outlined for the iterative scheme, with no singularities in the T matrix for real energies. In fact, the determinant in Eq. (3.24) never vanishes for real energies. This means that there are not di-neutrons in normal neutron matter within SCGF, in contrast with findings reported by Arellano *et al.* within BHF. As we mentioned in Chap. 3, this was expected because h-h (p-p) propagation gives no room for discrete eigenstates below (above) $2\varepsilon_F$.

On the other hand, if the non-interacting two-particle dressed propagator is extended to complex energies as

$$G_2^0(\mathbf{K},\mathbf{k},z) = \int_{\varepsilon_F}^{\infty}\int_{\varepsilon_F}^{\infty} \frac{A_p(\mathbf{k}_+,E)A_p(\mathbf{k}_-,E')}{z-E-E'}dEdE' - \int_{-\infty}^{\varepsilon_F}\int_{-\infty}^{\varepsilon_F} \frac{A_h(\mathbf{k}_+,E)A_h(\mathbf{k}_-,E')}{z-E-E'}dEdE' \,, \tag{4.19}$$

similarly as we did for the one-particle propagator, it results in a unique complex variable function, analytic off the real axis. The real-valued propagator can be recovered from the complex one near the real axis as

$$G_2^0(\omega) = \begin{cases} \lim_{\eta\to 0^+} G_2^0(\omega + i\eta) & ,\omega > 2\varepsilon_F \\ \lim_{\eta\to 0^+} G_2^0(\omega - i\eta) & ,\omega < 2\varepsilon_F \end{cases} \tag{4.20}$$

When we impose $D(K, z_b) = \det[1 - G_2^0(K, z_b)V] = 0$, two complex conjugate eigenvalues $z_b^{\pm}$ are found at a given density. In Fig. 4.18, we plot $D(K, z_b)$ in the complex plane. Here we consider the ${}^1S_0$ channel at $\rho = 0.007$ fm^{-3}. In the left-hand side (LHS) we show a colored level surface for the modulus $|D(0, z)|$. In the right-hand side (RHS) we plot $D(0, z)$ with the domain coloring technique, where the colors and saturation indicate the phase and modulus, respectively. We observe two conjugate zeros of the determinant located at $(z_b^{\pm} - 2\varepsilon_F) = -0.26 \pm 2.44$ MeV.

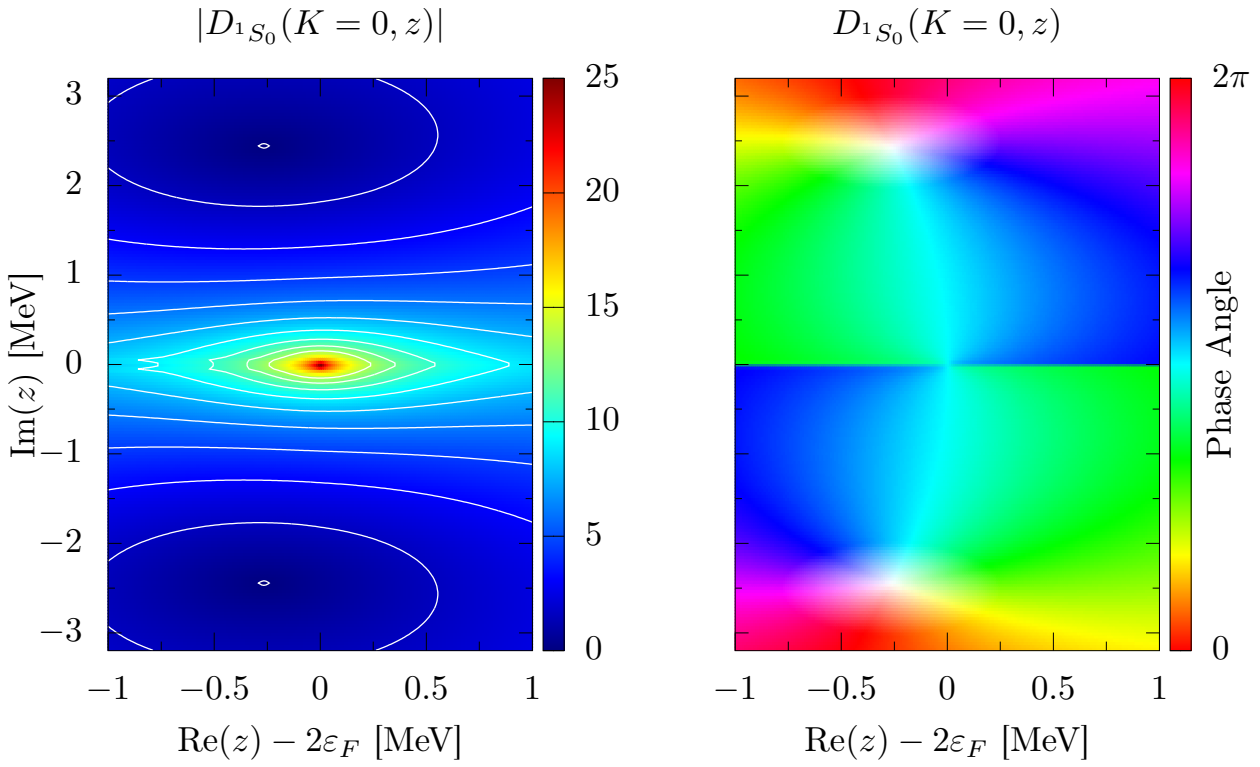

Figure 4.18: $|D_{^1S_0}(0, z)|$ (LHS) and domain coloring of $D_{^1S_0}(0, z)$ (RHS) in the complex plane for a density of 0.007 fm^{-3}. In the LHS panel, the saturation indicates the magnitude of the complex number.

After a more thorough study we found that these complex eigenvalues take place at densities below $0.08\,\mathrm{fm}^{-3}$, namely $k_F \leq 1.33\,\mathrm{fm}^{-1}$. Under their presence, any time dependence yields to an exponentially exploding solution in time and the system becomes unstable, effect known as pairing instability [34]. Despite this feature, some properties of the superfluid state can be explored for these eigenenergies and associated eigenfunctions.

The simplest theory that takes into account the condensation of Cooper pairs in fermionic systems is the Bardeen-Cooper-Schrieffer (BCS) theory. Within this theory, the energy gap $\Delta(k)$ for states with orbital momentum L satisfies

$$\Delta_L(k) = -\frac{2}{\pi}\sum_{L'}\int_0^\infty V_{LL'}(k,p)\frac{\Delta_{L'}(p)}{2E(p)}p^2dp\ , \tag{4.21}$$

where

$$E(k)^2 = (e(k)-\varepsilon_F)^2 + \Delta(k)^2\ . \tag{4.22}$$

Here $e(k)$ is the quasi-particle energy. The normal (n) and anomalous (χ) density are given by

$$n(k) = \frac{1}{2}\left[1 - \frac{e(k)-\varepsilon_F}{E(k)}\right]\ , \tag{4.23a}$$

$$\chi(k) = \frac{\Delta(k)}{2E(k)}\ . \tag{4.23b}$$

The Fermi energy is obtained from the condition $\rho = \nu\int\frac{d\mathbf{k}}{(2\pi)^3}n(k)$, and the system of equations can be solved self consistently. For uncoupled states, Eq. (4.21) can be written as

$$2\sqrt{[e(k)-\varepsilon_F]^2+\Delta(k)^2}\,\chi(k) = -\frac{2}{\pi}\int_0^\infty V(k,p)\chi(p)p^2dp\ . \tag{4.24}$$

Arellano and Isaule [10, 54] noticed that, if $|\Delta(k)| \ll |e(k)-\varepsilon_F|$ this equation is quite similar to the BHF equation for the wave function of two bound neutrons without translational motion. In this case, Eq. (4.24) reads

$$2[e(k)-\varepsilon_F]\chi(k) = -\frac{2}{\pi}\int_0^\infty V(k,p)\chi(p)p^2dp\ , \tag{4.25}$$

for $e(k) > \varepsilon_F$. On the other hand, the equation for a bound state within BHF can be expressed as

$$(h_1+h_2-E_b)\,|\psi_b\rangle = -V\,|\psi_b\rangle\ , \tag{4.26}$$

in other words

$$[2e(k)-E_b]\psi_b(\mathbf{k}) = -\frac{2}{\pi}\int_{k_F}^\infty V(k,p)\psi_b(p)p^2dp\ . \tag{4.27}$$

Comparing Eq. (4.27) for ψ_b with Eq. (4.25) for χ, we notice their resemblance. Note that if we assume $E_b = 2\varepsilon_F \pm i\, W_b$, the resemblance is even closer.

To explore these ideas, we consider the study of Ref. [79] on "*In-medium* bound states and pairing gap". There, the authors consider h-h propagation and quasi-particle spectral functions, so that G_2^0 is given by

$$\left[G_2^0(z)\right]^{-1} = \xi(z - h_1 - h_2)\ , \tag{4.28}$$

where the momentum representation of ξ is given by

$$\xi(k_1, k_2) = \theta(k_1 - k_F)\theta(k_2 - k_F) - \theta(k_F - k_1)\theta(k_F - k_2) \tag{4.29}$$

On the other hand, Eq. (3.22) for the eigenvalue problem, can be written as

$$G_2^0(E_b) V\, |\psi_b\rangle = |\psi_b\rangle\ . \tag{4.30}$$

Therefore

$$-\, G_2^0(E_b)^{-1}\, |\psi_b\rangle = -V\, |\psi_b\rangle\ . \tag{4.31}$$

Combining with Eq. (4.28) for G_2^0 the above equation can be expressed as

$$\xi[2e(k) - 2\varepsilon_F \pm W_b i]\psi_b(k) = -\frac{2}{\pi}\int_0^\infty V(k,p)\psi_b(p)p^2 dp\ , \tag{4.32}$$

restricted to zero total momentum. By taking the absolute value we obtain

$$|\psi_b(k)| = \frac{\left|\frac{2}{\pi}\int_0^\infty V(k,p)\psi_b(p)p^2 dp\right|}{\sqrt{[2e(k) - 2\varepsilon_F]^2 + {W_b}^2}}\ . \tag{4.33}$$

We now observe the close resemblance of this equation to the one for the absolute value of the anomalous density, expressed as

$$|\chi(k)| = \frac{\left|\frac{2}{\pi}\int_0^\infty V(k,p)\chi(p)p^2 dp\right|}{2\sqrt{[e(k) - \varepsilon_F]^2 + \Delta(k)^2}}\ . \tag{4.34}$$

Thus, if we use the constant gap approximation $\Delta(k) \simeq \Delta(k_F)$, the absolute value of the wave function is related to the absolute value of the anomalous density. Moreover, the maximum gap is equal to the imaginary part of the complex eigenvalue $\Delta(k_F) \simeq W_b$ [69, 78, 79].

Particularly, we are considering the sp dispersion over energies. Thus, G_2^0 does not have a simple analytical expression. Moreover, our complex eigenenergies do not have an exact $2\varepsilon_F$ real part. Despite of this, a comparison with the pairing gap can be explored.

In Fig. 4.19 we show the real and imaginary parts of the eigenvalue with positive imaginary part z_b^+, as a function of the Fermi momentum k_F. We also show the pairing gap at k_F obtained within BCS, by solving Eqs. (4.21) to (4.23) self-consistently, where $e(k)$ is the sp spectrum obtained from normal neutron matter within SCGF and BHF schemes. Here, only the $^1S_0$ channel is considered. We do not find solutions for the eigenvalue problem and the BCS equations for k_F above 1.34 fm^{-1}.

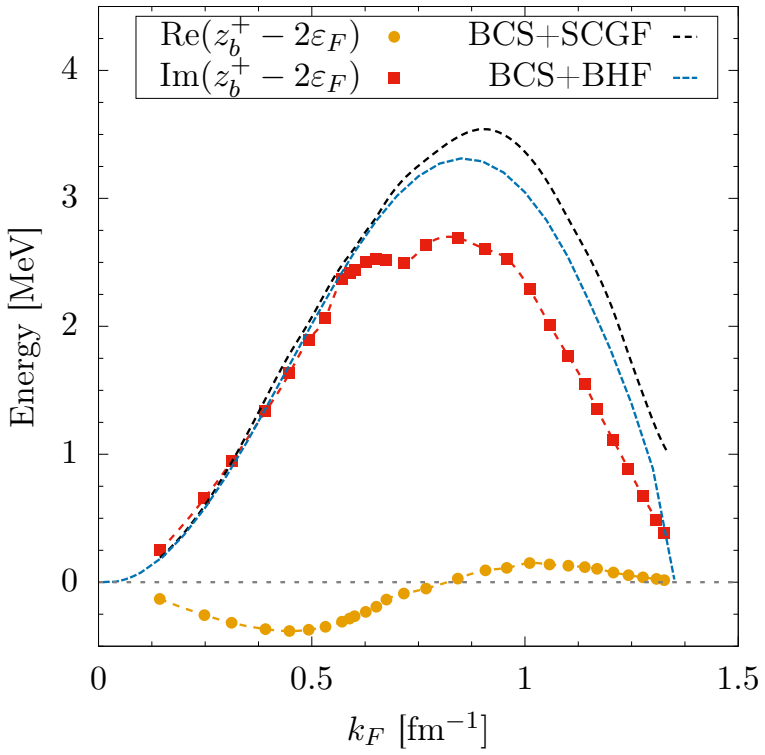

Figure 4.19: Real (orange circles) and imaginary (red squares) parts of the complex eigenvalue with positive imaginary part z_b^+, together with the pairing gap at $k = k_F$ within BCS, obtained with a SCGF (black dashed curve) and BHF (blue dashed curve) sp spectrum. The channel is $^1S_0$.

We observe that the gap estimated with the imaginary part of z_b^+, behaves in a similar way than the gaps obtained within BCS, featuring a maximum around $k_F = 0.9$ fm^{-1}. All of them deviate slightly for k_F below 0.55 fm^{-1}. For greater Fermi momenta, their differences increase, specially around the maximum value, where Im($z_b^+ - 2\varepsilon_F$) is about 0.8 MeV less than the BCS gap obtained with a SCGF spectrum, and around 0.6 MeV less than the BCS gap obtained with a BHF spectrum . These results differ from the ones reported in Ref. [79], where they find an excellent agreement between the imaginary part of the complex eigenenergies and the BCS gap at the Fermi surface, within mean-field and quasi-particle approximations.

On the other hand, when short-range correlations (SRC) are included beyond BCS, such as in Refs. [38, 74], the ${}^1S_0$ overall gap is reduced with a maximum that sits at nearly 2.25 MeV around $k_F = 0.8 - 0.9$ fm^{-1}, for the AV18 potential. In those works, a generalization of the BCS equation is introduced to include SRC. This is accomplished by making

$$E(k)^2 = \xi(k)^2 + \Delta^2(k) \ , \tag{4.35}$$

where in the zero-temperature case, $\xi(k)$ is given by

$$\frac{1}{2\xi(k)} = \int_{-\infty}^{\infty} dE \, dE' \, \frac{[1 - \theta(\varepsilon_F - E) - \theta(\varepsilon_F - E')]}{E + E'} A(k, E) A(k, E') \ . \tag{4.36}$$

Our estimated gap with $\mathrm{Im}(z_b^+ - 2\varepsilon_F)$, is in agreement with those findings, giving a maximum of 2.69 MeV at $k_F = 0.84$ fm^{-1}. Therefore, within SCGF theory, the imaginary part of the *in-medium* bound states energies, cannot be used to obtain the simplest BCS gap approximation, but to estimate the gap beyond BCS with SRC.

In Fig. 4.19, we also observe a shift of the real part of the eigenvalues to the h-h sector of the spectrum (energies below $2\varepsilon_F$) for k_F below 0.8 fm^{-1}, with a minimum of $\mathrm{Re}(z_b^+ - 2\varepsilon_F) = -0.38$ MeV at $k_F = 0.44$ fm^{-1}, and a deviation to the p-p sector of the spectrum (energies above $2\varepsilon_F$) for k_F above 0.8 fm^{-1}, with a maximum of $\mathrm{Re}(z_b^+ - 2\varepsilon_F) = 0.15$ MeV at $k_F = 1.01$ fm^{-1}. This deviation of the real part of the eigenvalues from $2\varepsilon_F$ is related to the strength of the attraction in the NN channel [78].

Chapter 5

Summary and conclusions

We have presented a microscopic study of normal neutron matter at zero-temperature within the SCGF theory in the ladder approximation. The realistic Argonne V18 potential was used as the bare *NN* interaction. Two approximations have been introduced to obtain fully self-consistent stable solutions. The first one is the angle-average in the two-particle propagator in the ladder equation, which allows to decouple partial waves with different total angular momentum. The second one is the decomposition of the spectral functions into a delta function and a soft background contribution, which was introduced to control the sharpness of the functions near the quasi-particle peak and the dispersion of the particles over a wide range of energies. With these approximations, the fully off-shell structure of the self-energy and spectral functions has been obtained on an energy-momentum lattice. The energy, momentum and density dependence of the relevant quantities have been discussed thoroughly. In the following, we summarize some of these main features.

We have found that the real part of the self-energy is mainly dominated by an energy independent or static contribution. In contrast, the imaginary part has an important energy dependence, with density dependent low and high energy tails. These self-energies are then used to evaluate the spectral functions. The width of these functions over energies near the quasi-particle peak is dominated by the density, becoming narrower with decreasing density. This dispersion of particles over energies causes a depletion of low-momentum states, which is mainly explained by short-range correlations, and is reflected on the momentum distribution.

Special attention was paid to the differences between the BHF results, which only accounts for p-p propagation, and the full solution, which includes both h-h and p-p propagation. We have found an overall repulsive effect in SCGF results compared to the BHF ones, consistent with results reported in Refs. [24, 44, 53, 76]. This was observed both on the on-shell values of the self-energy, as well as in the equation of state at high densities. This difference can be attributed to the backward propagation included in the T matrix.

We have also determined the *in-medium* mean-free path in neutron matter with the techniques proposed by Rios and Somà [75, 87], where the pole in the analytic continuation of the one-particle Green's function is considered. The quasi-particle spectra are similar to the ones within the lowest-order approximation, except for low momentum values. Therefore, for high energies, the mean-free paths provided with this method do not vary significantly if we employ the *first renormalization* approximation. These high energy mean-free paths are practically constant as a function of energy, and decrease with increasing density.

The formation of *in-medium* di-neutrons has been addressed within SCGF, where we notice that the inclusion of h-h propagation automatically inhibits the possibility of these bound states in the way described within BHF, that is, as singularities of the *in-medium* effective interaction in the real energy axis. This proves that the findings by Arellano, Delaroche and Isaule [10, 54] on di-nucleons, is a result of the BHF approximation only. Within a full scheme, with a less number of approximations, the spectrum is fully occupied by the continuum states and therefore, there is no room for discrete bound states. Despite this, we have found the appearance of *in-medium* bound states in the complex energy plane for the $^1S_0$ channel, at densities below 0.08 fm^{-3}, signaling a pairing instability. Based on the ideas developed in Ref. [79], we have made contact between these complex eigenenergies and the pairing gap in the superfluid state with the inclusion of short-range correlations.

An important result from this work is the non-existence of di-neutron bound states in low-density neutron matter. This finding is in contrast with results obtained in the BHF approach. As mentioned before, this is due to the full account of h-h propagation within SCGF theory, which embodies as a particular case the BHF approximation. The study presented here has been restricted to the use of AV18 *NN* bare potential and its extension to include other potentials should be carried out, particularly with the use of chiral potentials. This would help to elucidate whether the findings presented here remain robust under the bare interaction considered. Another interesting issue, in the context of the SCGF theory implemented in this work, would be to consider isospin-symmetric nuclear matter. This case is of particular interest for two reasons. One is the presence and role of deuteron bound states, which we know do take place at zero density, but we do not know at what densities they get dissolved. The other reason is about the existence of two sp potentials that fulfill self-consistency within BHF at subsaturation densities. The question here is whether solutions within SCGF theory exhibit similar features. These issues constitute a natural extension of this work.

Bibliography

[1] B. P. Abbott et al. GW170817: Observation of Gravitational Waves from a Binary Neutron Star Inspiral. *Phys. Rev. Lett.*, 119(16):161101, October 2017.

[2] B. P. Abbott et al. Multi-messenger Observations of a Binary Neutron Star Merger. *ApJL*, 848(2):L12, October 2017.

[3] A.A. Abrikosov, L.P. Gorkov, I.E. Dzyaloshinski, and R.A. Silverman. *Methods of Quantum Field Theory in Statistical Physics*. Dover Books on Physics. Dover Publications, 2012.

[4] Nelson Adriazola. Potenciales NN de inversión a energías sobre el umbral de producción de piones. Master's thesis, Universidad de Chile, 2019.

[5] T. Alm, G. Röpke, A. Schnell, N. H. Kwong, and H. S. Köhler. Nucleon spectral function at finite temperature and the onset of superfluidity in nuclear matter. *Phys. Rev. C*, 53:2181–2193, May 1996.

[6] M.R. Anastasio, L.S. Celenza, W.S. Pong, and C.M. Shakin. Relativistic nuclear structure physics. *Phys. Rep.*, 100(6):327–392, 1983.

[7] John Antoniadis et al. A Massive Pulsar in a Compact Relativistic Binary. *Science*, 340:6131, 2013.

[8] H. F. Arellano, F. A. Brieva, and W. G. Love. In-medium full-folding optical model for nucleon-nucleus elastic scattering. *Phys. Rev. C*, 52:301–315, Jul 1995.

[9] H. F. Arellano and J.-P. Delaroche. Toward an actual account for the angular dependence of the Brueckner-Bethe-Goldstone propagator in nuclear matter. *Phys. Rev. C*, 83:044306, Apr 2011.

[10] Hugo Arellano and Jean-Paul Delaroche. Low-density homogeneous symmetric nuclear matter: Disclosing dinucleons in coexisting phases. *European Physical Journal A*, 51, 10 2014.

[11] M. Baldo and C. Maieron. Neutron matter at low density and the unitary limit. *Phys. Rev. C*, 77:015801, Jan 2008.

[12] Marcello Baldo. *Nuclear Methods and the Nuclear Equation of State*. WORLD SCIENTIFIC, November 1999.

[13] A. Bauswein and H.-T. Janka. Measuring Neutron-Star Properties via Gravitational Waves from Neutron-Star Mergers. *Phys. Rev. Lett.*, 108:011101, Jan 2012.

[14] Djelloul Benzaid, Salaheddine Bentridi, Abdelkader Kerraci, and Naima Amrani. Bethe–Weizsäcker semiempirical mass formula coefficients 2019 update based on AME2016. *Nucl. Sci. Tech.*, 31(1):9, 2020.

[15] G. Bertsch and Derek Bingham. Estimating Parameter Uncertainty in Binding-Energy Models by the Frequency-Domain Bootstrap. *Phys. Rev. Lett.*, 119, 03 2017.

[16] H. A. Bethe, B. H. Brandow, and A. G. Petschek. Reference Spectrum Method for Nuclear Matter. *Phys. Rev.*, 129:225–264, Jan 1963.

[17] Raymond F. Bishop and Hermann G. Kümmel. The Coupled Cluster Method. *Physics Today*, 40(3):52–60, March 1987.

[18] P. Bożek. One-body properties of nuclear matter with off-shell propagation. *Phys. Rev. C*, 65:054306, Apr 2002.

[19] Piotr Bozek and P. Czerski. In medium T matrix with realistic nuclear interactions. *Acta Phys. Pol. B*, 34, 01 2003.

[20] P. Bożek. Superfluid nuclear matter calculations. *Nucl. Phys. A*, 657(2):187–215, 1999.

[21] R. Brockmann and R. Machleidt. Relativistic nuclear structure. I. Nuclear matter. *Phys. Rev. C*, 42:1965–1980, Nov 1990.

[22] K. A. Brueckner and J. L. Gammel. Properties of Nuclear Matter. *Phys. Rev.*, 109:1023–1039, Feb 1958.

[23] K. A. Brueckner, C. A. Levinson, and H. M. Mahmoud. Two-Body Forces and Nuclear Saturation. I. Central Forces. *Phys. Rev.*, 95:217–228, Jul 1954.

[24] Arianna Carbone. *Self-consistent Green's Functions with three-body forces*. PhD thesis, 2014.

[25] J. Carlson, J. Morales, V. R. Pandharipande, and D. G. Ravenhall. Quantum Monte Carlo calculations of neutron matter. *Phys. Rev. C*, 68:025802, Aug 2003.

[26] Claudio Ciofi degli Atti, S. Simula, L. L. Frankfurt, and M. I. Strikman. Two nucleon correlations and the structure of the nucleon spectral function at high values of momentum and removal energy. *Phys. Rev. C*, 44:R7–R11, 1991.

[27] John W. Clark. Variational theory of nuclear matter. *Progress in Particle and Nuclear Physics*, 2:89–199, 1979.

[28] H. Cromartie, Esfrit Fonseca, S. Ransom, P. Demorest, Z. Arzoumanian, H. Blumer, P. Brook, M. DeCesar, Timothy Dolch, J. Ellis, R. Ferdman, Elisabetta Ferrara, N. Garver-Daniels, P. Gentile, M. Jones, M. Lam, D. Lorimer, R. Lynch, M. McLaughlin, and Weiwei Zhu. Relativistic Shapiro delay measurements of an extremely massive millisecond pulsar. *Nature Astronomy*, 4:1–5, 01 2020.

[29] F. de Jong and H. Lenske. Towards a fully self-consistent spectral function of the nucleon in nuclear matter. *Phys. Rev. C*, 56:154–164, Jul 1997.

[30] P Demorest, T Pennucci, S Ransom, M Roberts, and J Hessels. A two-solar-mass neutron star measured using Shapiro delay. *Nature*, 467:1081–3, 10 2010.

[31] Y. Dewulf, W. H. Dickhoff, D. Van Neck, E. R. Stoddard, and M. Waroquier. Saturation of nuclear matter and short-range correlations. *Phys. Rev. Lett.*, 90:152501, Apr 2003.

[32] Y. Dewulf, D. Van Neck, and M. Waroquier. Short-range correlations in nuclear matter using Green's functions within a discrete pole approximation. *Phys. Lett. B*, 510(1):89–97, 2001.

[33] Y. Dewulf, D. Van Neck, and M. Waroquier. Effects of self-consistency in a Green's function description of saturation in nuclear matter. *Phys. Rev. C*, 65:054316, May 2002.

[34] W. Dickhoff and Dimitri Van Neck. *Many-body theory exposed! Propagator description of quantum mechanics in many-body systems, 2nd edition.* 01 2008.

[35] W. H. Dickhoff, C. C. Gearhart, E. P. Roth, A. Polls, and A. Ramos. Phase shifts and in-medium cross sections for dressed nucleons in nuclear matter. *Phys. Rev. C*, 60:064319, Nov 1999.

[36] W.H. Dickhoff. Connection between Brueckner ladders and pairing correlations. *Phys. Lett. B*, 210(1):15–19, 1988.

[37] W.H. Dickhoff and C. Barbieri. Self-consistent Green's function method for nuclei and nuclear matter. *Progress in Particle and Nuclear Physics*, 52(2):377–496, 2004.

[38] D. Ding, A. Rios, H. Dussan, W. H. Dickhoff, S. J. Witte, A. Carbone, and A. Polls. Pairing in high-density neutron matter including short- and long-range correlations. *Phys. Rev. C*, 94:025802, Aug 2016.

[39] E.N. Economou. *Green's Functions in Quantum Physics*. Springer Series in Solid-State Sciences. Springer Berlin Heidelberg, 2006.

[40] D. R. Entem, N. Kaiser, R. Machleidt, and Y. Nosyk. Peripheral nucleon-nucleon scattering at fifth order of chiral perturbation theory. *Phys. Rev. C*, 91:014002, Jan 2015.

[41] D. R. Entem and R. Machleidt. Accurate charge-dependent nucleon-nucleon potential at fourth order of chiral perturbation theory. *Phys. Rev. C*, 68:041001, Oct 2003.

[42] D. R. Entem, R. Machleidt, and Y. Nosyk. High-quality two-nucleon potentials up to fifth order of the chiral expansion. *Phys. Rev. C*, 96:024004, Aug 2017.

[43] A. L. Fetter and J. D. Walecka. *Quantum Theory of Many-Particle Systems*. McGraw-Hill, Boston, 1971.

[44] T. Frick. *Self-Consistent Green's Functions in Nuclear Matter at Finite Temperature*. PhD thesis, 2004.

[45] T. Frick and H. Müther. Self-consistent solution to the nuclear many-body problem at finite temperature. *Phys. Rev. C*, 68:034310, Sep 2003.

[46] T. Frick, H. Müther, and A. Polls. Sum rules and short-range correlations in nuclear matter at finite temperature. *Phys. Rev. C*, 69:054305, May 2004.

[47] V. M. Galitskii and A. B. Migdal. Application of quantum field theory methods to the many body problem. *Sov. Phys. JETP*, 7(1):96–104, 1958.

[48] Stefano Gandolfi, Alexandros Gezerlis, and J. Carlson. Neutron Matter from Low to High Density. *Annu. Rev. Nucl. Part.*, 65(1):303–328, 2015.

[49] Alexandros Gezerlis and J. Carlson. Strongly paired fermions: Cold atoms and neutron matter. *Phys. Rev. C*, 77:032801, Mar 2008.

[50] S. Goudarzi and H. R. Moshfegh. Neutron and nuclear matter properties with chiral three-nucleon forces. *Nucl. Phys. A*, 985:1–19, 2019.

[51] Morten Hjorth-Jensen, Maria Paola Lombardo, and Ubirajara van Kolck, editors. *An Advanced Course in Computational Nuclear Physics*, volume 936. Springer, 2017.

[52] Charles Horowitz. Neutron rich dense matter, neutron star mergers, and laboratory experiments. In *APS April Meeting Abstracts*, volume 2019 of *APS Meeting Abstracts*, page R05.001, January 2019.

[53] Arnau Rios Huguet. *Thermodynamical properties of nuclear matter from a self-consistent Green's function approach*. PhD thesis, 2007.

[54] Felipe Isaule, H. F. Arellano, and Arnau Rios. Di-neutrons in neutron matter within a Brueckner-Hartree-Fock approach. *Phys. Rev. C*, 94(3), sep 2016.

[55] Mikkel B. Johnson. Theory of meson exchange potentials for nuclear physics. *Annals of Physics*, 97(2):400–451, 1976.

[56] L.P. Kadanoff and G. Baym. *Quantum Statistical Mechanics*. W.A. Benjamin Inc., New York, 1962.

[57] Daniel S. Koltun. Theory of mean removal energies for single particles in nuclei. *Phys. Rev. C*, 9:484–497, Feb 1974.

[58] M. Lacombe, B. Loiseau, J. M. Richard, R. Vinh Mau, J. Côté, P. Pirès, and R. de Tourreil. Parametrization of the Paris $N-N$ potential. *Phys. Rev. C*, 21:861–873, Mar 1980.

[59] K. Langanke, Joachim A. Maruhn, and S. E. Koonin, editors. *Computational Nuclear Physics 1*. Springer Berlin Heidelberg, 1991.

[60] Martin Letz and Frank Marsiglio. Self-Consistent Treatment of Dynamical Correlation Functions Using a Spectral Representation Technique. *Journal of Low Temperature Physics*, 117:149–173, 1999.

[61] Z. H. Li, U. Lombardo, H.-J. Schulze, W. Zuo, L. W. Chen, and H. R. Ma. Nuclear matter saturation point and symmetry energy with modern nucleon-nucleon potentials. *Phys. Rev. C*, 74:047304, Oct 2006.

[62] Jia-Jing Lu, Zeng-Hua Li, Chong-Yang Chen, M. Baldo, and H.-J. Schulze. Convergence of the hole-line expansion with modern nucleon-nucleon potentials. *Phys. Rev. C*, 96:044309, Oct 2017.

[63] G. M. Murphy and Helen Johnston. The Nuclear Spin of Deuterium. *Phys. Rev.*, 46:95–98, Jul 1934.

[64] J. W. Negele and Erich Vogt, editors. *Advances in Nuclear Physics*. Springer US, 2000.

[65] Feryal Özel, Gordon Baym, and Tolga Güver. Astrophysical measurement of the equation of state of neutron star matter. *Phys. Rev. D*, 82:101301, Nov 2010.

[66] P. Bozek and P. Czerski. Thermodynamic consistency for nuclear matter calculations. *Eur. Phys. J. A*, 11(3):271–275, 2001.

[67] A. Polls, A. Ramos, C.C. Gearhart, W.H. Dickhoff, and H. Müther. Short range correlations and spectral functions for nuclear matter and finite nuclei. *Prog. Part. Nucl. Phys.*, 34:371–380, 1995. Electromagnetic Probes and the Structure Hadrons and Nuclei.

[68] Robert D Puff. Groud-state properties of nuclear matter. *Ann. Phys.*, 13(3):317–358, 1961.

[69] S. Ramanan, S.K. Bogner, and R.J. Furnstahl. Weinberg eigenvalues and pairing with low-momentum potentials. *Nuclear Physics A*, 797(3-4):81–93, dec 2007.

[70] A. Ramos, W. H. Dickhoff, and A. Polls. Binding energy and momentum distribution of nuclear matter using Green's function methods. *Phys. Rev. C*, 43:2239–2253, May 1991.

[71] A. Ramos, W.H. Dickhoff, and A. Polls. Hole-hole propagation and saturation. *Phys. Lett. B*, 219(1):15–21, 1989.

[72] A. Ramos, A. Polls, and W.H. Dickhoff. Single-particle properties and short-range correlations in nuclear matter. *Nucl. Phys. A*, 503(1):1–52, 1989.

[73] A. Rios. Green's Function Techniques for Infinite Nuclear Systems. *Front. in Phys.*, 8:387, 2020.

[74] A. Rios, D. Ding, H. Dussan, W. H. Dickhoff, S. J. Witte, and A. Polls. Beyond BCS pairing in high-density neutron matter. *J. Phys. Conf. Ser.*, 940(1):012014, jan 2018.

[75] Arnau Rios and Vittorio Somà. Self-Consistent Green's Function Calculation of the Nucleon Mean Free Path. *Phys. Rev. Lett.*, 108:012501, Jan 2012.

[76] Arnau Rios Huguet, Artur Polls, and I. Vidaña. Hot neutron matter from a Self-Consistent Green's Functions approach. *Physical Review C*, 79, 10 2008.

[77] E. P. Roth. *Self-consistent Green's function in Nuclear Matter*. PhD thesis, Washington University, St. Louis, 2000.

[78] O. A. Rubtsova, V. I. Kukulin, and V. N. Pomerantsev. In-medium T matrix in case of pairing instability. *Phys. Rev. C*, 103:014307, Jan 2021.

[79] O. A. Rubtsova, V. I. Kukulin, V. N. Pomerantsev, and H. Müther. In-medium bound states and pairing gap. *Phys. Rev. C*, 96:034327, Sep 2017.

[80] J. J. Sakurai and Jim Napolitano. *Modern Quantum Mechanics*. Cambridge University Press, 2 edition, 2017.

[81] R. Sartor. Solution of the bethe-goldstone equation with an exact propagator. *Phys. Rev. C*, 54:809–814, Aug 1996.

[82] A. Schnell, T. Alm, and G. Röpke. Nucleon self-energies and spectral functions in nuclear matter at finite temperature with a realistic potential. *Phys. Lett. B*, 387(3):443–448, 1996.

[83] Stuart L. Shapiro and Saul A. Teukolsky. *Black holes, white dwarfs and neutron stars. The physics of compact objects*. 1983.

[84] V. Somà and P. Bożek. In-medium T matrix for nuclear matter with three-body forces: Binding energy and single-particle properties. *Phys. Rev. C*, 78:054003, Nov 2008.

[85] V. Somà and P. Bożek. Thermodynamic properties of nuclear matter with three-body forces. *Phys. Rev. C*, 80:025803, Aug 2009.

[86] V. Soma and P. Bozek. In medium T-matrix for nuclear matter with three-body forces: Binding energy and single particle properties. *Phys. Rev. C*, 78:054003, 2008.

[87] V. Soma and A. Rios. Nucleon ean-free path in the medium. *EPJ Web Conf.*, 66:03081, 2014.

[88] Vittorio Somà. Self-Consistent Green's Function Theory for Atomic Nuclei. *Front. Phys.*, 8, 2020.

[89] H. Q. Song, M. Baldo, G. Giansiracusa, and U. Lombardo. Bethe-Brueckner-Goldstone Expansion in Nuclear Matter. *Phys. Rev. Lett.*, 81:1584–1587, Aug 1998.

[90] A. W. Steiner and S. Gandolfi. Connecting neutron star observations to three-body forces in neutron matter and to the nuclear symmetry energy. *Phys. Rev. Lett.*, 108:081102, Feb 2012.

[91] Andrew W. Steiner, James M. Lattimer, and Edward F. Brown. The neutron star mass–radius relation and the equation of state of dense matter. *ApJL*, 765(1):L5, feb 2013.

[92] V. G. J. Stoks, R. A. M. Klomp, C. P. F. Terheggen, and J. J. de Swart. Construction of high-quality NN potential models. *Phys. Rev. C*, 49:2950–2962, Jun 1994.

[93] K. Suzuki, R. Okamoto, M. Kohno, and S. Nagata. Exact treatment of the Pauli exclusion operator in nuclear matter calculation. *Nucl. Phys. A*, 665(1):92–104, 2000.

[94] Robert van Leeuwen and Gianluca Stefanucci. Equilibrium and nonequilibrium many-body perturbation theory: A unified framework based on the Martin-Schwinger hierarchy. *Journal of Physics Conference Series*, 427:2001–, 03 2013.

[95] B. E. Vonderfecht, W. H. Dickhoff, A. Polls, and A. Ramos. Distribution of single-particle strength due to short-range and tensor correlations. *Phys. Rev. C*, 44:R1265–R1268, Oct 1991.

[96] B. E. Vonderfecht, C. C. Gearhart, W. H. Dickhoff, A. Polls, and A. Ramos. Bound pair states in nuclear matter. *Phys. Lett. B*, 253:1–8, 1991.

[97] Steven Weinberg. Nuclear forces from chiral Lagrangians. *Phys. Lett. B*, 251:288–292, 1990.

[98] Steven Weinberg. Effective chiral Lagrangians for nucleon - pion interactions and nuclear forces. *Nucl. Phys. B*, 363:3–18, 1991.

[99] Steven Weinberg. Three-body interactions among nucleons and pions. *Phys. Lett. B*, 295(1):114–121, 1992.

[100] R. B. Wiringa, V. G. J. Stoks, and R. Schiavilla. Accurate nucleon-nucleon potential with charge-independence breaking. *Phys. Rev. C*, 51:38–51, Jan 1995.

ANNEX

Approximation for the spectral function

In this annex, some useful explicit expressions will be presented, following the decomposition for the spectral function as

$$A(\mathbf{k},\omega) = Z(\mathbf{k})\delta(\omega - e(\mathbf{k})) + B(\mathbf{k},\omega)\ . \tag{1}$$

If $Z(\mathbf{k})$ is adjusted so that the sum rule is satisfied, then the momentum distribution $n(\mathbf{k})$ becomes expressed as

$$n(\mathbf{k}) = \theta[\varepsilon_F - e(\mathbf{k})]\left\{1 - \int_{\varepsilon_F}^{\infty} B(\mathbf{k},E)dE\right\} + \theta[e(\mathbf{k}) - \varepsilon_F]\int_{-\infty}^{\varepsilon_F} B(\mathbf{k},E)dE\ . \tag{2}$$

For the energy of the system we get

$$\frac{E_{\mathrm{SCGF}}}{N} = \frac{\nu}{\rho}\left\{\int \frac{d\mathbf{p}}{(2\pi)^3}\frac{1}{2}\left[\frac{p^2}{2m}n(\mathbf{k}) + \theta[\varepsilon_F - e(\mathbf{p})]Z(\mathbf{p})e(\mathbf{p}) + \int_{-\infty}^{\varepsilon_F} d\omega\ \omega B(\mathbf{p},\omega)\right]\right\}\ . \tag{3}$$

For Im G_2^0 we have

$$
\begin{aligned}
-\frac{1}{\pi}\text{Im } G_2^0(\mathbf{K},\mathbf{k},\omega) =& [\theta(e_+ - \varepsilon_F)\theta(e_- - \varepsilon_F) + \theta(\varepsilon_F - e_+)\theta(\varepsilon_F - e_-)] \\
& \cdot Z(\mathbf{k}_+)Z(\mathbf{k}_-)\delta(\omega - e_+ - e_-) \\
& + [\theta(e_+ - \varepsilon_F)\theta(\omega - \varepsilon_F - e_+) + \theta(\varepsilon_F - e_+)\theta(e_+ + \varepsilon_F - \omega)] \\
& \cdot Z(\mathbf{k}_+)B(\mathbf{k}_-, \omega - e_+) \\
& + [\theta(e_- - \varepsilon_F)\theta(\omega - \varepsilon_F - e_-) + \theta(\varepsilon_F - e_-)\theta(e_- + \varepsilon_F - \omega)] \\
& \cdot Z(\mathbf{k}_-)B(\mathbf{k}_+, \omega - e_-) \\
& + \theta(\omega - 2\varepsilon_F)\int_{\varepsilon_F}^{\omega-\varepsilon_F} B(\mathbf{k}_+, E)B(\mathbf{k}_-, \omega - E)dE \\
& + \theta(2\varepsilon_F - \omega)\int_{\omega-\varepsilon_F}^{\varepsilon_F} B(\mathbf{k}_+, E)B(\mathbf{k}_-, \omega - E)dE \ ,
\end{aligned}
\tag{4}
$$

and for Im $\Sigma(\mathbf{k},\omega)$ we obtain

$$
\begin{aligned}
\text{Im } \Sigma(\mathbf{k},\omega) =& \theta(\omega - \varepsilon_F)\left\{\int_{2\varepsilon_F-\omega<e(\mathbf{k}')<\varepsilon_F} \frac{d\mathbf{k}'}{(2\pi)^3}\left\langle\frac{\mathbf{k}-\mathbf{k}'}{2}\right|\text{Im}T_{\mathbf{k}+\mathbf{k}'}[\omega + e(\mathbf{k}')]\left|\frac{\mathbf{k}-\mathbf{k}'}{2}\right\rangle_A Z(\mathbf{k}')\right. \\
& \left. + \int_{2\varepsilon_F-\omega}^{\varepsilon_F} dE'' \int \frac{d\mathbf{k}'}{(2\pi)^3}\left\langle\frac{\mathbf{k}-\mathbf{k}'}{2}\right|\text{Im}T_{\mathbf{k}+\mathbf{k}'}(\omega + E'')\left|\frac{\mathbf{k}-\mathbf{k}'}{2}\right\rangle_A B(\mathbf{k}', E'')\right\} \\
& - \theta(\varepsilon_F - \omega)\left\{\int_{\varepsilon_F<e(\mathbf{k}')<2\varepsilon_F-\omega} \frac{d\mathbf{k}'}{(2\pi)^3}\left\langle\frac{\mathbf{k}-\mathbf{k}'}{2}\right|\text{Im}T_{\mathbf{k}+\mathbf{k}'}[\omega + e(\mathbf{k}')]\left|\frac{\mathbf{k}-\mathbf{k}'}{2}\right\rangle_A Z(\mathbf{k}')\right. \\
& \left. + \int_{\varepsilon_F}^{2\varepsilon_F-\omega} dE'' \int \frac{d\mathbf{k}'}{(2\pi)^3}\left\langle\frac{\mathbf{k}-\mathbf{k}'}{2}\right|\text{Im}T_{\mathbf{k}+\mathbf{k}'}(\omega + E'')\left|\frac{\mathbf{k}-\mathbf{k}'}{2}\right\rangle_A B(\mathbf{k}', E'')\right\} \ .
\end{aligned}
\tag{5}
$$

These expressions have been implemented in the subroutines used in this work.